Computational fluid dynamics modeling of cell culture bioreactors

A Dissertation Presented for the
Doctor of Philosophy
Degree
The University of Tennessee, Knoxville

Fernando José Cantarero Rivera
December 2024

DEDICATION

Dedicated to my family (Manuel, Miriam, and Carlos) and my friends for their endless support.

ACKNOWLEDGEMENTS

I would like to first thank Dr. Chen for taking a chance on me and offering me the Ph.D. position. I appreciate his guidance and patience during my program. I would also like to offer my sincere appreciation to my committee members, Dr. Doris D’Souza, Dr. Madhu Dhar, Dr. Scott Lenaghan, Dr. Simon Kahan, for training me in cell culture, computational models and for their guidance, advice, and encouragement. I am also grateful to all my lab mates, friends, and staff in the department and UTK for always being supportive.

I would also like to express my appreciation to: the Cultivated Meat Modeling Consortium for allowing me to work with such an incredible interdisciplinary and multicultural team that awoke a genuine interest in cellular agriculture in me; Dr. Haochen Li, who provided much needed guidance on machine learning topics; all the people in the Dhar and D’Souza labs who contributed with my training in cell culture or helped with the experiments

And finally, I would like to acknowledge the people that mean most in my life for always supporting me and encouraging me to pursue more.

ABSTRACT

Cultivated meat production, driven by increasing meat consumption worldwide, requires optimized bioreactor designs for high cell densities and yields. Computational Fluid Dynamics (CFD) models are invaluable for analyzing bioreactor performance, such as shear stress, turbulence, and oxygen transfer rates. Traditional and recent modeling approaches were reviewed and compared for seven types of cell culture bioreactors. This comparison allowed the identification of some limitations in the CFD models; namely, the considerable computational resources required and lack of accuracy due to assumptions taken to reduce computational time. This body of work reviews CFD models for various bioreactors, explores machine learning (ML) approaches to enhance CFD modeling, and investigates the impact of dynamic viscosity on mixing performance.

An Artificial Neural Network (ANN)-based ML model was developed to predict and correct coarse-mesh-induced errors in CFD modeling of a spinner flask bioreactor. The ANN model improved the Root Mean Square Error (RMSE) values of nodal velocities by an average of 20% at different rotational speeds. The effect of ANN structure, input data normalization, and training dataset combinations on prediction performance was evaluated. However, the model had limited generalization capabilities especially when correcting lower mixing speeds when a higher speed was used during training.

A three-dimensional Convolutional Neural Network (CNN) ML model was then developed to address ANN model’s generalization limitation by predicting high-resolution fluid profiles from a low-resolution counterpart directly. This model’s structure was optimized and was able to improve the coarse shear stress profile by 67%. The model's generalization capabilities were evaluated across bioreactors with different impeller geometries, showing proper generalization for Kolmogorov length but not shear stress when trained with a single dataset but when including data from all impellers in training, the model was able to improve the coarse shear stress profile by an average of 57% regardless of impeller shape.

Finally, the dynamic viscosity of Human Embryo Kidney (HEK) 293T cell cultures was characterized, revealing shear thinning behaviors and an increase with microcarrier concentrations and cell culture stages. Incorporating dynamic viscosity data into the CFD model showed significant influence on shear stress and Kolmogorov length profiles. The results highlight the importance of monitoring dynamic viscosity and controlling mixing parameters for optimized cell growth, especially during scale-up production operations. These methods reduce computational expenses and increase accuracy of CFD models and lay the groundwork for the development of digital twins of tissue engineering bioreactors and advancing the commercialization of cultivated meat.

TABLE OF CONTENTS

LIST OF TABLES

LIST OF FIGURES

1. CHAPTER I. LITERATURE REVIEW

COMPUTATIONAL FLUID DYNAMICS MODELING OF CELL CULTURES IN BIOREACTORS AND ITS POTENTIAL FOR CULTIVATED MEAT PRODUCTION—A MINI-REVIEW

A version of this chapter was originally published by Fernando José Cantarero Rivera and Jiajia Chen:

Cantarero Rivera, F. J. & Chen, J. Computational fluid dynamics modeling of cell cultures in bioreactors and its potential for cultivated meat production—A mini-review. Future Foods 6, 100195 (2022).

As the first author of this literature review article, I was the main contributor to Conceptualization, Literature review, Visualization, and Writing of the manuscript. Dr. Jiajia Chen, as the major professor and corresponding author, contributed to the Conceptualization, Investigation, Supervision, and Writing - Reviewing and Editing of the manuscript

Abstract

Cultivated meat production was developed as a response to the rapidly increasing demand for meat consumption. Bioreactor designs were adapted from other bioprocesses to account for the high cell densities and final yield necessary to commercialize cultivated meat. Computational fluid dynamics (CFD) models are useful tools to analyze the bioreactor performance (e.g., predicting shear stress, turbulence, and oxygen transfer rate) for better bioreactors design so that cell growth can be optimized. This review assesses the CFD models for seven types of bioreactors – stirred tank, wave/rocking, hollow-fiber, fluidized bed, airlift, rotary wall, and high-aspect ratio vessel –and compares strengths and weaknesses of the approaches taken. Traditional approaches include single-phase flow, k-ε turbulence models, and simplified water-like material properties to simulate bioreactor performance. Recent research has focused on using Large Eddy Simulations (LES) and multiphase flow to develop more accurate and robust models. Strategies that can improve CFD model development include incorporating dynamic rheological properties, simulating multiple phases to account for cells and microcarriers, compartmentalizing to speed up simulations, and integrating with micro-scale cell growth models.

Keywords: Cultivated meat, Bioreactors, Computational fluid dynamics, Mammalian cell culture, Microcarriers.

1 Introduction

Cultivated meat, also called clean, lab-grown, cell-based, or *in vitro* meat, is a technology that grows stem cells extracted harmlessly from an animal under a controlled environment, such as a bioreactor, with all the required nutrients. Eventually, these cells will differentiate into tissue similar to the meat that would have been otherwise harvested directly from the animal after slaughter (Mattick, 2018). The first cell-based hamburger patty was made by Mark J. Post from Mosa Meat in 2013, but it cost around €250,000 to make and lacked a fair amount of characteristics that animal-origin meat has (Post, 2014). Nevertheless, the ever-increasing demand for global meat consumption must be addressed and cultivated meat might be a way to fulfill such demands. By 2030, global meat consumption is expected to increase by 14% (OECD et al., 2021). This increase in consumption will translate into negative environmental impacts such as greenhouse gas (GHG) emissions, land use, and animal welfare, among others.

Cultivated meat technology will be a good complement to current animal farms to meet the demands for more meat products without negative environmental impacts (Mattick et al., 2015). An initial life cycle assessment (LCA) study reported that cultivated meat production would use less energy, generate less GHG, and spend less water than conventionally produced meat (Tuomisto and Teixeira de Mattos, 2011). However, more recent studies warn that all LCA presented so far are very speculative and based on lab-scale equipment since a full-scale industrial cultivated meat processing plant is not in place (Lynch and Pierrehumbert, 2019; Mattick et al., 2015; Smetana et al., 2015).

Bioreactor design is crucial for scaling up cultivated meat production and commercialization of the technology (Post et al., 2020). The design must accommodate the needs of the cell types being grown as too much shear stress can induce differentiation while a gentler environment is desirable for cells to proliferate successfully (Allan et al., 2019). Temperature, pH, dissolved oxygen, and cell metabolite concentration are other factors that must be considered as well (Catapano et al., 2009). A design that considers all these aspects could improve the final yield from the process. Thus, it is necessary to develop bioreactors with optimized processing conditions for high cell growth yield.

Computational fluid dynamics (CFD) models have been developed as useful tools to simulate bioreactor environments and determine optimal processing parameters for cell growth. Most of the literature reviewed concerns using CFD in cell culturing for biomedical applications as there are very few published articles regarding cultivated meat modeling (Li et al. 2020; Zhang et al. 2021). These models often simulated lab-scale bioreactors for cell culturing with low cell densities. Much can be learned from bioreactor models for other applications. However, to meet the enormous demand for meat consumption, it is necessary to scale up the production of cultivated meat and grow the cells at a much larger scale and cell density. Some hydrodynamic variables, such as mixing speed of the impellers in a stirred-tank bioreactor, tend to be scale-specific, and although they can be determined experimentally, CFD can help in reducing the cost, time, and risk of contamination inherent to the experiments required (Karimi Alavijeh et al., 2022). The fluid dynamics also vary significantly among bioreactor types. Some studies have used CFD tools to develop cultivated meat technology, but most models are for lab-scale bioreactors with low-density cell cultures. There are some large-scale bioreactor models used for other applications that can provide key insights for cultivated meat processes (Spann et al. 2019). This review focuses on discussing the modeling approaches taken to develop CFD models in simulating different bioreactor environments in cell culture for various applications, identifying current model limitations, and discussing future research directions that can promote the use of CFD tools for cultivated meat production.

2 CFD Modeling of Cell Cultures in Bioreactors

CFD is an essential tool to characterize the hydrodynamics inside bioreactors and can provide a good idea of the environment that cells will be exposed to during culture. CFD has been used to improve the design of scaffolds, stirred tanks, and agitation parameters for microcarriers (Zhang et al., 2020). Microcarriers are beads of different materials that provide cells with a surface for attachment. Readers can refer to (Bodiou et al., 2020) for more details on the use of microcarriers for cultured meat production. Initial implementations of CFD for bioprocessing have focused on single-phase fluid flow, meaning the cell culture is considered a homogeneous fluid, and hydrodynamic shear characterization. Models have evolved into exploring multiphase scenarios that separate cells from the media, and some consider the microcarriers and the bubbles generated by sparging gases into the system. Different CFD software packages such as Ansys fluent, Ansys CFX, and COMSOL have been utilized in these various applications, showing different strengths and weaknesses. This section will discuss the CFD modeling approaches used for different types of bioreactors, including the stirred tank, wave/rocking, hollow fiber, fluidized bed, airlift, rotary wall vessel, and high-aspect-ratio vessel (HARV) bioreactors (**Figure 1.1**, All tables and figures are located in the appendix). These bioreactors are typically used to grow cells in suspension with microcarriers to provide them with surfaces to attach to, except for the hollow fiber bioreactor in which the fibers act as a cell scaffold. The use of CFD models in simulating the different bioreactors is summarized in **Table 1.1**. Most of the literature pertains to tissue engineering to the lack of publicly available research on cultivated meat applications. Unlike other reviews that focus on scale-up and mention CFD as a tool (Allan et al., 2019; Karimi Alavijeh et al., 2022; Werner et al., 2014), this will focus on discussing in depth the modeling approaches taken to simulate the bioreactors, their limitations, and future directions.

2.1 Stirred Tank Bioreactor (STB)

The stirred tank bioreactor (STB, **Figure 1.1**a) is the most used bioreactor type for cell proliferation because it is the most readily available and has well-established protocols. Growing animal cells in an STB requires microcarriers to provide surfaces to the cells for attachment (Bodiou et al., 2020). The microcarrier type will determine the optimal impeller rotating speed depending closely on the impeller and vessel geometry. Enough agitation is needed for proper mixing, but too much stress could induce differentiation or damage cells (Allan et al., 2019). Adamo and García-Cardeña (2011) discussed how fluid shear stress could differentiate stem cells into specific lineages. It is well-known how cells can be damaged by shear stress in bioreactors, and extensive literature is available regarding this issue (Berdugo, 2010; Chisti, 2001; Papoutsakis, 1991). Understanding the hydrodynamic stresses and environments the cells are subjected to is critical to controlling cell production.

Many studies have used CFD to evaluate and characterize the flow patterns and stress that cells are subjected to within an STB, especially when using microcarriers (Berry et al., 2016; Delafosse et al., 2018; Ebrahimi et al., 2019; Ghasemian et al., 2020; Jossen et al., 2018; Julaey et al., 2016; Kaiser et al., 2013; Ponnuru et al., 2014; Verma et al., 2019). For example, Jossen et al. (2018) used Ansys Fluent to model 125- and 500-ml bioreactors and evaluated how different rotational speeds of impellers would change the microcarrier dispersion. They found that the suspension criteria N_{s1} – rpm required to suspend most (>99%) particles in a specific bioreactor would disperse fewer particles in a larger bioreactor. Because of this finding, it is necessary to characterize N_{s1} and other suspension criteria when scaling up production.

The CFD models also have been used to develop novel designs of impellers to improve bioreactor performance (e.g., stress profiles) (Bliatsiou et al., 2019; Ebrahimi et al., 2019; Patel et al., 2014; Ueki et al., 2021; Verma et al., 2019). For example, Patel et al., (2014) studied the velocity and shear stress profiles in an STB generated by changing the number of blades on a Rushton impeller and baffles on the bioreactor wall. They demonstrated that more blades on the Rushton impeller do not necessarily translate into higher velocities and stresses, and the number of baffles and ratio of impeller and reactor diameter significantly impact the hydrodynamic profile. Novel designs of impellers can be easily modeled with CFD to optimize them before manufacturing and assembling the system. CFD models have recently been used for simulating bioreactors larger than the typical lab scale required for industrial production that aims to reach 1000 L or more. Scully et al. (2020) used results from a validated CFD model they developed for a 2000 L bioreactor to scale up to a 5000 L single-use bioreactor for cell culture in biopharma industry. Villiger et al. (2018) modeled a 5000 L and a 15000 L bioreactor for animal cell culture and found good agreement in maximum hydrodynamic stress, mixing time, and oxygen mass transfer coefficients between their models and experimental data. Other researchers have done comprehensive CFD models of large scale spinner bioreactors (700 L) for lactic acid bacteria cultures to study the formation of pH gradients in the system (Spann et al. 2019). Haringa (2022) has developed complex models in M-Star CFD for a 54 m^3 stirred bioreactor to evaluate the effect of varying number of blades and impellers on the mixing behavior, nutrient distribution, and organism lifelines.

These CFD models also used different modeling approaches in model development. The most common approach used to calculate turbulence in STBs is to use the Reynolds Averaged Navier-Stokes (RANS) k-ε model, where k is the turbulent kinetic energy and ε is the rate of dissipation of k (Bilgen et al., 2005; Borys et al., 2018; Ebrahimi et al., 2019; Kaiser et al., 2013; Till et al., 2018). This modeling approach provides a good approximation generally accepted for industrial applications; however, it disregards the viscous sublayer, the closest layer to the wall, where velocity is known to be zero. This layer is particularly important when characterizing velocities and shear stresses affecting adherent cells. Another RANS modeling approach, the k-ω model, where ω is the specific dissipation rate, considers the viscous sublayer but typically has difficulties in converging. The Shear Stress Transport (SST) model, which combines both k-ε and k-ω, has seen more use in recent studies as a much more accurate model (Berry et al., 2016). It is more computationally intensive, but high-performance computers (HPC) allow it to be used more efficiently.

HPCs allow users to account for the microcarriers by using the Euler-Euler and Euler-Lagrange models (Berry et al., 2016; Delafosse et al., 2018; Jossen et al., 2018; Kaiser et al., 2013). These models will treat the media and microcarriers as different phases and vary in how the phases interact with each other. Using these multiphase models allows the user to simulate the volume fraction or distribution of the microcarriers within the system and their residence time. The residence time is the time the particles spend inside a controlled volume and is significant in determining how much time the cells will be in a high shear stress zone.

2.2 Wave/Rocking Bioreactor (WRB)

Another bioreactor used extensively for cell culture is the wave or rocking bioreactor (WRB, **Figure 1.1**b), which is a controlled, low-shear alternative to the STB. The WRB is a bag or container supported on a rocking platform that provides a gentle environment for cells to grow in suspension with microcarriers. The WRB can regulate the rocking angle and speed for proper and controlled mixing. However, it is mainly used for small to medium scale because its physical footprint increases drastically as the bags must be operated at 50% of their total capacity to ensure proper mixing (Marsh, 2017).

All literature surveyed in this review used the volume of fluid (VOF) method in ANSYS to characterize the WRB performance and evaluate the free fluid surface, i.e., the interface between the liquid and the air. It is necessary to track the interface properly in this type of bioreactor because the waves' motions will likely be the source of high stress. The VOF method is a Eulerian approximation that assumes the different phases are treated as immiscible and share velocity and pressure fields, thus using a single set of conservation equations. The fluxes between the phases and the location of the boundary are calculated by the volume fraction of each phase in defined regions. The volume fraction serves as a weighing function for properties such as viscosity and density. The fluid within a control region will be considered completely one of the phases or a mixture of both, depending on the value of the volume fraction (Werner et al., 2014; Zhan et al., 2019). This approach is especially helpful in keeping track of the fluid interface but depends significantly on mesh size at the boundary. A smaller mesh will allow a more accurate interface reconstruction, providing more control regions where the volume fraction will be calculated (ANSYS FLUENT 12.0 User's Guide”). The VOF method is typically compared against the level set method. The level set method is better at calculating surface tension forces but struggles with mass conservation and can be more computationally intensive (Bilger et al., 2017).

Eibl et al., (2009) characterized the fluid flow and calculated Reynold's number of different bag sizes for wave biotech's BioWave® rocking bioreactor. They argued that as culture volume – fill level – in the bags increases, headspace is lost, and wave motion is limited, reducing Reynold's number. They also tested 5, 8, and 10° and found that the 5° rocking angle resulted in the longest mixing times regardless of bag size; ~80s in the 2L bag and ~320s in the 200 L bag. WRB using cellbags of 2 and 20 L capacity were studied to understand the velocity and shear stress profiles (Öncül et al., 2010). Zhan et al., (2019) expanded upon that research by studying a 10 L cellbag filled at 50% capacity and nine rocking rates and angles combinations. They found that mixing and shear stress increase with the rocking angle but not with rocking speed. A single-use 20 L WRB was modeled at 20 rpm and 10° rocking angle to analyze the flow field, power input, turbulent energy dissipation rate, and volumetric oxygen mass transfer rates (Svay et al. 2020). This study found that large bubble entrapment and breakage happen at high rocking speeds and angles. They also correlated mass transfer coefficients to power density which can be used as a tool for scaling bag bioreactors. These models have analyzed the shear stress profiles generated by different rocking rates and angles in this bioreactor. They have shown that WRB is significantly less likely to damage cells than STB. However, these models did not include microcarriers or encapsulated cells in the simulation; they only modeled the culture media and used water-like properties.

2.3 Hollow Fiber Bioreactor (HFB)

The hollow fiber bioreactor (HFB, **Figure 1.1**c) is another alternative used for cell expansion and differentiation that mimics the blood vessels’ capability to supply nutrients and remove metabolites. Wung et al., (2014) have compiled a small list of regenerative medicine applications where HFBs were used for the proliferation and differentiation of mammalian cells. This bioreactor type has semi-permeable membranes that allow water and nutrients to flow and act as an adherent surface for cells to grow. Cells can be seeded anywhere on the surface of the fibers or in a gel in the extra capillary space (ECS), the space between the fibers. This flexibility is beneficial since each seeding location will be exposed to different shear stresses. Therefore, it is crucial to understand the hydrodynamics within HFB to know what environment the cells are growing in.

Mohebbi-Kalhori et al., (2012) modeled a 5-cm-long HFB with laminar flow as two interpenetrating porous regions; the inside of the fibers and the ECS. The porous region defines a zone with an added flow resistance or momentum sink. It is modeled as an added source term to the momentum equations composed of a viscous loss term and an inertial loss term. In this study, they analyzed the effect of membrane thickness, inner fiber radius, and inter-fiber spacing on cell volume fraction and the effect of fiber length on nutrient distribution. Their results show that these design parameters significantly affect cell growth and migration within the bioreactor. Khademi et al., (2014) conducted a similar study on a system they modified to have a hollow membrane sheet instead of separate fibers inside the bioreactor. In their study, a 3D CFD model was used to study the flow of oxygen, glucose, and lactate within the system at different flow rates, porosity, cell density, and permeability. The system was modeled with the lumens, or insides of sheets, as a homogeneous region and with the sheet membrane and ECS as a single porous region. Another study modeled a 20-fiber HFB to compare modes of media flow into the system to determine which was more optimal for mammalian cell expansion and to understand the hydrodynamics in the ECS of the bioreactor (Menshutina et al. 2020). The media inflow modalities tested were maximum flow rate into lumen space, stepwise increments in flow rate, and continuous smooth increases in flow rate as a function of time. The third mode was chosen over the rest because it allowed for more accurate control of media supply while maintaining proper permeate outflow. The direct and counter flow of medium into the system were also modeled. The direct flow of media proved to have a more uniform velocity and stress distribution with no stagnant zones, which were the main reasons to discard the counter flow. This model was validated experimentally, and a model for a scaled-up 60-fiber bioreactor was developed in which the direct inflow of media was also the best option to maintain nutrient and permeate balance.

2.4 Fluidized Bed (FBB)

The fluidized bed bioreactor (FBB, **Figure 1.1**d) has gained popularity in cell culture because it provides a well-controlled environment for cell growth. This bioreactor uses a fluid that passes through a distributor to suspend solid particles and make them behave as a fluid as well. The low shear stress and continuous media perfusion aid in culturing higher cell densities than static cell cultures (Lucena-Thomas et al., 2020). The cells, either grown on microcarriers or encapsulated in gel beads, are suspended by a constant media flow while a secondary flow removes metabolites, thus providing a stable and highly mixed environment (Runstadler et al., 1990).

The shear stress distribution, oxygen mass transfer, and particle density of a small 20-cm-high FBB were modeled using Ansys Fluent (Huang et al., 2018). The model was validated with results from the literature regarding particle velocity and volume fraction of solids within the system. A small-scale FBB was used to cultivate HepG2 cells growing encapsulated in alginate beads, and its hydrodynamics were modeled with SOLIDWORKS Flow Simulation (Mendonça da Silva et al., 2020). The sintered glass distributor at the bottom was defined as porous media in the simulation. Flow profile and shear stress at varying flow rates were analyzed, along with cell proliferation and viability. The reproducibility and flexibility shown by this system could aid in future co-culture applications. More complex models have been developed recently. For example, Ding et al., (2022) developed a two-phase model – continuous phase of water and dispersed phase of air – to characterize bubble patterns more accurately in a pulsed flow FBB.

2.5 Air-Lift Bioreactor (ALB)

The air-lift bioreactor (ALB, **Figure 1.1**e) uses sparged gas from the bottom to create an upwards flow in a section called the riser. Once the fluid reaches the top it recirculates downwards in a section called the downcomer that is parallel to the riser. This creates a recirculation of the fluid inside that provides more homogeneous shear stress distribution than the STB and has comparable mixing and mass transfer rates (Wadaugsorn et al., 2016). The ALB has been typically used for wastewater treatment

(Ahmadi et al., 2020; Liu et al., 2021), bacterial fermentation (Singhania et al., 2022), and plant cell culture (Han et al., 2022). Unlike the FBB, the ALB can operate with a much lower solids load and typically has a recirculating loop.

Their application for large-scale production of cultivated meat has been extensively discussed as they do not have any moving parts and generate homogeneous environments. Li et al. (2020), used ANSYS fluent to develop a CFD model to optimize reactor geometry and reduce gas entrainment and flow maldistribution in a 300 m^3 bioreactor that could theoretically feed 75,000 people. These characteristics have made FBB and ALB strong candidates for scaling up mammalian cell culture for cultivated meat. Nadal-Rey et al. (2022) developed a comprehensive comparison of STBs and ALBs with working volumes of 40, 60 and 90 m^3. They concluded that ALBs have mixing times up to 10x shorter than STBs probably due to a more uniform distribution of turbulent eddies.

The ALB must not be confused with bubble column bioreactors as these do not have any divisions in them or recirculation. They work similarly to the FBB but use sparged gases to cause the fluidization of the particles inside. Bubble column bioreactors, however, have also been used for cell and bacterial cultures. McClure et al. (2016) performed an extensive characterization of the performance of a bubble column bioreactor using ANSYS CFX to model the system. They modeled a 0.2 m^3 bioreactor and evaluated oxygen transfer rates, sugar concentrations, and particle distribution after addition of a tracer at varying locations.

2.6 Rotary Wall Vessel (RWV) and High-Aspect Ratio Vessel (HARV)

The Rotary Wall Vessel (RWV, **Figure 1.1**f) and the High-Aspect Ratio vessel (HARV, **Figure 1.1**g) are two low-shear alternatives. RWV is a system consisting of two concentric cylinders, and cells are grown in the media space in between. When both cylinders rotate at the same speed, the system provides high oxygen mass transfer rates but considerably lower shear stresses (0.13 $dyne/cm^2$) than the STB (Cinbiz et al., 2010). HARVs are cylindrical single-layer vessels with a high aspect ratio of diameter to length, which translates to a thin and spread-out layer of media. In contrast, the rotary wall vessel is a cylinder capped at both ends and can have either inside or outside wall rotating. Single-use versions of all these bioreactors have become increasingly popular as they decrease the chances of contamination and eliminate the need for thorough cleaning and disinfection (Consolo et al., 2012). However, current systems do not have sensors that accurately describe the stresses experienced inside this vessel, making CFD a crucial tool in designing the appropriate vessel dimensions and processing parameters. This bioreactor type could prove useful for scale-down research to evaluate the effect of shear stress on cell cultures as shear stress can be precisely controlled, and turbulent flow can easily be induced (Ghasemian et al., 2020).

Cinbiz et al., (2010) modeled a Rotary Culture MW™ bioreactor with scaffolds for cartilage tissue growth using Ansys fluent. They analyzed the velocity and shear stress profiles at varying rotational speeds and compared results against values found in the literature for other bioreactor types. Other authors have focused on modeling cells encapsulated in alginate beads and studied the effect of the volume fraction of the beads (Consolo et al., 2012) and glucose concentration (Teo et al., 2014) on the flow and stress profiles within the system. Both studies used experimental data to validate their models and explored cardiac gene expression. Ghasemian et al., (2020) used Ansys CFX to model the fluid dynamics and evaluate the shear stress profile of an RWB and a spinner flask. Not only did the rotary wall generate lower overall shear stress, but also the range of stresses present in the entirety of the vessel was much smaller than those present in the spinner flask.

Consolo et al., (2012) modeled the High Aspect Ratio Vessel (HARV), a small vessel used to deliver well-controlled stresses to cells grown inside by rotating the single-layer wall. It was initially developed by NASA to mimic microgravity environments but has slowly gained popularity in different tissue culture applications. Teo et al., (2014) comprehensively compared the transport of nutrients from the media to a culture encapsulated in a hydrogel in typical T-flasks, a HARV, and an RWV. This study showed the HARV, and the RWV reached equilibrium within 15 - 30 s while the static culture presented a drastic gradient. One of the few studies using COMSOL Multiphysics to model any bioreactor explored the growth kinetics of Chinese hamster ovary cells in a

HARV and showed model results for volume fraction, velocity profile, and glucose distribution inside the system (Chao and Das, 2015). Results implied that cells might accumulate in the middle of the bioreactor but that the nutrient concentration is well-mixed. The proper and fast mixing of nutrients provided by the HARV and RWV is beneficial for cell proliferation and aggregation.

2.7 Summary of bioreactor CFD modeling in cell culturing

The CFD models presented in this section are meant to show the usefulness of CFD for cell cultures. Single phase models can be used as a good initial guess of the hydrodynamics within a bioreactor. However, the multiphase models such as Euler-Euler allow to properly simulate microcarrier or encapsulated cell culture as shown in some of the most recent articles for every bioreactor. The multiphase models help better quantify the distribution and residence time within high shear stress zones which are known to induce differentiation or damage cells. Turbulence models such as k-ε or k-ω, which are used in most models presented, are very useful to characterize the shear stresses and fluid profiles within the bioreactors. They can also be used as initial step for more complex LES models which are able to capture smaller Kolmogorov scale eddies as shown by Berry et al. (2016). On the other hand, simpler models like the VOF provide a good enough estimate for WRBs as the main source of shear stress and damage to cells is the interface between media and air.

The different models show many differences between the bioreactor types and specific values for oxygen mass transfer coefficient, mixing time, shear stress, and Kolmogorov length can be found in **Table 1.1** for those studies who provided such data. The STB has a wide range of shear stress that varies greatly depending on impeller and vessel design as well as scale; it is typically used as the point of comparison since it is the most used. The ALB are next because of the detrimental effect of their bubbles on the cells. The other bioreactors, however, tend to provide gentler environments without compromising mixing time as much, except for the WRB which is the design that has the longest mixing time of all. HFBs are the most efficient bioreactors in terms of media consumption and metabolite removal. Their scale-up however, is still very limited due to the cost of the membrane materials. Finally, the RWV and HARV bioreactors are great designs for high cell densities and aggregation, however, more comprehensive CFD models should be developed for industrial-scale versions of them to assess their feasibility since only lab-scale and milliliter-scale models exist at this moment.

3 Limitations and potential applications of CFD in cultivated meat production

CFD has proven to be a very useful tool to characterize the hydrodynamic environment inside different types of bioreactors. The CFD models were developed in various ways to understand the performance of cell culture bioreactors. Most of these models were developed for tissue engineering applications and need improvement to enable their applicability for cultivated meat applications.

First, the CFD models must be improved to incorporate more accurate material properties for cultivated meat applications. Most models used significantly simplified fluid properties by using constant water density and viscosity values. However, it is known that culture medium supplemented with fetal bovine serum (FBS) has slight non-Newtonian behavior (Wyma et al., 2018). Recently, the cell culture was characterized at different stages of cell growth and identified that as the culture progresses, a non-Newtonian shear thinning behavior is more apparent (Poon, 2022). The shear stress values simulated in the model would be much higher than those obtained when using the constant water-like Newtonian values (Wyma et al., 2018). Characterizing and implementing dynamic non-Newtonian behaviors for the media in future models will be necessary to fine-tune processing parameters, especially since cultivated meat requires a much higher cell density than conventional cell culture. Characterization and inclusion of dynamic properties will be especially useful as serum-free media has started to replace regular media. Replacing serum for various combinations of supplements will most likely change the rheological behavior of the cell culture.

In addition to incorporating the dynamic cell culture media properties, the CFD models for cultivated meat cell cultures need to describe the multiple phases in bioreactors. In cell cultures, the Stokes numbers of cells (and microcarriers) are very small due to their small diameter and density close to the media, indicating that the cells will flow along with the streamline of culture media during mixing. Single phase CFD model is a good initial approximation of the cell cultures. However, complicated multiple phase model may be more useful for complicated scenarios, such as cell growth on microcarriers, cell aggregations and gas bubbles inside the bioreactors. Multiphase models, Euler-Lagrange or Euler-Euler approximations can better describe the effect of flow on the microcarriers and cells in suspension. Euler-Lagrange tracks the solid particles but becomes very computationally intensive when trying to model the actual microcarrier amount. Euler-Euler, on the other hand, will treat each phase as continuous media, and therefore one cannot occupy the volume of the other (Kelly, 2008). Nevertheless, multiphase models are becoming increasingly popular as different microcarriers or alternatives such as alginate encapsulation are developed, and more powerful computers are becoming available. Greater detail and accuracy of the model translate directly into a higher computational cost. However, a dynamic compartment modeling approach was recently suggested as an alternative to speed up simulations without sacrificing accuracy (Nadal-Rey et al., 2021).

Third, the CFD model must be better developed and used to evaluate cell-scale fluid behavior. A parameter that can be calculated from CFD results that tends to get overlooked in these models is the Kolmogorov turbulent eddy scale or length. Experimental determination of the Kolmogorov scales is challenging as it is a function of the kinematic fluid viscosity and the local energy dissipation rate (Czermak et al., 2009). It is considered that when the turbulent eddies are about two-thirds the size of the microcarriers, they can damage cells. If eddies are larger than the microcarriers, they will rotate with the flow reducing the effect of forces on the surface. However, when the eddies are smaller, the microcarriers would not move; instead, the cells growing on them would experience the force of the eddies (Croughan et al., 2000). For example, Human fibroblasts are damaged when the Kolmogorov length scale is below 125 μm, and chicken embryo cells are damaged when this value falls below 100 μm (Chisti, 2001). It is known that higher rotational speeds in an STB will make smaller eddies and have higher local shear stress values (Jossen et al., 2018), but this depends significantly on the bioreactor geometry and impeller design. Typical RANS methods like *k*-*ε* will provide some insight into the eddies. However, Large Eddies Simulation (LES) methods have recently gained popularity for their increased resolution at the smallest scale. This modeling approach has not yet been widely used in modeling cell culture applications (Berry et al., 2016).

CFD has great potential to be integrated with other modeling approaches to understand the cultivated meat cell culturing process at multiple scales. CFD alone has been developed to provide useful information about the physical environment that the cells experience during their expansion and differentiation stages at the bioreactor scale. However, the cell behaviors of metabolism, adhesion, proliferation, and differentiation at the cellular scale determine the final cell culture yield. Thus, it is vital to understand the relationship between the bioreactor environment and cell culture behaviors. A comprehensive approach that couples CFD with other modeling methods, such as Agent-Based Modeling (ABM), was recently explored to capture the entire system at macro and micro scales. Van Liedekerke et al., (2015) presented multiple ABM models to evaluate cell growth, attachment, and deformation in tissue engineering. Kaul et al., (2013) coupled CFD with ABM to model cell growth and nutrient consumption within a scaffold bioreactor. The coupled models informed each other, so cell behavior and bioreactor environment would update simultaneously. More recently, Corti et al., (2020) used Ansys Fluent to model the fluid dynamics of a superficial femoral artery and calculate the shear stress. This stress was then used to inform the ABM model implemented in MATLAB to study atherosclerotic plaque generation. However, no research was found during the development of this review regarding using this coupled approach to mode cell culture for cultivated meat purposes.

CFD models can be improved with machine learning (ML) for faster, high-accuracy simulations and advanced turbulence models (Vinuesa and Brunton 2022). Kochkov et al. (2021) used a convolutional neural network (CNN) to speed up Direct Numerical Simulations (DNS) and Large Eddy Simulations (LES), achieving up to 40x acceleration. ML can also verify new models through post-processing (Wang and Wang 2021). Coarse-grid CFD correction is a data-driven ML approach that reduces computational time and cost. Pirnia et al. (2019) used it to predict drag force on granular materials. Hanna et al. (2020) used ANN and RF models to predict high-accuracy results from a new CFD model. CNN models have been used for super-resolution, predicting high-resolution images from low-resolution ones (Dong et al. 2016). Fukami et al. (2019) and Liu et al. (2020) used CNN for super-resolution reconstruction of turbulent flow fields, demonstrating its capability in reconstructing high-resolution laminar and turbulent flow fields from low-resolution data.

4 Conclusion

Although CFD modeling has been widely used for simulating bioreactors for various applications, including cell cultures, very few applied in cultivated meat processing. This review summarizes the use of CFD modeling in understanding hydrodynamic behaviors of fluid flow in six types of cell culture bioreactors and discusses the potential and limitations of current CFD models for cultivated meat production. Future research can focus on: 1) improving model accuracy by incorporating dynamic properties of cell cultures, 2) enhancing model efficiency and applicability by using various modeling strategies (e.g., multiphase modeling, compartment modeling, LES), and 3) expanding modeling capability by integrating with other modeling approaches, such as ABM and machine learning algorithms. Ideally, models will evolve to a point where the industry can easily change cell lines, media, and processing parameters on the model and quickly generate all the information they need to optimize their process.

REFERENCES

Adamo, L., & García-Cardeña, G. (2011). Directed stem cell differentiation by fluid mechanical forces. *Antioxidants & Redox Signaling*, *15*(5), 1463–1473. https://doi.org/10.1089/ars.2011.3907

Allan, S. J., De Bank, P. A., & Ellis, M. J. (2019). Bioprocess Design Considerations for Cultured Meat Production With a Focus on the Expansion Bioreactor. *Frontiers in Sustainable Food Systems*, *3*. https://www.frontiersin.org/article/10.3389/fsufs.2019.00044. Accessed 26 January 2022

ANSYS FLUENT 12.0 User's Guide. (n.d.). https://www.afs.enea.it/project/neptunius/docs/fluent/html/ug/main_pre.htm. Accessed 4 August 2022

Berdugo, C. (2010). Cell Damage Mechanisms and Stress Response in Animal Cell Culture. The Ohio State University.

Berry, J. D., Liovic, P., Šutalo, I. D., Stewart, R. L., Glattauer, V., & Meagher, L. (2016). Characterisation of stresses on microcarriers in a stirred bioreactor. *Applied Mathematical Modelling*, *40*(15), 6787–6804. https://doi.org/10.1016/j.apm.2016.02.025

Bilgen, B., Chang-Mateu, I. M., & Barabino, G. A. (2005). Characterization of mixing in a novel wavy-walled bioreactor for tissue engineering. *Biotechnology and Bioengineering*, *92*(7), 907–919. https://doi.org/10.1002/bit.20667

Bilger, C., Aboukhedr, M., Vogiatzaki, K., & Cant, R. S. (2017). Evaluation of two-phase flow solvers using Level Set and Volume of Fluid methods. *Journal of Computational Physics*, *345*, 665–686. https://doi.org/10.1016/j.jcp.2017.05.044

Bliatsiou, C., Malik, A., Böhm, L., & Kraume, M. (2019). Influence of Impeller Geometry on Hydromechanical Stress in Stirred Liquid/Liquid Dispersions. *Industrial & Engineering Chemistry Research*, *58*(7), 2537–2550. https://doi.org/10.1021/acs.iecr.8b03654

Bodiou, V., Moutsatsou, P., & Post, M. J. (2020). Microcarriers for Upscaling Cultured Meat Production. *Frontiers in Nutrition*, *7*. https://doi.org/10.3389/fnut.2020.00010

Borys, B. S., Roberts, E. L., Le, A., & Kallos, M. S. (2018). Scale-up of embryonic stem cell aggregate stirred suspension bioreactor culture enabled by computational fluid dynamics modeling. *Biochemical Engineering Journal*, *133*, 157–167. https://doi.org/10.1016/j.bej.2018.02.005

Catapano, G., Czermak, P., Eibl, R., Eibl, D., & Pörtner, R. (2009). Bioreactor Design and Scale-Up. In R. Eibl, D. Eibl, R. Pörtner, G. Catapano, & P. Czermak (Eds.), *Cell and Tissue Reaction Engineering: With a Contribution by Martin Fussenegger and Wilfried Weber* (pp. 173–259). Berlin, Heidelberg: Springer. https://doi.org/10.1007/978-3-540-68182-3_5

Chao, T.-C., & Das, D. B. (2015). Numerical simulation of coupled cell motion and nutrient transport in NASA's rotating bioreactor. *Chemical Engineering Journal*, *259*, 961–971. https://doi.org/10.1016/j.cej.2014.08.077

Chisti, Y. (2001). Hydrodynamic Damage to Animal Cells. *Critical Reviews in Biotechnology*, *21*(2), 67–110. https://doi.org/10.1080/20013891081692

Cinbiz, M. N., Tığlı, R. S., Beşkardeş, I. G., Gümüşderelioğlu, M., & Çolak, Ü. (2010). Computational fluid dynamics modeling of momentum transport in rotating wall perfused bioreactor for cartilage tissue engineering. *Journal of Biotechnology*, *150*(3), 389–395. https://doi.org/10.1016/j.jbiotec.2010.09.950

Consolo, F., Bariani, C., Mantalaris, A., Montevecchi, F., Redaelli, A., & Morbiducci, U. (2012). Computational modeling for the optimization of a cardiogenic 3D bioprocess of encapsulated embryonic stem cells. *Biomechanics and Modeling in Mechanobiology*, *11*(1), 261–277. https://doi.org/10.1007/s10237-011-0308-0

Corti, A., Chiastra, C., Colombo, M., Garbey, M., Migliavacca, F., & Casarin, S. (2020). A fully coupled computational fluid dynamics – agent-based model of atherosclerotic plaque development: Multiscale modeling framework and parameter sensitivity analysis. *Computers in Biology and Medicine*, *118*, 103623. https://doi.org/10.1016/j.compbiomed.2020.103623

Croughan, M. S., Hamel, J.-F., & Wang, D. I. C. (2000). Hydrodynamic effects on animal cells grown in microcarrier cultures. *Biotechnology and Bioengineering*, *67*(6), 841–852. https://doi.org/10.1002/(SICI)1097-0290(20000320)67:6<841::AID-BIT19>3.0.CO;2-K

Czermak, P., Pörtner, R., & Brix, A. (2009). Special Engineering Aspects. In R. Eibl, D. Eibl, R. Pörtner, G. Catapano, & P. Czermak (Eds.), *Cell and Tissue Reaction Engineering: With a Contribution by Martin Fussenegger and Wilfried Weber* (pp. 83–172). Berlin, Heidelberg: Springer. https://doi.org/10.1007/978-3-540-68182-3_4

Delafosse, A., Loubière, C., Calvo, S., Toye, D., & Olmos, E. (2018). Solid-liquid suspension of microcarriers in stirred tank bioreactor – Experimental and numerical analysis. *Chemical Engineering Science*, *180*, 52–63. https://doi.org/10.1016/j.ces.2018.01.001

Ding, Z., Tiwari, S. S., Tyagi, M., & Nandakumar, K. (2022). Computational fluid dynamic simulations of regular bubble patterns in pulsed fluidized beds using a two-fluid model. *The Canadian Journal of Chemical Engineering*, *100*(2), 405–422. https://doi.org/10.1002/cjce.24082

Dong, C., Loy, C.C., He, K., Tang, X., 2016. Image Super-Resolution Using Deep Convolutional Networks. IEEE Transactions on Pattern Analysis and Machine Intelligence 38, 295–307. https://doi.org/10.1109/TPAMI.2015.2439281

Ebrahimi, M., Tamer, M., Villegas, R. M., Chiappetta, A., & Ein-Mozaffari, F. (2019). Application of CFD to Analyze the Hydrodynamic Behaviour of a Bioreactor with a Double Impeller. *Processes*, *7*(10), 694. https://doi.org/10.3390/pr7100694

Eibl, R., Werner, S., & Eibl, D. (2009). Bag Bioreactor Based on Wave-Induced Motion: Characteristics and Applications. *Advances in biochemical engineering/biotechnology*, *115*, 55–87. https://doi.org/10.1007/10_2008_15

Fukami, K., Fukagata, K., Taira, K., 2019. Super-resolution reconstruction of turbulent flows with machine learning. J. Fluid Mech. 870, 106–120. https://doi.org/10.1017/jfm.2019.238

Ghasemian, M., Layton, C., Nampe, D., zur Nieden, N. I., Tsutsui, H., & Princevac, M. (2020). Hydrodynamic characterization within a spinner flask and a rotary wall vessel for stem cell culture. *Biochemical Engineering Journal*, *157*, 107533. https://doi.org/10.1016/j.bej.2020.107533

Hanna, B.N., Dinh, N.T., Youngblood, R.W., Bolotnov, I.A., 2020. Machine-learning based error prediction approach for coarse-grid Computational Fluid Dynamics (CG-CFD). Progress in Nuclear Energy 118, 103140. https://doi.org/10.1016/j.pnucene.2019.103140

Haringa, C. (2022). An analysis of organism lifelines in an industrial bioreactor using Lattice-Boltzmann CFD. *Engineering in Life Sciences*, *n/a*(n/a). https://doi.org/10.1002/elsc.202100159

Huang, Z., Odeleye, A. O. O., Ye, H., Cui, Z., & Yang, A. (2018). Fluid dynamic characterization of a fluidized-bed perfusion bioreactor with CFD–DEM simulation. *Journal of Chemical Technology & Biotechnology*, *93*(8), 2316–2330. https://doi.org/10.1002/jctb.5576

Jossen, V., Eibl, R., Kraume, M., & Eibl, D. (2018). Growth Behavior of Human Adipose Tissue-Derived Stromal/Stem Cells at Small Scale: Numerical and Experimental Investigations. *Bioengineering*, *5*(4). https://doi.org/10.3390/bioengineering5040106

Julaey, M., Hosseini, M., & Amani, H. (2016). Stem Cells Culture Bioreactor Fluid Flow, Shear Stress and Microcarriers Dispersion Analysis Using Computational Fluid Dynamics. *Journal of Applied Biotechnology Reports*, *3*(2), 425–431.

Kaiser, S., Jossen, V., Schirmaier, C., Eibl, D., Brill, S., van den Bos, C., & Eibl, R. (2013). Fluid Flow and Cell Proliferation of Mesenchymal Adipose-Derived Stem Cells in Small-Scale, Stirred, Single-Use Bioreactors. *Chemie Ingenieur Technik*, *85*(1–2), 95–102. https://doi.org/10.1002/cite.201200180

Karimi Alavijeh, M., Baker, I., Lee, Y. Y., & Gras, S. L. (2022). Digitally enabled approaches for the scale up of mammalian cell bioreactors. *Digital Chemical Engineering*, *4*, 100040. https://doi.org/10.1016/j.dche.2022.100040

Kaul, H., Cui, Z., & Ventikos, Y. (2013). A Multi-Paradigm Modeling Framework to Simulate Dynamic Reciprocity in a Bioreactor. *PLOS ONE*, *8*(3), e59671. https://doi.org/10.1371/journal.pone.0059671

Kelly, W. J. (2008). Using computational fluid dynamics to characterize and improve bioreactor performance. *Biotechnology and Applied Biochemistry*, *49*(4), 225–238. https://doi.org/10.1042/BA20070177

Khademi, R., Mohebbi-Kalhori, D., & Hadjizadeh, A. (2014). Computational study of culture conditions and nutrient supply in a hollow membrane sheet bioreactor for large-scale bone tissue engineering. *Journal of Artificial Organs*, *17*(1), 69–80. https://doi.org/10.1007/s10047-013-0732-2

Kochkov, D., Smith, J.A., Alieva, A., Wang, Q., Brenner, M.P., Hoyer, S., 2021. Machine learning–accelerated computational fluid dynamics. Proc. Natl. Acad. Sci. U.S.A. 118, e2101784118. https://doi.org/10.1073/pnas.2101784118

Li, X., Zhang, G., Zhao, X., Zhou, J., Du, G., & Chen, J. (2020). A conceptual air-lift reactor design for large scale animal cell cultivation in the context of in vitro meat production. *Chemical Engineering Science*, *211*, 115269. https://doi.org/10.1016/j.ces.2019.115269

Liu, B., Tang, J., Huang, H., Lu, X.-Y., 2020. Deep learning methods for super-resolution reconstruction of turbulent flows. Physics of Fluids 32, 025105. https://doi.org/10.1063/1.5140772

Lucena-Thomas, J. P. de, Boonprasirt, P., Luetchford, K., De Bank, P., & Ellis, M. (2020). Bed expansion properties of tissue engineering particles in a fluidised bed bioreactor. *Biochemical Engineering Journal*, *160*, 107632. https://doi.org/10.1016/j.bej.2020.107632

Lynch, J., & Pierrehumbert, R. (2019). Climate Impacts of Cultured Meat and Beef Cattle. *Frontiers in Sustainable Food Systems*, *3*. https://www.frontiersin.org/article/10.3389/fsufs.2019.00005. Accessed 26 January 2022

Marsh, D. T. J. (2017, January 28). Engineering Characterisation of a Rocked Bag Bioreactor for Improved Process Development and Scale-Up (Doctoral). Doctoral thesis, UCL (University College London). Doctoral presented at the UCL (University College London), UCL (University College London). Retrieved from https://discovery.ucl.ac.uk/id/eprint/1534658/

Mattick, C. S. (2018). Cellular agriculture: The coming revolution in food production. *Bulletin of the Atomic Scientists*, *74*(1), 32–35. https://doi.org/10.1080/00963402.2017.1413059

Mattick, C. S., Landis, A. E., Allenby, B. R., & Genovese, N. J. (2015). Anticipatory Life Cycle Analysis of In Vitro Biomass Cultivation for Cultured Meat Production in the United States. *Environmental Science & Technology*, *49*(19), 11941–11949. https://doi.org/10.1021/acs.est.5b01614

McClure, D. D., Kavanagh, J. M., Fletcher, D. F., & Barton, G. W. (2016). Characterizing bubble column bioreactor performance using computational fluid dynamics. *Chemical Engineering Science*, *144*, 58–74. https://doi.org/10.1016/j.ces.2016.01.016

Mendonça da Silva, J., Erro, E., Awan, M., Chalmers, S.-A., Fuller, B., & Selden, C. (2020). Small-Scale Fluidized Bed Bioreactor for Long-Term Dynamic Culture of 3D Cell Constructs and in vitro Testing. *Frontiers in Bioengineering and Biotechnology*, *8*. https://www.frontiersin.org/article/10.3389/fbioe.2020.00895. Accessed 9 February 2022

Menshutina, N. V., Guseva, E. V., Safarov, R. R., & Boudrant, J. (2020). Modelling of hollow fiber membrane bioreactor for mammalian cell cultivation using computational hydrodynamics. *Bioprocess and Biosystems Engineering*, *43*(3), 549–567. https://doi.org/10.1007/s00449-019-02249-9

Mohebbi-Kalhori, D., Behzadmehr, A., Doillon, C. J., & Hadjizadeh, A. (2012). Computational modeling of adherent cell growth in a hollow-fiber membrane bioreactor for large-scale 3-D bone tissue engineering. *Journal of Artificial Organs*, *15*(3), 250–265. https://doi.org/10.1007/s10047-012-0649-1

Nadal-Rey, G., McClure, D. D., Kavanagh, J. M., Cassells, B., Cornelissen, S., Fletcher, D. F., & Gernaey, K. V. (2021). Development of dynamic compartment models for industrial aerobic fed-batch fermentation processes. *Chemical Engineering Journal*, *420*, 130402. https://doi.org/10.1016/j.cej.2021.130402

Nadal-Rey, G., McClure, D. D., Kavanagh, J. M., Cassells, B., Cornelissen, S., Fletcher, D. F., & Gernaey, K. V. (2022). Computational fluid dynamics modelling of hydrodynamics, mixing and oxygen transfer in industrial bioreactors with Newtonian broths. *Biochemical Engineering Journal*, *177*, 108265. https://doi.org/10.1016/j.bej.2021.108265

OECD, Food, & Nations, A. O. of the U. (2021). *OECD-FAO Agricultural Outlook 2021-2030*. https://doi.org/10.1787/19428846-en

Öncül, A. A., Kalmbach, A., Genzel, Y., Reichl, U., & Thévenin, D. (2010). Characterization of flow conditions in 2 L and 20 L wave bioreactors® using computational fluid dynamics. *Biotechnology Progress*, *26*(1), 101–110. https://doi.org/10.1002/btpr.312

Papoutsakis, E. (1991). Fluid-mechanical damage of animal cells in bioreactors. *Trends in Biotechnology*, *9*(1), 427–437. https://doi.org/10.1016/0167-7799(91)90145-8

Patel, P., Vaidya, P., & Singh, G. (2014). An overview of impellers, velocity profile and reactor design. Presented at the 2014 COMSOL Conference, Bangalore.

Pirnia, P., Duhaime, F., Ethier, Y., Dubé, J.-S., 2019. Drag Force Calculations in Polydisperse DEM Simulations with the Coarse-Grid Method: Influence of the Weighting Method and Improved Predictions Through Artificial Neural Networks. Transp Porous Med 129, 837–853. https://doi.org/10.1007/s11242-019-01308-9

Ponnuru, K., Wu, J., Ashok, P., Tzanakakis, E., & Furlani, E. (2014). Analysis of stem cell culture performance in a microcarrier bioreactor system. *Technical Proceedings of the 2014 NSTI Nanotechnology Conference and Expo, NSTI-Nanotech 2014*, *2*, 132–135.

Poon, C. (2022). Measuring the density and viscosity of culture media for optimized computational fluid dynamics analysis of in vitro devices. *Journal of the Mechanical Behavior of Biomedical Materials*, *126*, 105024. https://doi.org/10.1016/j.jmbbm.2021.105024

Post, M. J. (2014). Cultured beef: medical technology to produce food. *Journal of the Science of Food and Agriculture*, *94*(6), 1039–1041. https://doi.org/10.1002/jsfa.6474

Post, M. J., Levenberg, S., Kaplan, D. L., Genovese, N., Fu, J., Bryant, C. J., et al. (2020). Scientific, sustainability and regulatory challenges of cultured meat. *Nature Food*, *1*(7), 403–415. https://doi.org/10.1038/s43016-020-0112-z

Runstadler, P. W., Tung, A. S., Hayman, E. G., Ray, N. G., Sample, J. V. G., & Delucia, D. E. (1990). Continuous Culture with Macroporous Matrix, Fluidized Bed Systems. In *Large-Scale Mammalian Cell Culture Technology*. Routledge.

Scully, J., Considine, L. B., Smith, M. T., McAlea, E., Jones, N., O'Connell, E., et al. (2020). Beyond heuristics: CFD-based novel multiparameter scale-up for geometrically disparate bioreactors demonstrated at industrial 2kL–10kL scales. *Biotechnology and Bioengineering*, *117*(6), 1710–1723. https://doi.org/10.1002/bit.27323

Smetana, S., Mathys, A., Knoch, A., & Heinz, V. (2015). Meat alternatives: life cycle assessment of most known meat substitutes. *The International Journal of Life Cycle Assessment*, *20*(9), 1254–1267. https://doi.org/10.1007/s11367-015-0931-6

Spann, R., Glibstrup, J., Pellicer-Alborch, K., Junne, S., Neubauer, P., Roca, C., et al. (2019). CFD predicted pH gradients in lactic acid bacteria cultivations. *Biotechnology and Bioengineering*, *116*(4), 769–780. https://doi.org/10.1002/bit.26868

Svay, K., Urrea, C., Shamlou, P. A., & Zhang, H. (2020). Computational fluid dynamics analysis of mixing and gas–liquid mass transfer in wave bag bioreactor. *Biotechnology Progress*, *36*(6), e3049. https://doi.org/10.1002/btpr.3049

Teo, A., Mantalaris, A., Song, K., & Lim, M. (2014). A novel perfused rotary bioreactor for cardiomyogenesis of embryonic stem cells. *Biotechnology Letters*, *36*(5), 947–960. https://doi.org/10.1007/s10529-014-1456-y

Till, Z., Molnár, B., Egedy, A., & Varga, T. (2018). CFD Based Qualification of Mixing Efficiency of Stirred Vessels. *Periodica Polytechnica Chemical Engineering*, *63*(1), 226–238. https://doi.org/10.3311/PPch.12245

Tuomisto, H. L., & Teixeira de Mattos, M. J. (2011). Environmental Impacts of Cultured Meat Production. *Environmental Science & Technology*, *45*(14), 6117–6123. https://doi.org/10.1021/es200130u

Ueki, M., Tansho, N., Sato, M., Kanamori, H., & Kato, Y. (2021). Improved cultivation of Chinese hamster ovary cells in bioreactor with reciprocal mixing. *Journal of Bioscience and Bioengineering*, *132*(5), 531–536. https://doi.org/10.1016/j.jbiosc.2021.08.003

Van Liedekerke, P., Palm, M. M., Jagiella, N., & Drasdo, D. (2015). Simulating tissue mechanics with agent-based models: concepts, perspectives and some novel results. *Computational Particle Mechanics*, *2*(4), 401–444. https://doi.org/10.1007/s40571-015-0082-3

Verma, R., Mehan, L., Kumar, R., Kumar, A., & Srivastava, A. (2019). Computational fluid dynamic analysis of hydrodynamic shear stress generated by different impeller combinations in stirred bioreactor. *Biochemical Engineering Journal*, *151*, 107312. https://doi.org/10.1016/j.bej.2019.107312

Villiger, T. K., Neunstoecklin, B., Karst, D. J., Lucas, E., Stettler, M., Broly, H., et al. (2018). Experimental and CFD physical characterization of animal cell bioreactors: From micro- to production scale. *Biochemical Engineering Journal*, *131*, 84–94. https://doi.org/10.1016/j.bej.2017.12.004

Vinuesa, R., Brunton, S.L., 2022. Enhancing computational fluid dynamics with machine learning. Nat Comput Sci 2, 358–366. https://doi.org/10.1038/s43588-022-00264-7

Wadaugsorn, K., Limtrakul, S., Vatanatham, T., & Ramachandran, P. A. (2016). Hydrodynamic behaviors and mixing characteristics in an internal loop airlift reactor based on CFD simulation. *Chemical Engineering Research and Design*, *113*, 125–139. https://doi.org/10.1016/j.cherd.2016.07.017

Wang, B., Wang, J., 2021. Application of Artificial Intelligence in Computational Fluid Dynamics. Ind. Eng. Chem. Res. 60, 2772–2790. https://doi.org/10.1021/acs.iecr.0c05045

Werner, S., Kaiser, S. C., Kraume, M., & Eibl, D. (2014). Computational fluid dynamics as a modern tool for engineering characterization of bioreactors. *Pharmaceutical Bioprocessing*, *2*(1), 85–99.

Wung, N., Acott, S. M., Tosh, D., & Ellis, M. J. (2014). Hollow fibre membrane bioreactors for tissue engineering applications. *Biotechnology Letters*, *36*(12), 2357–2366. https://doi.org/10.1007/s10529-014-1619-x

Wyma, A., Martin-Alarcon, L., Walsh, T., Schmidt, T. A., Gates, I. D., & Kallos, M. S. (2018). Non-Newtonian rheology in suspension cell cultures significantly impacts bioreactor shear stress quantification. *Biotechnology and Bioengineering*, *115*(8), 2101–2113. https://doi.org/10.1002/bit.26723

Zhan, C., Hagrot, E., Brandt, L., & Chotteau, V. (2019). Study of hydrodynamics in wave bioreactors by computational fluid dynamics reveals a resonance phenomenon. *Chemical Engineering Science*, *193*, 53–65. https://doi.org/10.1016/j.ces.2018.08.017

Zhang, G., Zhao, X., Li, X., Du, G., Zhou, J., & Chen, J. (2020). Challenges and possibilities for bio-manufacturing cultured meat. *Trends in Food Science & Technology*, *97*, 443–450. https://doi.org/10.1016/j.tifs.2020.01.026

Zhang, J., Li, X., Liu, H., Zhou, J., Chen, J., & Du, G. (2021). Hydrodynamics and mass transfer in spinner flasks: Implications for large scale cultured meat production. *Biochemical Engineering Journal*, *167*, 107864. https://doi.org/10.1016/j.bej.2020.107864

APPENDIX

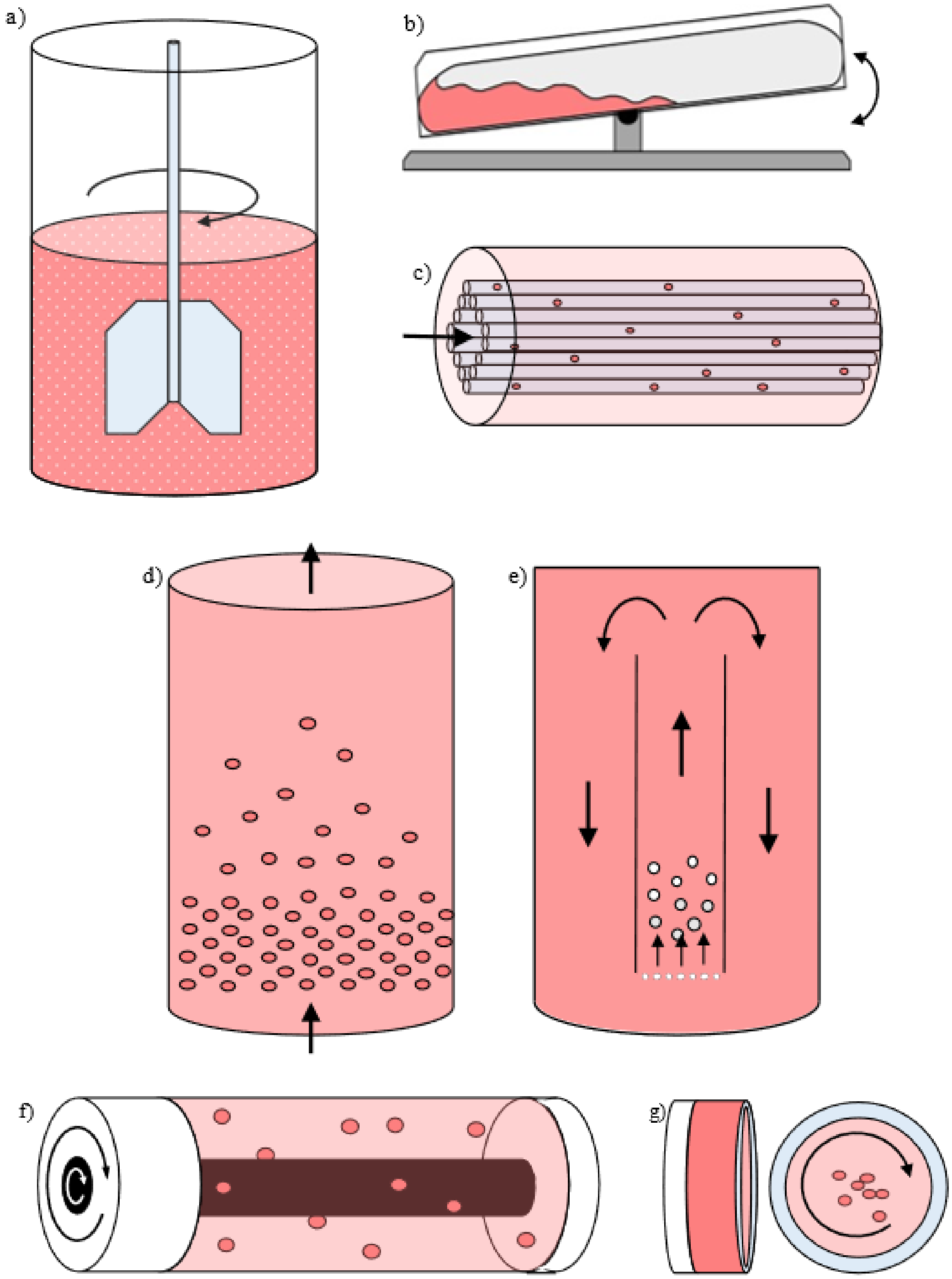

Figure 1.1. Sketches of (a) stirred tank, (b) wave/rocking, (c) hollow fiber, (d) fluidized bed, (e) airlift, (f) rotary wall bioreactors and (g) high-aspect ratio vessel.

Table 1.1. CFD models for different bioreactor types to optimize cell expansion for tissue engineering applications.

Reference	Bioreactor parameters	Media properties	Physics/Gov. Equations	Validation of CFD Results	Modeling software	Study Findings
Stirred Tank Bioreactor (STB)						
Bilgen et al., 2005	rpm = 50 Vol = 120 and 250 ml	$\rho = 1020$ kg/m^3 $\mu = 0.98$ mPa·s	Turbulent flow (k-ε)	PIV measurements	Ansys Fluent	Wavy walled had similar average shear stress (0.1 Pa) but better mixing than normal STB (10 vs 15 s).
Kaiser et al., 2012	rpm = 50, 60, 75, 82, 105 Vol = 125 ml	N/A	Turbulent flow (k-ε) Euler-Euler multiphase (Microcarrier)	PIV measurements	Ansys Fluent	Adipose stem cells (ASC) tolerated maximum shear stresses of 0.2 Pa. Characterized N_{S90}, N_{S1u}, and N_{S1} for Hillex and Pronectin-F microcarriers.
Berry et al., 2016	rpm = 60 Vol = 125 ml	N/A	Turbulent flow (SST) 3 LES approaches Euler-Lagrange multiphase (Microcarrier)	PIV measurements	Ansys CFX	LES calculated velocity fluctuations more accurately than URANS. Stress experienced by microcarriers was highest during impeller start-up (0.05 Pa). Minimum Kolmogorov length remains constant at ~60 µm.
Julaey et al., 2016	rpm = 30, 60, 90, 100, 120, 150 Vol = 3 L	Constant water ρ and μ	Turbulent flow (k-ε) Euler-Euler multiphase	Literature	COMSOL	60 rpm produced the best particle distribution. Average shear stress generated by 30 rpm was 0.9 mPa, by 60 rpm was 0.21 mPa, and by 90 rpm was 0.37 mPa.
Borys et al., 2018	rpm = 40, 60, 80, 100, 120, 140 Vol = 10 and 100 ml	N/A	Turbulent flow (k-ε)	N/A	COMSOL	When volume energy dissipation rate and shear stress were kept constant, aggregate sizes stayed constant during scale up.
Delafosse et al., 2018	rpm = 50, 100 Vol = 1.12 L	N/A	"Mixture" Turbulent flow (k-ε) Huilin-Gidaspow drag Euler-Euler multiphase (Microcarrier)	Light attenuation for solid phase distribution	Ansys Fluent	Solid distribution at the bottom was underestimated when rpm < N_{JS} and overestimated when rpm > N_{JS}

Table 1.1. Continued

Jossen et al., 2018	Vol = 125 and 500 ml rpm_125 = 25, 49, 60, 120 rpm_500 = 20, 41, 52, 100	Constant water ρ and μ	Euler-Euler multiphase (Microcarrier) Euler-Lagrange multiphase (Microcarrier)	PIV measurements	Ansys Fluent	Suspension criteria depend on geometrical dimensions. The same N_{S1} values will not create the same particle dispersion in larger bioreactors.
Wave/Rocking Bioreactor (WRB)						
Eibl et al., 2009	Bag Vol = 2, 20, 100, 200 L Fill Level = 40 and 50% Rocking Angle = 5.1, 6, 8, 10° Rocking Freq = 6, 15, 18, 20, 25 rpm	Newtonian	Volume of Fluid (VOF)	N/A	Ansys Fluent	Mass and energy transfer depends on wave formation and propagation. Residence and mixing times are comparable to an ideally mixed stirred tank. Mixing time for a cellbag of 2L ranged between 9-264 s, and for a 200L one from 65 - 874.
Oncul et al., 2010	Bag Vol = 2 and 20 L Fill Level = 50% Rocking Angle = 7° Rocking Freq = 15 rpm	Constant distilled water ρ and μ	Volume of Fluid (VOF)	Measured level of the liquid surface Estimation of velocity and shear stress w/ hot-film probe	Ansys Fluent	Maximum velocity was higher for the larger bag at the same rocking speed and angle. The maximum shear stress was 0.01 Pa – much lower than a stirred tank.
Zhan et al., 2019	Bag Vol = 10 L Fill Level = 50% Rocking Angle = 4, 5.5, 7° Rocking Freq = 15, 22, 30 rpm	Constant water ρ and μ	Volume of Fluid (VOF)	Oncul 2010	Ansys Fluent	Mixing and shear stress increased with increasing rocking angle. The lowest rocking speed studied generated the highest stress (0.05 – 0.06 Pa), velocity, and mixing. kLa values remained around 6 h^{-1} regardless of rocking angle.
Svay et al., 2020	Bag Vol = 2 and 20 L Fill Level = 50% Rocking Angle = 10° Rocking Freq = 20 rpm	Constant water ρ and μ	Volume of Fluid (VOF) Higbie's penetration model (Mass transfer coefficient)	Calculated mass transfer coefficient (K_La) from dissolved O2 measurements	Ansys CFX	Mixing time is close to 18 s. kLa values range from 10-100 h^{-1}.

Table 1.1. Continued

Reference	Bioreactor parameters	Media properties	Physics/Gov. Equations	Validation of CFD Results	Modeling software	Study Findings
Hollow Fiber Bioreactor (HFB)						
Mohebbi – Kalhori et al. 2012	membrane porosity(γ) = 0.2 fiber length (L) = 5 cm inner membrane radius = 0.15 mm perfusion rate (Q) = 17 ml/min	Constant water ρ and μ	Laminar flow Double Porous media Nutrient diffusion and consumption (Fick's Law) Glucose-limited cell growth kinetics	Literature data for oxygen concentration at the outlet	Ansys Fluent	Membrane thickness, inner fiber radius, inter-fiber spacing, and fiber length significantly affect cell volume fraction. The optimum fiber inner radius for high-density cell growth is 300-400 um. Fiber length is limited by the O_2 concentration and diffusion
Khademi et al., 2014	membrane porosity(γ) = 0.8 fiber length (L) = 4 cm inner membrane radius = 0.5 mm inlet velocity = 7.45E-3 m/s	Constant water ρ and μ	Laminar flow Porous media (NS-Brinkman) Nutrient diffusion and consumption (Fick's Law)	N/A	N/A 3D FEM	Increasing bioreactor length created a more drastic nutrient gradient. O_2 consumption was much faster than glucose. Thinner lumen walls increased mass diffusion but lost mechanical strength.
Menshutina et al. 2020	membrane porosity(γ) = 0.7 fiber length (L) = 11 cm inner membrane radius = 0.35 mm perfusion rate (Q) = 66.67, 133.3, 200 ml/min	Constant water ρ and μ	Hagen-Poiseuille and Darcy (permeate flow) Cell growth kinetics (Verhulst)	N/A	Ansys Fluent	Daily increases in medium flow rate were recommended for a more optimal media expenditure while providing enough nutrients. Counterflow for medium supply is not recommended as metabolites were not properly removed from the system.

Table 1.1. Continued

Reference	Bioreactor parameters	Media properties	Physics/Gov. Equations	Validation of CFD Results	Modeling software	Study Findings
Fluidized Bed (FBB)						
Huang et al., 2018 FBB	diameter = 0.1 m height = 0.2 m flow rate = 0.2, 0.5, 1.0, 1.5, 2.0, 2.5 cm/s particle diameter = 3, 4, 5 mm particle ρ = 1025, 1100, 1200 kg/m^3	Constant water ρ and μ	Euler-Lagrange multiphase (Glass Beads) Navier-Stokes fluid equations	Literature data for axial particle velocity	Ansys Fluent	Shear stress for a 3mm diameter, 1025 kg/m^3 particle was around 0.5 Pa. Larger and heavier particles experience shear stresses up to 1 Pa. Adopting a high-density material allowed the reactor to operate at higher flow rates before shear stress distribution became heterogeneous. Bed reached a steady state after 10 s at a flow of 0.005 m/s.
Mendonca et al. 2020 FBB	diameter = 3.5 cm height = 21 cm flow rate = 12 and 25 ml/min	Constant water ρ and μ	Navier-Stokes fluid equations Porous media Alginate encapsulation	Visual and calculated values for bed fluidization	SolidWorks 2018	Shear stress remained below 0.23 Pa. The validated design was used to build a multi-unit setup that had a yield comparable to a clinical scale FBB.
Ding et al. 2022 FBB	diameter = 0.4 m height = 0.8 m particle diameter = 360 um particle ρ = 2500 kg/m^3	Constant water ρ and μ	Euler-Euler multiphase (Bubbles) Gidaspow drag Turbulent flow (k-ε)	Literature data for bubbles volume fraction	Ansys Fluent	The gas bubble pattern can only be reproduced using Johnson and Jackson's frictional model in a laminar regime. Frictional models studied could not predict stresses and dilute/dense particle regions.

Table 1.1. Continued

Reference	Bioreactor parameters	Media properties	Physics/Gov. Equations	Validation of CFD Results	Modeling software	Study Findings
Airlift Bioreactor (ALB)						
Wadaugsorn et al., 2016 ALB	Height = 1.08 – 2.26 m Diameter = 0.28 – 0.57 m	Constant water ρ and μ	Euler-Euler multiphase (bubbles) Turbulent flow (k-ε)	N/A	Ansys Fluent	Liquid mixing times range from 18.4 – 24.5 s. The circulation time is minimized where the space of the riser and downcomer are equal. Larger reactors will have less wall effects, thus better dispersion.
Li et al., 2020 ALB	Height = 10.5 m Diameter = 5 m	Constant water ρ and μ	Euler-Euler multiphase (bubbles) Tomiyama drag law Turbulent flow (realizable k-ε)	Wadaugsorn et al., 2016	Ansys Fluent	Average energy dissipation rate was 0.049 m^2/s^2, and kLa was 36 h^{-1}. Mixing time was 103.4 s with single injection point, however, reactor has capacity for multiple injection points.
Rotary Wall (RWV) and High-Aspect Ratio Vessels (HARV)						
Cinbiz et al., 2010 RWV	rpm = 33, 35, 37, 38 Length = 14.5 cm Outer radius = 3.4 cm Inner radius = 0.75 cm Flow rate = 2.25 ml/min	ρ = 1020 kg/m^3 μ = 0.97 mPa*s	Laminar flow	N/A	Ansys Fluent	Upper surfaces of the scaffolds experienced higher shear stress (9-12 mPa) than lower surfaces (7 - 11 mPa)
Ghasemian et al., 2020 RWV	rpm = 40, 60, 80, 100 Length = 9.4 cm Outer radius = 3.75 cm Inner radius = 3 cm	N/A	Laminar flow	N/A	ANSYS CFX	The standard deviation in Shear stress generated in RWB is about 53% smaller than in STB.
Consolo et al. 2012 HARV	rpm = 10, 15, 20, 25, 30	Constant water ρ and μ	Euler-Euler multiphase (Alginate Encapsulated Cells) Laminar flow Michaelis Menten for O2 consumption	N/A	Ansys Fluent	30 rpm was inadequate for encapsulated ESC because of frequent collisions and heterogeneous distribution. Rotational speeds < 20 rpm led to inadequate mixing.

Table 1.1. Continued

Teo et al., 2014 RWV & HARV	rpm = 10, 12.5	N/A	Laminar flow Nutrient diffusion Stationary Alginate Encapsulated Cells	N/A	Ansys Fluent	HARV and RWB made nutrient transport into encapsulated cells than static culture faster.
Chao and Das, 2015 HARV	rpm = 10 diameter = 7.5 cm	Constant water ρ and μ	Euler-Euler multiphase (Alginate Encapsulated Cells) Nutrient diffusion Glucose-limited cell growth kinetics	Literature data for cell volume fraction	COMSOL	Cells accumulated in the middle of the bioreactor Nutrient concentration was uniform, with a slight decrease in the middle possibly caused by the high cell concentration.

2. CHAPTER II.

AN ARTIFICIAL NEURAL NETWORK-BASED MACHINE LEARNING APPROACH TO CORRECT COARSE-MESH-INDUCED ERROR IN COMPUTATIONAL FLUID DYNAMICS MODELING OF CELL CULTURE BIOREACTORS

A version of this chapter was originally published by Fernando José Cantarero Rivera, Ran Yang, Haochen Li, Hairong Qi, and Jiajia Chen:

Cantarero-Rivera FJ, Yang R, Li H, et al (2024) An artificial neural network-based machine learning approach to correct coarse-mesh-induced error in computational fluid dynamics modeling of cell culture bioreactor. Food and Bioproducts Processing 143:128–142. https://doi.org/10.1016/j.fbp.2023.11.004

As the first author of this research article, I was the main contributor to Conceptualization, Methodology, Data curation, Investigation, Software, Visualization, and Writing of the manuscript. Dr. Jiajia Chen, as the major professor and corresponding author, contributed to Conceptualization, Investigation, Supervision, Project administration, Funding acquisition, Writing - Reviewing and Editing of the manuscript. The co-authors contributed with technical machine learning support, and Reviewing and Editing of the manuscript.

Abstract

Computational Fluid Dynamics (CFD) is a valuable tool for studying fluid environments within cell culture bioreactors and optimizing processing parameters, but it can be computationally expensive. This study developed an artificial neural network (ANN)-based machine learning model to predict and correct the coarse-mesh-induced errors in CFD modeling of a spinner flask bioreactor. A baseline ANN model was trained to predict the velocity error function between the coarse and optimized reference mesh results at one rotational speed (90 rpm), demonstrating that the ANN-based approach could correct the coarse-mesh velocity with RMSE values of nodal velocities improved by an average of ~20% at different rotational speeds. The effect of ANN structure, input data normalization, and training dataset combinations on prediction performance was evaluated. More neurons and hidden layers generated better results but required more computational time for training. The model's generalization capabilities were further evaluated in case studies of correcting velocity and Kolmogorov length at different fluid viscosity and bioreactor impeller geometry conditions. Results suggested that the ANN model had better generalization in correcting Kolmogorov length than velocity. This research provides insights into using a machine learning approach to enhance CFD modeling in bioreactor applications, contributing to advancing tissue engineering processes.

Keywords: Machine learning, ANN, CFD. Coarse mesh error, Spinner flask, Cell culture.

1 Introduction

Animal cell culture in bioreactors is an essential technique for biopharmaceutical and tissue engineering (Pörtner 2015) with recent applications for cultivated meat production (Hanga et al. 2021). Cell culture in bioreactors involves the growth and proliferation of animal cells in a controlled environment outside their natural habitat, allowing researchers to study cell behavior, characteristics, and functionality. While traditional animal cell culture methods involve flasks, dishes, or roller bottles, bioreactors (e.g., stirred tank, rocking bed, etc.) have become a powerful and efficient approach in recent years to increase cell culture efficiency. Bioreactors provide a controlled and optimal environment for the growth of animal cells by simulating the conditions found within living organisms. These specialized vessels integrate parameters such as temperature, pH, dissolved oxygen, and nutrient supply to create the ideal environment for cell growth, proliferation, and production of desired products. However, bioreactor scale-up is one of the main issues faced by cultivated meat industry. Humbird (2020) developed a techno-economic analysis of why scaling up cultivated meat is so complicated, including the slower growth rate of animal cells, the increased shear sensitivity of animal cells, and the high cost of culture media compared to bacterial cell cultures. Animal cells’ sensitivity to mechanical stress and low growth rate have led to several bioreactors designed to address specific issues such as excessive shear stress and insufficient nutrient mixing (Taya and Kino-oka 2011; Valdiani et al. 2019). Since the hydrodynamic environment surrounding the cells plays such a significant role, it is important to be able to characterize it accurately to properly design the bioprocesses and ensure adequate proliferation and differentiation and ultimately obtain consistent final product yields.

Computational Fluid Dynamics (CFD) is a very useful tool for understanding the fluid environment within the bioreactors and allows for better control of processing parameters. It has been extensively used to simulate the various bioreactor systems and help with their design and scale-up (Cantarero Rivera and Chen 2022). CFD simulations of lab-scale spinner flasks have been used to characterize the stress experienced by cells on microcarriers and validated by particle image velocimetry (PIV) (Kaiser et al. 2013; Berry et al. 2016). Similar models have been developed to help scale up bioreactor processes from spinner flasks up to large, industrial-scale bioreactors with working volumes up to 10 m^3 (Scully et al. 2020) and 90 m^3 (Nadal-Rey et al. 2022). The most significant advantage of using tools such as CFD is that the experimental time and cost are reduced significantly by simulating multiple scenarios without physically doing all the experiments. This cost reduction is especially helpful for system design and scale-up, for example, when designing the impeller for a stirred tank without having to build all of the options and testing them (Bliatsiou et al. 2019) or when upscaling production to industrial levels since it is not feasible to run multiple experiments at such large scales (Zhang et al. 2021). However, CFD models of bioreactors can quickly become computationally expensive, especially as the processes are scaled-up and more parameters are included. To accurately model mixing performance in bioreactors, the physical geometry must be discretized into small elements by creating a fine mesh. In general, employing finer grids can enhance the precision of the outcomes. However, it’s important to consider the balance between refining the grid, the computational expense, and the duration of the simulation. A grid independence study is used to ascertain the optimal grid resolution for sufficient modeling accuracy and decent computational efficiency.

Machine learning (ML) algorithms have been used to improve CFD models’ accuracy and computational efficiency. ML algorithms can increase the speed of high-accuracy simulations, develop turbulence models with different levels of fidelity, and produce reduced-order models beyond what can be achieved with classical approaches (Vinuesa and Brunton 2022). ML algorithms may be applied in different steps during a CFD-based study. Kochkov et al. (2021), implemented a convolutional neural network (CNN) to expedite Direct Numerical Simulations (DNS) of the Navier-Stokes equations and Large Eddy Simulations (LES) by using the CNN as a solver that fits the observed CFD solutions to the equations they solve. This approach maintained the accuracy and generalization of the simulations while achieving an acceleration factor of up to 40 times. Raissi and Karniadakis (2018) proposed a probabilistic ML approach to learn the physics and solve the Navier-Stokes equations by using Gaussian processes which infer parameters of the corresponding partial differential equations (PDEs) from limited and possibly noisy CFD models. Wu et al. (2022) used a neural network to create an adaptive mesh that refines areas with high gradients and decreases number of nodes in low-gradient regions. This approach significantly improves the accuracy of local flow features. Others have proposed using ML approaches to improve solvers for Navier-Stokes (Ranade et al. 2021) and pressure Poisson (Chen et al. 2022) equations. Using ML solvers could achieve good accuracy, better stability, and faster convergence as compared to typical partial differential equations solvers.

ML approaches can also be used as post-processing to analyze data patterns in results to verify the accuracy of new models (Wang and Wang 2021). One of the data-driven ML approaches used to reduce computational time and cost is the coarse-grid CFD correction. Pirnia et al. (2019) used coarse-grid CFD data as inputs for an artificial neural network (ANN) to predict the drag force on smaller particles in granular materials. Hanna et al. (2020) proposed a method to calculate the local errors due to a coarse mesh and train ANN and random forest (RF) models to predict high-accuracy results based on a new CFD model for a basic lid-driven cavity. Different ML algorithms have been evaluated in multiple studies and found controversial results. Kiener et al., (2023) used an ANN, RF, and Graph neural network to improve the accuracy of coarse mesh velocity components, pressure, and density results from a 2D airfoil and a 3D LANN wing. The results showed that the best correction performance was obtained using the GNN and that the ANN worked better than a RF when the models were trained with 60 simulations and tested on 29 others. On the other hand, results obtained by Hanna et al. (2020) suggested that the RF model had better performance than the ANN. Overall, these studies showed that using ANN-based (and others) ML models to predict high-accuracy CFD results is a promising method to increase computational efficiency. Inspired by these studies, a similar approach can be applied to extend these simulations of simple flow applications to more complicated applications of simulating fluid flow in cell culture bioreactors.

In the ANN model, the model structure (Pirnia et al. 2019), input data quality (Bandi et al. 2023), and training dataset (Hanna et al. 2020) are important parameters that influence the ML model's accuracy. The model architecture refers to the hyperparameters (neurons, hidden layers, activation functions, learning rates, etc.) that can be fine-tuned to improve the prediction performance of the ANN model. However, there is no best way to optimize these parameters, so the typical approach is trial-and-error until the model's results satisfy our expectations. Input data quality refers to whether the inputs have been normalized or not. Although the activation functions help normalize the inputs in different ways depending on the function used, normalizing the input data before feeding it to the model is generally a good practice to save computational time and improve prediction performance (Liu et al. 2023). Finally, the training dataset used often influences the prediction results. The general understanding is that as more data is fed to the ANN model, the better it will be at predicting, especially when the prediction falls within the range of the datasets used for training. However, the model's ability to extrapolate and predict outside of the training range should be evaluated to understand the range of applications in which the model can be used.

Considering all the factors mentioned above, the objectives of this study are to:

(1) develop and validate a CFD model to simulate the mixing performance of fluid velocity in a spinner flask for cell culture;

(2) develop a baseline ANN-based ML model to predict and correct the coarse-mesh-induced errors of velocity in CFD modeling of cell culture bioreactor with various mixing speeds;

(3) evaluate the effect of the ANN architecture (number of neurons, normalization of input dataset, and training datasets) on the ML models' accuracy in correcting coarse-mesh-induced errors of velocity in CFD modeling;

(4) evaluate the generalization of the trained ANN-based ML model in case studies of correcting velocity and Kolmogorov length at additional conditions of different fluid viscosity and impeller geometry.

2 Materials and methods

2.1 Problem description

The overall concept of this study is to use an ANN-based ML learning model using CFD modeling results from different mesh sizes as training datasets to predict and correct the coarse-mesh-induced errors. ANN was chosen as the choice of ML algorithm due to the promising results reported by Kiener et al. (2023) and Pirnia et al. (2019). The CFD models were solved with both a coarse mesh and a fine mesh that was optimized through a mesh independence study. The results of the CFD model with optimized mesh were considered accurate and reference results, while the other CFD models with a coarser mesh would have coarse-mesh-induced errors in the simulated results (e.g., velocity profiles). The predicted error function can then be used to correct the coarse-mesh modeling results and compared against the reference CFD results for accuracy evaluation. **Figure 2.1** shows the three steps of the ANN-based machine learning modeling approach for error prediction and correction: CFD to generate the training dataset for ML, ML training to predict coarse-mesh-induced error, and CFD correction with ML.

The mixing performance (velocity profiles) of a Corning®, Series 4500-125 spinner flask (Corning, NY) with 100 mL working volume at impeller speeds of 30, 60, 90, 120, and 150 rpm was evaluated by CFD modeling and ML-corrected CFD modeling in this study. These rotational speeds were selected to represent conditions similar to those commonly used for animal cell culture experiments (Jeske et al., 2021; Van Beylen et al., 2021; Yang et al., 2019). A baseline ML model with a default ANN architecture was developed using the mixing performance of 90 rpm to predict and correct the coarse-mesh modeling results of velocity profiles at all five rotational speeds (30, 60, 90, 120, and 150 rpm). The effect of ANN structure (i.e., number of neurons, normalization of training datasets, and training dataset conditions) on the ML model performance for error correction was comprehensively evaluated with details described in the following sections.

2.2 CFD modeling of mixing performance in the spinner flask

2.2.1 Geometry

The geometry of the spinner flask (Corning®, Series 4500-125, Corning, NY) was created in COMSOL Multiphysics® 6.1 (COMSOL Inc., Burlington, MA) following the flask and impeller dimensions, as shown in **Figure 2.2**. The impeller itself is composed of a magnetic stirring bar and a pair of paddles held together by a cylindrical housing. The working volume of 100 mL was used following our other ongoing cell culture experiments.

2.2.2 Governing equations and boundary conditions

The simulation used the Reynolds averaged Navier-Stokes (RANS) κ-ε turbulence model. This turbulence model is widely used for industrial applications because of its low memory requirements (Corsini et al. 2013). The Reynolds-averaged approach separates dependent variables into two components, a time-averaged and a fluctuating component represented as:

$$\boldsymbol{u_i} = \boldsymbol{\overline{u}_i} + \boldsymbol{u'_i} \tag{2.1}$$

Assuming steady-state, that the fluid flow is incompressible Newtonian, and incorporating the two components from equation 1, the RANS equation is expressed as:

$$\rho \boldsymbol{u} \cdot \nabla \boldsymbol{u} = -P\nabla + (\mu + \mu_t)\nabla^2 \boldsymbol{u} + \rho g \tag{2.2}$$

$$\rho \nabla \cdot \boldsymbol{u} = 0 \tag{2.3}$$

where ρ is the density, $\boldsymbol{u}$ is the Reynold's-averaged velocity field, P is the pressure, μ is the dynamic viscosity, and g is the gravity constant. The κ-ε turbulence model introduces two additional transport equations, one for k, the turbulent kinetic energy, expressed as:

$$\rho\boldsymbol{u}\cdot\nabla k = \nabla\cdot\left(\left(\mu+\frac{\mu_t}{\sigma_k}\right)\nabla k\right)+P_k-\rho\varepsilon \qquad \textbf{(2.4)}$$

and one for ε, the turbulent dissipation rate, expressed as:

$$\rho\boldsymbol{u}\cdot\nabla\varepsilon = \nabla\cdot\left(\left(\mu+\frac{\mu_t}{\sigma_\varepsilon}\right)\nabla\varepsilon\right)+C_{\varepsilon1}\frac{\varepsilon}{k}P_k-C_{\varepsilon2}\rho\frac{\varepsilon^2}{k} \qquad \textbf{(2.5)}$$

where σ_k and σ_ε are the turbulent Prandtl numbers for k and ε, respectively, and P_k is the production term expressed as:

$$P_k=\mu_t\left(\nabla\boldsymbol{u}:(\nabla\boldsymbol{u}+(\nabla\boldsymbol{u})^T)-\frac{2}{3}(\nabla\cdot\boldsymbol{u})^{\boldsymbol{2}}\right)-\frac{2}{3}\rho k\nabla\cdot\boldsymbol{u} \qquad \textbf{(2.6)}$$

where μ_T is the turbulent viscosity modeled as:

$$\mu_t=\rho C_\mu\frac{k^2}{\varepsilon} \qquad \textbf{(2.7)}$$

This model uses five turbulence constants $C_\mu = 0.09$, $C_{\varepsilon1} = 1.44$, $C_{\varepsilon2} = 1.92$, $\sigma_k = 1$, and $\sigma_\varepsilon = 1.3$. These were determined from experimental data in simple flows (Launder and Spalding 1974; Wilcox 2006).

An initial no-slip wall condition, where the fluid velocity relative to the wall velocity is zero, was defined at the bioreactors' walls and is represented by:

$$\boldsymbol{u}=0 \qquad \textbf{(2.8)}$$

The liquid was set to have a constant viscosity of 1 mPa·s and a density of 1000 kg/m^3.

The geometry was separated into two domains: a stationary/outer domain and a rotating/inner domain around the impeller to prescribe constant revolutions per time for the impeller. The boundary between the two domains was defined as a continuity boundary that transfers momentum from the rotating domain to the stationary domain. A two-step study called "frozen rotor with stationary free surface" was used to solve the model. The first step of the study, the frozen rotor, computed the velocity, pressure, and turbulence in rotating machinery, assuming the flow is fully developed. In this step, the rotating parts were kept stationary, and rotation effects were accounted for by including centrifugal and Coriolis forces. The second step, the stationary free surface, solved the deformation of the top boundary layer, the liquid-gas interface. For this second step, a stationary free surface boundary condition was defined at the top of the geometry to identify the liquid/gas interface and define an external pressure of 0 Pa.

2.2.3 Meshing scheme

A tetrahedral mesh with a boundary layer of brick elements at the bioreactors' wall was created for the geometry following a linear discretization for fluid velocity and pressure fields. Pyramid and prism elements were used to transition from the boundary elements to the tetrahedral elements. This mixed mesh approach is preferred over meshing with a single type of element as it reduces degrees of freedom and computational complexity (Rousseau et al. 2013). A mesh-independence study was performed to determine the optimal mesh size for accurate modeling results and acceptable computational time for a CFD model with a rotational speed of 30, 60, and 150 rpm for the impeller (**Figure 2.3**). The 30 and 150 rpm represented the speeds at two ends of the evaluation, and 60 rpm was used in the experimental validation. The volumetric average velocity magnitude and turbulent dissipation rate (TDR) were selected as indicators since this study focuses on the fluid profile inside the bioreactor (Borys et al. 2019; Kreitmayer et al. 2022). The percent change between meshes is always < 1% for the velocity magnitude at all mixing speeds meaning it is reasonably stable. The percent change in TDR is < 5% when the mesh reaches ~1 million elements for all rotational speeds. Considering this, the mesh with 1.03 million elements was considered the optimized mesh. The mesh size for the rotating domain ranged from 0.0883 to 2.712 mm, and for the stationary domain, from 0.1676 to 2.908 mm in the optimized mesh (**Figure 2.4**a). The modeling results using this mesh were considered accurate and reference results for later ML model training and corrected modeling results comparison.

2.2.4 Simulation strategy

The CFD model was simulated by solving the governing equations using a segregated iterative Generalized Minimal RESidual (GMRES) solver for velocity and turbulence variables. The numerical convergence was consistent in all simulations across the mixing speed range as the errors reached values of $2 – 3 \times 10^{-4}$. The simulations were performed using a workstation with 2 Intel® Xeon® Gold 6234 CPU at 3.30 GHz, 3301 MHz, 8 cores, 16 logical processors, and 100 GB of installed physical memory (RAM).

2.2.5 CFD model validation

The COMSOL κ-ε turbulence model has been widely used for suspension bioreactors (Borys et al. 2019; Freiberger et al. 2022). The modeling results of velocity profiles were validated with the experimental velocity profiles of a Corning® series 4500-125 spinner flask collected using the PIV at the same condition by Berry et al. (2016). Note that the volume used in the PIV experimental results was 140 mL, while a working volume of 100 mL was used in the ANN-based ML model training and correction to represent our cell culture experiments.

2.3 Baseline ANN model for predicting and correcting the coarse-mesh-induced error

The framework for using the ANN model to predict and correct the coarse mesh-induced errors of CFD modeling results is shown in **Figure 2.5**, with Prediction and Correction components. The Prediction component used the training datasets of the coarse- and optimized reference-mesh CFD modeling results at one mixing condition (e.g., 90 rpm) to predict the flow-dependent coarse-mesh-induced error functions. The predicted error functions can then be used in the Correction component to correct the coarse-mesh-induced errors at other mixing conditions (e.g., 30, 60, 90, 120, and 150 rpm in this study).

2.3.1 Prediction of coarse-mesh-induced error using ANN

In the Prediction component, the baseline ANN model was trained with CFD modeling results obtained at 90 rpm. The training dataset is obtained by simulating this flow condition with the optimized reference mesh (~1 million elements) (**Figure 2.4**a) and again with a coarse mesh (~44,500 elements) (**Figure 2.4**b). Before the training process, the coarse-mesh CFD modeling results were first mapped into a higher resolution using the coordinates of the optimized reference mesh in COMSOL Multiphysics. This mapping step to a higher resolution differed from (Hanna et al. 2020), where the fine mesh results were mapped down to the coarse mesh. Both mapping approaches introduced mapping errors, either before the training or after the training. The use of mapping from coarse to fine approach in this study has potential benefit that the prior mapped error can be learned and corrected in the ML training process. In addition, the mapping-up approach used in this study could obtain corrected CFD modeling results in a higher resolution, which is important for studying the mixing performance in cell culture bioreactors.

A total of 37 local (nodal) variables, including the cell-Reynolds number and the cell-size normalized first and second derivatives of the fluid velocity components on x, y, and z directions from the coarse and reference mesh simulations, were used as the features or inputs (predictors) for the ANN model, as shown in **Figure 2.6**. The first and second derivatives of the fluid velocities were normalized by multiplying the cell size and the square of the cell size, respectively, following a Taylor expansion concept, as explained in Hanna et al. (2020). The error between the reference and coarse-mesh velocity profiles was used as the output (response). During training, the ANN fits a regression between the inputs and outputs. The ANN model with default structure in MATLAB, one hidden layer with 20 neurons and a sigmoid activation function, was used for the baseline ANN model (**Figure 2.6**). The backpropagation Levenberg-Marquardt algorithm was used to train the ANN (Levenberg 1944; Marquardt 1963). The input dataset was randomly separated into three groups: 70% was used for training, 15% to validate that the network is generalizing and stop training before overfitting, and 15% to test network generalization. The ANN algorithm was implemented in MATLAB with the Deep Learning toolbox.

During the ANN model training process, the training mean square error (MSE) and regression (R) were used as indicators of training performance. In a general ANN training process, the ANN network weights and biases are re-adjusted in each iteration to reduce the MSE. Training stops when the validation error increases consecutively for six iterations. Non-zero MSE may indicate that more data is needed to train the ANN to capture the relation between the output and the inputs or that we need more flow features, or inputs, to characterize the flow. MSE values may also be reduced if the number of neurons increases (Hanna et al. 2020). The ANN also fits a nonlinear regression between the predictions (output) and the responses (target) for the training, validation, and test sets. A regression value (R) is calculated for each of these regressions. Training performance is better when this value increases, especially when the test R increases (Hanna et al. 2020; Seb Rengma et al. 2023).

2.3.2 Correction of coarse-mesh-induced error using ANN

After training, the ANN model can be used to predict and correct the errors at other mixing conditions with different flow behaviors. The trained ANN model can be fed with a new set of 37 coarse-mesh inputs to predict flow-dependent errors at new mixing conditions. These predicted errors are then combined with the coarse-mesh velocity profiles to correct the errors. This study predicted and corrected mixing performance (velocity profiles) at 30, 60, 90, 120, and 150 rpm using the trained baseline ANN model at 90 rpm.

2.4 Performance evaluation of the ANN model for coarse mesh-induced error correction

The prediction and correction accuracy of the ANN model was evaluated by the root mean square error (RMSE) of nodal velocity profiles at x, y, and z components. Two RMSE values were calculated: one RMSE value was calculated between coarse-mesh and reference model results (Equation (2.9), and the other RMSE value was calculated between the corrected and reference model results (Equation(2.10).

$$RMSE_{coarse} = \sqrt{\frac{1}{n}\sum_{i=1}^{n}|Coarse_i - Reference_i|^2} \quad \textbf{(2.9)}$$

$$RMSE_{corrected} = \sqrt{\frac{1}{n}\sum_{i=1}^{n}|Corrected_i - Reference_i|^2} \quad \textbf{(2.10)}$$

where *n* is the number of meshing nodes of the reference mesh, *Coarse*$_i$, *Corrected*$_i$*, and Reference*$_i$ are the nodal velocities (x, y, or z) from mapped coarse mesh, corrected, and optimized reference mesh modeling results.

The percentage change of the RMSE value change from the coarse-mesh model to the corrected model was calculated as follows:

$$\Delta RMSE\ \% = \frac{RMSE_{corrected} - RMSE_{coarse}}{RMSE_{coarse}} \times 100 \quad \textbf{(2.11)}$$

Lower RMSE values indicate that the model results match better with the reference results. A negative number in the percentage change indicates an improvement in velocity accuracy.

2.5 Effect of ANN model structure on corrected CFD model accuracy

2.5.1 Effect of number of neurons and hidden layers

It is well-known that the hyperparameters (e.g., number of neurons, hidden layers, learning rate, activation function, among others) play a significant role in the network's training and prediction performance. Pirnia et al. (2019) suggest that these hyperparameters must be optimized, but no rule exists for choosing them. Optimizing the hyperparameters is typically a trial-and-error process that depends on the user's optimization criteria, such as minimizing the training MSE or maximizing the training regression R. Le et al., (2023) used the trial-and-error approach to test 50, 100, 150, and 200 neurons per hidden layer and one, two, or three hidden layers until their selection criterion (mean test error) was minimized. Their finalized structure consisted of three hidden layers with 50 neurons per layer. Other approaches such as the Bayesian optimization and Genetic Algorithms can be used to help with hyperparameter optimization (Yang and Shami 2020). This study used a grid search approach where various levels of each hyperparameter were tested within an arbitrary range to find one that minimizes the training MSE and maximizes error prediction and correction accuracy. The number of neurons tested were 5, 10, 20, 30, 50, and 100 and 1 – 5 hidden layers with 20 neurons per layer and with 100 neurons evenly distributed. All hyperparameters' values were tested on the 90-rpm coarse mesh dataset.

2.5.2 Effect of normalization of the training data input

The performance of ANN models depends on the quality of the data used as inputs. The model could be biased towards inputs with more variation, and therefore the model's predictive ability might be hindered (Bandi et al. 2023). Exploratory data analysis of the ANN inputs showed that although the velocity derivatives were already normalized by multiplying with their respective cell sizes, there was still a considerable difference among the ranges of each input feature (**Figure 2.7**). Typical approaches used to tackle this issue are to normalize the datasets by scaling them to specific ranges, such as from 0 to 1 or from -1 to 1, to calculate the z-scores and ensure the variables have a mean of 0 and a standard deviation of 1, or to calculate the norm-2 Euclidean distances (GökhanAksu 2019). All these normalization techniques were tested to determine their impact on the prediction results. The 37 input variables were normalized in MATLAB using the corresponding functions.

2.5.3 Effect of training datasets of mixing conditions

The baseline ANN model used the CFD modeling results for a mixing speed of 90 rpm for training and corrected the coarse-mesh CFD results of all five impeller rotational speeds: 30, 60, 90, 120, and 150 rpm. Each dataset consists of the cell-Reynold's number and the first and second derivatives of the velocity components in all directions. Since the mixing speed varied in a wide range (e.g., 30 to 150 rpm), the limited training dataset at 90 rpm may not be enough for good training. Thus, this study further evaluated the effect of different combinations of datasets from different mixing speeds on the ANN model accuracy for error prediction and correction. In addition to the training dataset of 90 rpm, all other single mixing speeds (30, 60, 120, and 150 rpm) and varied combinations (30 & 60 rpm, 120 & 150 rpm, 30 & 150 rpm, 60 & 120 rpm, 30, 90, & 150 rpm) were used as training datasets. These different training datasets were selected considering their varied mixing performances that either cover narrow or wide ranges for testing the ANN model's capability of interpolation and extrapolation. The ANN model performance on error correction was evaluated on all five impeller speeds for each ML model with different mixing conditions of training datasets.

2.6 Generalization of the ANN-model in other case studies

The developed ANN-based ML model/approach was further evaluated on its generalization in other case studies of correcting velocity and the Kolmogorov length at other mixing conditions of different fluid properties and impeller geometry.

First, the developed baseline model/approach was re-trained to predict and correct the errors of Kolmogorov length scale using the baseline model. The Kolmogorov length scale (η) describes the smallest scale in the turbulent fluid and at this length, viscosity dominates, and the turbulence kinetic energy is dissipated into thermal energy. This parameter has important applications in bioreactor scale-up as turbulent eddies with η values smaller or similar in size to animal cells can cause damage and even induce the cell death (Croughan et al. 1987). The Kolmogorov length can be expressed as:

$$\eta = \left(\frac{v^3}{\varepsilon}\right)^{\frac{1}{4}} \tag{2.12}$$

where v is the kinematic viscosity of the fluid and ε is the turbulent energy dissipation rate.

Then, two additional case studies used the developed baseline 90 rpm ML models (velocity and Kolmogorov length) and applied in other mixing processes with different fluid viscosities and a different stirrer geometry to evaluate the generalization of the trained ML at one mixing condition. In the fluid viscosity case study, two other viscosities (0.5 and 2 mPa·s) were evaluated. In the different stirrer geometry case study, a simplified geometry was made using only the magnetic stirrer portion of the original impeller. This simple cylindrical bar has a length of 3.75 cm and a diameter of 0.8 cm, as seen in **Figure 2.2**b and **Figure 2.2**c. The height off the bottom to the center of the bar was kept the same as in the original geometry, 2 cm. The final simplified geometry is shown in **Figure 2.8** and is considered to be similar to impeller used for the disposable Corning ® spinner flask used by (Jossen et al. 2018). Note that both case studies did not develop new ML models but used the baseline ANN models for velocity or Kolmogorov length correction.

3 Results and discussion

3.1 CFD model validation

The CFD model of the spinner flask was validated against PIV flow patterns from Berry et al. (2016) at a mixing speed of 60 rpm using a volume of 140 mL in the Corning® series 4500-125 spinner flask (**Figure 2.9**). There was generally good agreement in the overall flow pattern between simulation and experiments. Two major vortices were observed around the stirrer in both the CFD simulation and experimental data with similar intensities and slightly different locations. The slight differences between simulation and experiment might be attributed to periodic deformations of the fluid surface and possible misalignment of experimental stirrer. These periodic fluctuations were not captured with the ensemble-average PIV results and the steady-state CFD simulation strategy. Berry et. al, (2016) also simulated the flow pattern using different transient CFD approaches (not shown) and reported slightly different vortex locations for all models and argued the boundary condition of the fluid surface could influence this as well.

The simulated results in this study were further quantitatively validated by comparing the simulated velocity component values horizontally and vertically relative to the center of the two major vortices (shown in **Figure 2.9**) against the experimental results and the computational models (Unsteady RANS and variations of LES) from Berry et. al, (2016). **Figure 2.10**(a) and (c) showed the vertical velocity along the horizontal line across the top and bottom vortexes, respectively; **Figure 2.10** (b) and (d) showed the horizontal-velocity along the vertical line (perpendicular to the plane in **Figure 2.9**) across the top and bottom vortexes, respectively. There was reasonable agreement between this study and the experimental values, however, values farther from the center of the vortices had larger differences. As mentioned previously, these differences can be attributed to differences in location and size of the vortices. For example, the lower vortex was closer to the impeller in this study than in the PIV ensemble-averaged results. Furthermore, the CFD model used the frozen rotor approach, which simplified the flow to a steady-state condition and the ensemble-averaged results from the PIV fail to capture the vortices’ random walk.

3.2 Coarse mesh correction results using baseline ANN model

The baseline model, using 20 neurons in a single hidden layer and 90 rpm dataset as training without specific normalization, was first used to predict and correct the coarse-mesh-induced error of the velocity components in x, y, and z direction for the same rotational speed of 90 rpm (**Figure 2.11**). The RMSE values for the coarse and corrected velocity components against the reference results obtained from the optimized reference mesh were calculated. The results showed that the trained baseline ANN model could properly predict the coarse mesh-induced error and improve the velocity components at x, y, and z directions with smaller corrected RMSE values (23.0% – 24.1% improvement). As seen from the scatter plot of the nodal velocity in Figure 11, the z-velocity spread to a wider range along the diagonal line, indicating a larger coarse-mesh-induced error in the z-direction velocity. Thus, in the following discussions, the prediction and correction accuracy of the ANN model was only reported for the z-velocity component. Note that the smaller coarse RMSE value in z-direction than that of x- and y-directions was attributed to the smaller z-velocity magnitudes.

The baseline model was then used to correct the z-velocity component for all five rotational speeds of 30, 60, 90, 120, and 150 rpm. Qualitative comparison using contour plots of the z-velocity profiles between coarse mesh, reference mesh, and corrected modeling results is shown in **Figure 2.12**. The results showed that the corrected z-velocity profiles were closer to the reference than the coarse mesh results for most mixing scenarios, especially for the regions close to the impeller. More specifically, the coarse mesh results underestimated the velocity below the impeller and overestimated it along the sides of the impeller. The trained ANN model corrected the underestimated and overestimated velocities in these regions. However, the corrected results were not as smooth as the originally simulated results. This is one limitation of the used ANN model where the correction was applied on each individual node without considering the gradients of adjacent nodal points. Other machine learning algorithms (e.g., convolutional neuron network - CNN) that use the volumetric modeling results of all nodes as a single datapoint in the training process could have smoother results. But CNN model needs a large amount of simulation results at different conditions as training dataset to train a robust model.

The improvement in the corrected results can be qualitatively and quantitatively observed from the scatterplots and RMSE values of the nodal z-velocity of the coarse mesh and corrected results against the reference results obtained from the optimized mesh, as shown in **Figure 2.13**. The narrower scatterplots and smaller corrected RMSE values of the corrected results indicated their better match with the reference results than the coarse mesh for most mixing conditions, except 30 rpm.

3.3 Effect of ANN architecture on model prediction and correction accuracy

3.3.1 Effect of number of neurons and hidden layers

The training performance of the ANN was measured by the mean square error (MSE) and the training regression R. It is generally accepted that more neurons and hidden layers lead to better training performance, however, overparameterization can lead to overfitting which negatively impacts the model's generalization capabilities. Training performance was evaluated in terms of minimizing MSE and maximizing training R. The prediction performance of the trained ANN models with a different number of neurons was measured using the RMSE values for the coarse mesh and corrected results and the percentage change of RMSE values. A lower prediction RMSE value indicates a better result.

As the number of neurons in the single hidden layer increased from 5 to 100, the training MSE decreased, and regression R increased as expected (**Table 2.1**). However, when the number of neurons was increased to 100, the training time increased significantly, which defeats the purpose of using this approach to reduce computational expense. The correction performance of the trained ANN models was improved as more neurons were included in the ANN model. This shows the direct relationship between the training and prediction performances.

Different numbers of hidden layers (1 – 5) were also tested. When using 20 neurons per layer, the best results for both training and prediction performance were obtained when using 5 hidden layers (**Table 2.2**). However, this approach also increased the number of neurons in total. To eliminate the impact of changing neurons and properly evaluate the impact of changing the number of hidden layers, 100 neurons were evenly distributed in 1 – 5 hidden layers. In this case, the best training and prediction performances were obtained when using 4 hidden layers with 25 neurons each (**Table 2.3**). However, increasing to 5 layers with 20 neurons each reduced training time considerably while still having comparable training and prediction performance.

3.3.2 Effect of input normalization

The correction performance of the ANN model with different normalization of inputs was measured with the RMSE, as shown in **Table 2.4**. None of the tested normalization techniques improved the correction performance compared to the baseline model result. The lack of improvement indicated that the input data required no further tweaking. The worst results were obtained when scaling the input data from -1 to 1, where the RMSE values increased for all rotational speeds. This is different from the results obtained by GökhanAksu, (2019) who found that the scaling method, also known as, min-max scaling yielded better results. Instead of individual scaling of the input data, other approaches such as online normalization (Chiley et al. 2019) and feature-wise normalization (Singh and Singh 2022) have been proposed to improve ANN performance.

As mentioned previously, the predictive ability of ANN models might be hindered depending on the quality of the data used as inputs as the model could be biased towards inputs with more variation (Bandi et al. 2023). Limited and imbalanced training samples often lead to the learning of highly similar parameters, resulting in model redundancy and compromising its generalization capacity. Diversified data improves the quality of training samples, enhancing informativeness and representativeness, thus, maximizing the information available for the model to learn, subsequently improving the model's fit to the data (Gong et al. 2019).

3.3.3 Effect of training datasets of mixing conditions

The effect of training datasets of mixing conditions on the ANN model performance was evaluated and summarized in **Table 2.5**. Training datasets at different mixing conditions generally showed considerable variation in correction performances on correcting the coarse mesh modeling results.

First, for the training dataset of one single rotational speed (60, 120, and 150 rpm), the correction performance was similar to that of the baseline ANN model trained with the 90-rpm dataset. The RMSE values were reduced by about 10% to 20% by varying the rotational speeds. It was worth noting that the best correction performance for a mixing speed consistently matched the training rotational speed, and the correction performance decreased as the speed for correction deviated from the training speed. For example, when the rotational speed of 120 rpm was used as the training dataset, the best correction performance was observed at the same rotational speed, while the %RMSE increased when the correction speed was changing away from the training speed. This %RMSE trend can be explained by the similarity between the training and prediction (correction) datasets, where the ANN model performs better if the training and prediction datasets are similar. This trend can also be observed for the correction of the 30 rpm modeling results. For all the ANN models with different training datasets (60, 90, 120, and 150 rpm), the coarse-mesh results of 30 rpm cannot be improved, which was due to different flow patterns between 30 rpm and other rpms (shown in **Figure 2.10**). However, when 30 rpm was used to train the ANN model, the RMSE for correction of 30 rpm was significantly improved by about 40%, indicating enhanced performance of the ANN model. The results implied that the developed ANN model in this study, when trained with data from one single speed, is limited by its generalization ability, where the training speed was the critical contributor. A similar result was reported by Hanna et al. (2020) that “closeness” between the training and the correction flows influenced the capability of the ML model.

When the dataset of multiple rotational speeds was used for training, the trained ANN model exhibited no improvement in error correction capability. The ANN model trained with the dataset consisting of 30 and 60 rpm showed good performance of error corrections for all five rotational speeds, indicating a better generalization of this trained ANN model. This result differed from all the other combinations of the training dataset, as those combinations consistently faced difficulties in error correction at 30 rpm. With all other training dataset combinations, the ANN model performance was not improved compared to the single training rotational speed. The performance of the ANN model trained with 30 rpm and other rpms (except 60 rpm) was also not good on correcting the 30-rpm model. This implied that simply expanding the training dataset with different flow patterns cannot address the limitations of the current ANN models, and proper selection of training datasets is of great importance to achieve desired model performance.

The lack of accuracy of the model when predicting 30 rpm might be because the flow behavior of 30 rpm is different from the trained rotational speed (90 rpm). The impeller Reynolds number can be calculated to estimate the flow behavior in a mixing bioreactor as (Doran 2013):

$$Re_i = \frac{(\rho D_i^2 N)}{\mu} \tag{2.13}$$

where ρ is the media density, D_i is the impeller diameter, N is the rotations of impeller per second, and μ is the media viscosity. The Reynolds numbers of 30 and 90 rpm were estimated as 800 and 4000, representing early and late transitional flow behavior in mixer conditions, respectively. Unlike fluid flow in a pipe where the transition from laminar to turbulent has been clearly defined from $2100<Re<4000$, the transition in stirred vessels has been set to a much wider range where a $Re_i<10$ is a considered laminar and a fully turbulent flow can only be guaranteed when $Re_i>10{,}000$ (Doran 2013). This can bring some complications to the k-ε turbulence model used in this study. Although it is known for being the most widely used approach due to its low computational requirements and overall good approximations of mean flow, it has its limitations. This model ignores the viscous sublayer and therefore leads to errors in the near-wall areas. Models such as the

Shear Stress Transport (SST), which combines *k*-*ε* with *k*-*ω*, take this region into account but require a much finer mesh near the walls to solve, leading to an increase in computational requirements (Coroneo et al. 2011; Singh et al. 2011). Another limitation of the *k*-*ε* model is it assumes the existence of isotropic turbulence which is why most of its satisfactory results are reported at high Reynolds numbers (Joshi et al. 2011a). The LES models can accurately calculate flows in laminar, transitional, or turbulent regime but are significantly more computationally intensive than typical RANS approaches. Despite these limitations, the *k*-*ε* model was considered to generate a good starting point to test the machine learning mesh-induced error correction since the algorithm is not coupled with the solver but is rather used as postprocessing to improve the results obtained from a CFD modeling result.

3.4 Generalization of the trained model/approach for predicting other case study scenarios

The developed training approach was applied in other case study scenarios. All cases used the baseline model structure and mixing speed (90 rpm). First, the baseline ANN-model approach was used to develop a new ANN model to predict and correct the Kolmogorov length (**Table 2.6**). The ANN was able to properly predict and correct the Kolmogorov length values for all mixing speeds evaluated, including the 30 rpm, although previous results for z-velocity component showed that baseline ANN model could not correct the coarse-mesh-induced error at this rotational speed. The different observations between velocity and Kolmogorov length might be attributed to their characteristics of complexity. The velocity profile is a vector with three components, making it difficult to train a robust ML model for prediction and correction; while the Kolmogorov length is a scalar value, without the concern of direction. The promising results in Kolmogorov length prediction showed that the ANN-based ML approach can be useful in efficiently correcting this important parameter that is critical for bioreactor performance.

The second case study explored using the trained model to predict and correct the velocity profile and Kolmogorov length for fluids with other viscosity values (**Table 2.7**).

This application case is similar to predicting flow generated by varying mixing speeds as it is a function of global impeller Reynolds number. In this case, the Re_i at 90 rpm is 4800 for 0.5 mPa·s, 2400 for 1 mPa·s, and 1200 for 2 mPa·s. These results are similar to those obtained by Hanna et al., (2020), where the kinematic viscosity was modified to generate different global Reynolds numbers 6000, 8000, 10000, and 12000 and their ANN model trained with a combination of three was able to properly correct results when interpolating and extrapolating. These results suggested that the trained model can be extended to predict and correct similar mixing scenarios with similar correction results.

Finally, the third case study was expanding the use of the trained ANN model to predict and correct z-velocity profile and Kolmogorov length scale across different impeller geometries. **Table 2.8** results indicated that the previously trained baseline model using original impeller lacks the generalization capability to correct velocity components across geometries with the current setup, but it can correct Kolmogorov length scales. As mentioned previously, the Kolmogorov length scale is a scalar, and the velocity is separated into three vectors which may hinder the model’s performance.

3.5 Usefulness, limitations, and future work

This study demonstrated ANN-based ML models that can use one set of CFD result at one mixing condition to predict and correct the coarse-mesh-induced-errors of various parameters (i.e., velocity, Kolmogorov length) for other mixing scenarios of different rotational speed and fluid viscosity with different accuracy improvement. This ML approach is more computationally efficient than commonly used CFD modeling approach with optimized mesh. For example, in this study, the CFD model with optimized mesh had a computational time of 2.5 hours; and the coarse mesh model and the baseline ML model prediction had a computational time of 5 min and 10 min, indicating a 90% computational time improvement. The proposed approach is also more computationally efficient than the common CFD approach to improve modeling efficiency by initializing the fine-mesh results with coarse-mesh results. This improved CFD method reduced the total computational time from 2.5 hours to 40 min (5 min for coarse-mesh model and 35 min for initialized fine mesh modeling). Thus, the ML approach could improve the modeling efficiency by ~63% in computational time reduction when compared to the improved CFD modeling strategy. The baseline ANN model structure can be further optimized to improve performance.

The current performance of the ANN model has shown a limitation in its ability to generalize well when dealing with low similarity datasets, particularly in fluid patterns as seen in this research. To address this issue, future research will require a more robust ANN model that can balance specific accuracy and generalization (Dębska and Guzowska-Świder 2011). One way to improve generalization is by increasing the size of the training dataset and feeding the model with data from various scenarios. Alternatively, as Hanna et al. (2020) proposed, implementing a suitable metric for evaluating the closeness between training and correction as a prior assessment can aid in determining appropriate selection of the training dataset, especially concerning speed range. To further enhance modeling performance, optimizing the ANN structure through hyperparameter optimization with advanced ML techniques such as Bayesian optimization and Genetic algorithm can be helpful. These techniques have been proven to be efficient and powerful tools to enhance overall performance, prediction accuracy and generalization of black-box models like ANN (Alibrahim and Ludwig 2021; Liu et al. 2023). Given limitations on dataset size, several strategies can be employed to augment generalizability. One such strategy involves training multiple neural networks and subsequently averaging their outputs. Alternatively, Bayesian regularization can be utilized which provides an estimation of effective usage of weights and biases within the network (Dan Foresee and Hagan 1997).

The scope of this study was solely to demonstrate the proposed ANN-based approach’s ability to correct velocity patterns. However, it is essential to note that this demonstration does not impose any restrictions on the broader applicability of the approach. With more descent dataset selection and model optimization included, this model can be readily adapted to predict additional parameters in more complicated CFD simulation, such as shear stress, nutrient and gas diffusion rates, etc., that are critical for cell culture studies. The proposed approach may also be used to design bioreactors and impellers with improved computational efficiency.

4 Conclusion

The ANN-based ML model was able to predict and correct the coarse-mesh-induced errors with significantly reduced computational. Increasing the number of neurons in a single hidden layer increased training and prediction performance, however, using 100 neurons was considered to take too long to be feasible. Further normalization of the input data, beyond the mesh cell-size normalization applied to the first and second velocity derivatives, did not improve the ANN model's performance. The ANN model was able to use a single mixing speed as training to correct all others with average improvements of ~20%. However, performance in predicting and correcting coarse mesh-induced error in z-velocity profiles was highly dependent on the closeness of the dataset in training and correction. However, the baseline model was able to correct the Kolmogorov length scale across all mixing speeds when trained with 90 rpm. The generalization of the model across different impeller geometries was evaluated and the ANN model cannot correct z-velocity but it corrected Kolmogorov length with an average 13% improvement across geometries. The good performance of the model for Kolmogorov was attributed to it being a scalar value whereas the velocity is separated into three vectors and the interaction between the three may not be learnt properly with this approach. This approach may be used to correct other variables of interest, such as shear stress, nutrient, and gas diffusion rates for more complicated CFD models of large-scale bioreactors. This machine learning approach in correcting coarse-mesh-induced error could also be modified to work as a digital twin for cell culture bioreactors and other mixing applications with significantly improved computational efficiency.

Acknowledgments

This work was supported by the AI Tennessee Initiative at the University of Tennessee.

REFERENCES

Adamo L, García-Cardeña G (2011) Directed stem cell differentiation by fluid mechanical forces. Antioxid Redox Signal 15:1463–1473. https://doi.org/10.1089/ars.2011.3907

Alibrahim H, Ludwig SA (2021) Hyperparameter Optimization: Comparing Genetic Algorithm against Grid Search and Bayesian Optimization. In: 2021 IEEE Congress on Evolutionary Computation (CEC). IEEE, Kraków, Poland, pp 1551–1559

Allan SJ, De Bank PA, Ellis MJ (2019) Bioprocess Design Considerations for Cultured Meat Production With a Focus on the Expansion Bioreactor. Frontiers in Sustainable Food Systems 3:

Bandi P, Manelil NP, Maiya MP, et al (2023) CFD driven prediction of mean radiant temperature inside an automobile cabin using machine learning. Thermal Science and Engineering Progress 37:101619. https://doi.org/10.1016/j.tsep.2022.101619

Berdugo C (2010) Cell Damage Mechanisms and Stress Response in Animal Cell Culture. The Ohio State University

Berry JD, Liovic P, Šutalo ID, et al (2016) Characterisation of stresses on microcarriers in a stirred bioreactor. Applied Mathematical Modelling 40:6787–6804. https://doi.org/10.1016/j.apm.2016.02.025

Bilgen B, Chang-Mateu IM, Barabino GA (2005) Characterization of mixing in a novel wavy-walled bioreactor for tissue engineering. Biotechnology and Bioengineering 92:907–919. https://doi.org/10.1002/bit.20667

Bilger C, Aboukhedr M, Vogiatzaki K, Cant RS (2017) Evaluation of two-phase flow solvers using Level Set and Volume of Fluid methods. Journal of Computational Physics 345:665–686. https://doi.org/10.1016/j.jcp.2017.05.044

Bliatsiou C, Malik A, Böhm L, Kraume M (2019) Influence of Impeller Geometry on Hydromechanical Stress in Stirred Liquid/Liquid Dispersions. Ind Eng Chem Res 58:2537–2550. https://doi.org/10.1021/acs.iecr.8b03654

Bodiou V, Moutsatsou P, Post MJ (2020) Microcarriers for Upscaling Cultured Meat Production. Front Nutr 7:. https://doi.org/10.3389/fnut.2020.00010

Borys BS, Le A, Roberts EL, et al (2019) Using computational fluid dynamics (CFD) modeling to understand murine embryonic stem cell aggregate size and pluripotency distributions in stirred suspension bioreactors. Journal of Biotechnology 304:16–27. https://doi.org/10.1016/j.jbiotec.2019.08.002

Borys BS, Roberts EL, Le A, Kallos MS (2018) Scale-up of embryonic stem cell aggregate stirred suspension bioreactor culture enabled by computational fluid dynamics modeling. Biochemical Engineering Journal 133:157–167. https://doi.org/10.1016/j.bej.2018.02.005

Cantarero Rivera FJ, Chen J (2022) Computational fluid dynamics modeling of cell cultures in bioreactors and its potential for cultivated meat production—A mini-review. Future Foods 6:100195. https://doi.org/10.1016/j.fufo.2022.100195

Catapano G, Czermak P, Eibl R, et al (2009) Bioreactor Design and Scale-Up. In: Eibl R, Eibl D, Pörtner R, et al. (eds) Cell and Tissue Reaction Engineering: With a Contribution by Martin Fussenegger and Wilfried Weber. Springer, Berlin, Heidelberg, pp 173–259

Chao T-C, Das DB (2015) Numerical simulation of coupled cell motion and nutrient transport in NASA's rotating bioreactor. Chemical Engineering Journal 259:961–971. https://doi.org/10.1016/j.cej.2014.08.077

Chen R, Jin X, Li H (2022) A machine learning based solver for pressure Poisson equations. Theoretical and Applied Mechanics Letters 12:100362. https://doi.org/10.1016/j.taml.2022.100362

Chiley V, Sharapov I, Kosson A, et al (2019) Online Normalization for Training Neural Networks. In: Wallach H, Larochelle H, Beygelzimer A, et al. (eds) Advances in Neural Information Processing Systems. Curran Associates, Inc.

Chisti Y (2001) Hydrodynamic Damage to Animal Cells. Critical Reviews in Biotechnology 21:67–110. https://doi.org/10.1080/20013891081692

Choi J, Lee SY, Yoo Y-M, Kim CH (2017) Maturation of Adipocytes is Suppressed by Fluid Shear Stress. Cell Biochem Biophys 75:87–94. https://doi.org/10.1007/s12013-016-0771-4

Cinbiz MN, Tığlı RS, Beşkardeş IG, et al (2010) Computational fluid dynamics modeling of momentum transport in rotating wall perfused bioreactor for cartilage tissue engineering. Journal of Biotechnology 150:389–395. https://doi.org/10.1016/j.jbiotec.2010.09.950

Consolo F, Bariani C, Mantalaris A, et al (2012) Computational modeling for the optimization of a cardiogenic 3D bioprocess of encapsulated embryonic stem cells. Biomech Model Mechanobiol 11:261–277. https://doi.org/10.1007/s10237-011-0308-0

Coroneo M, Montante G, Paglianti A, Magelli F (2011) CFD prediction of fluid flow and mixing in stirred tanks: Numerical issues about the RANS simulations. Computers & Chemical Engineering 35:1959–1968. https://doi.org/10.1016/j.compchemeng.2010.12.007

Corsini A, Delibra G, Sheard AG (2013) A Critical Review of Computational Methods and Their Application in Industrial Fan Design. ISRN Mechanical Engineering 2013:1–20. https://doi.org/10.1155/2013/625175

Corti A, Chiastra C, Colombo M, et al (2020) A fully coupled computational fluid dynamics – agent-based model of atherosclerotic plaque development: Multiscale modeling framework and parameter sensitivity analysis. Computers in Biology and Medicine 118:103623. https://doi.org/10.1016/j.compbiomed.2020.103623

Cross MM (1979) Relation between viscoelasticity and shear-thinning behaviour in liquids. Rheol Acta 18:609–614. https://doi.org/10.1007/BF01520357

Croughan MS, Hamel J-F, Wang DIC (2000) Hydrodynamic effects on animal cells grown in microcarrier cultures. Biotechnol Bioeng 67:841–852. https://doi.org/10.1002/(SICI)1097-0290(20000320)67:6<841::AID-BIT19>3.0.CO;2-K

Croughan MS, Hamel J-F, Wang DIC (1987) Hydrodynamic effects on animal cells grown in microcarrier cultures. Biotechnology and Bioengineering 29:130–141. https://doi.org/10.1002/bit.260290117

Cytiva (2021) Microcarrier Cell Culture Principles and Methods. In: Cytiva Handbooks. https://www.cytivalifesciences.com/en/us/support/handbooks. Accessed 1 Nov 2021

Czermak P, Pörtner R, Brix A (2009) Special Engineering Aspects. In: Eibl R, Eibl D, Pörtner R, et al. (eds) Cell and Tissue Reaction Engineering: With a Contribution by Martin Fussenegger and Wilfried Weber. Springer, Berlin, Heidelberg, pp 83–172

Dan Foresee F, Hagan MT (1997) Gauss-Newton approximation to Bayesian learning. In: Proceedings of International Conference on Neural Networks (ICNN'97). IEEE, Houston, TX, USA, pp 1930–1935

Dębska B, Guzowska-Świder B (2011) Application of artificial neural network in food classification. Analytica Chimica Acta 705:283–291. https://doi.org/10.1016/j.aca.2011.06.033

Delafosse A, Loubière C, Calvo S, et al (2018) Solid-liquid suspension of microcarriers in stirred tank bioreactor – Experimental and numerical analysis. Chemical Engineering Science 180:52–63. https://doi.org/10.1016/j.ces.2018.01.001

Ding Z, Tiwari SS, Tyagi M, Nandakumar K (2022) Computational fluid dynamic simulations of regular bubble patterns in pulsed fluidized beds using a two-fluid model. The Canadian Journal of Chemical Engineering 100:405–422. https://doi.org/10.1002/cjce.24082

Dong C, Loy CC, He K, Tang X (2016) Image Super-Resolution Using Deep Convolutional Networks. IEEE Transactions on Pattern Analysis and Machine Intelligence 38:295–307. https://doi.org/10.1109/TPAMI.2015.2439281

Doran PM (2013) Fluid Flow. In: Bioprocess Engineering Principles. Elsevier, pp 201–254

Ebrahimi M, Tamer M, Villegas RM, et al (2019) Application of CFD to Analyze the Hydrodynamic Behaviour of a Bioreactor with a Double Impeller. Processes 7:694. https://doi.org/10.3390/pr7100694

Eibl R, Eibl D, Pörtner R, et al (2009a) Cell and Tissue Reaction Engineering. Springer Berlin Heidelberg, Berlin, Heidelberg

Eibl R, Werner S, Eibl D (2009b) Bag Bioreactor Based on Wave-Induced Motion: Characteristics and Applications. Advances in biochemical engineering/biotechnology 115:55–87. https://doi.org/10.1007/10_2008_15

Freiberger F, Budde J, Ateş E, et al (2022) New Insights from Locally Resolved Hydrodynamics in Stirred Cell Culture Reactors. Processes 10:107. https://doi.org/10.3390/pr10010107

Freshney RI (2010) Culture of animal cells: a manual of basic technique and specialized applications. Wiley-Blackwell, Hoboken

Fukami K, Fukagata K, Taira K (2019) Super-resolution reconstruction of turbulent flows with machine learning. J Fluid Mech 870:106–120. https://doi.org/10.1017/jfm.2019.238

Gareau T, Lara GG, Shepherd RD, et al (2014) Shear stress influences the pluripotency of murine embryonic stem cells in stirred suspension bioreactors. Journal of Tissue Engineering and Regenerative Medicine 8:268–278. https://doi.org/10.1002/term.1518

Ghasemian M, Layton C, Nampe D, et al (2020) Hydrodynamic characterization within a spinner flask and a rotary wall vessel for stem cell culture. Biochemical Engineering Journal 157:107533. https://doi.org/10.1016/j.bej.2020.107533

GökhanAksu CO Mehmet TahaEser (2019) The Effect of the Normalization Method Used in Different Sample Sizes on the Success of Artificial Neural Network Model. JOR 6:170–192

Gong Z, Zhong P, Hu W (2019) Diversity in Machine Learning. IEEE Access 7:64323–64350. https://doi.org/10.1109/ACCESS.2019.2917620

Hanga MP, de la Raga FA, Moutsatsou P, et al (2021) Scale-up of an intensified bioprocess for the expansion of bovine adipose-derived stem cells (bASCs) in stirred tank bioreactors. Biotechnology and Bioengineering 118:3175–3186. https://doi.org/10.1002/bit.27842

Hanna BN, Dinh NT, Youngblood RW, Bolotnov IA (2020) Machine-learning based error prediction approach for coarse-grid Computational Fluid Dynamics (CG-

CFD). Progress in Nuclear Energy 118:103140. https://doi.org/10.1016/j.pnucene.2019.103140

Haringa C (2022) An analysis of organism lifelines in an industrial bioreactor using Lattice-Boltzmann CFD. Engineering in Life Sciences n/a: https://doi.org/10.1002/elsc.202100159

Hu W, Berdugo C, Chalmers JJ (2011) The potential of hydrodynamic damage to animal cells of industrial relevance: current understanding. Cytotechnology 63:445–460. https://doi.org/10.1007/s10616-011-9368-3

Huang Z, Odeleye AOO, Ye H, et al (2018) Fluid dynamic characterization of a fluidized-bed perfusion bioreactor with CFD–DEM simulation. Journal of Chemical Technology & Biotechnology 93:2316–2330. https://doi.org/10.1002/jctb.5576

Hughes JP, Davies JM, Jones TER (1998) Concentric cylinder end effects and fluid inertia effects in controlled stress rheometry: part I: numerical simulation. Journal of Non-Newtonian Fluid Mechanics 77:79–101. https://doi.org/10.1016/S0377-0257(97)00102-X

Humbird D (2020) Scale-Up Economics for Cultured Meat: Techno-Economic Analysis and Due Diligence. https://doi.org/10.17605/OSF.IO/AJSU9

Jeske R, Lewis S, Tsai A-C, et al (2021) Agitation in a microcarrier-based spinner flask bioreactor modulates homeostasis of human mesenchymal stem cells. Biochemical Engineering Journal 168:107947. https://doi.org/10.1016/j.bej.2021.107947

Joshi JB, Nere NK, Rane CV, et al (2011a) CFD simulation of stirred tanks: Comparison of turbulence models. Part I: Radial flow impellers. Can J Chem Eng 89:23–82. https://doi.org/10.1002/cjce.20446

Joshi JB, Nere NK, Rane CV, et al (2011b) CFD simulation of stirred tanks: Comparison of turbulence models (Part II: Axial flow impellers, multiple impellers and multiphase dispersions). Can J Chem Eng 89:754–816. https://doi.org/10.1002/cjce.20465

Jossen V, Eibl R, Kraume M, Eibl D (2018) Growth Behavior of Human Adipose Tissue-Derived Stromal/Stem Cells at Small Scale: Numerical and Experimental Investigations. Bioengineering (Basel) 5:. https://doi.org/10.3390/bioengineering5040106

Julaey M, Hosseini M, Amani H (2016) Stem Cells Culture Bioreactor Fluid Flow, Shear Stress and Microcarriers Dispersion Analysis Using Computational Fluid Dynamics. Journal of Applied Biotechnology Reports 3:425–431

Kaiser S, Jossen V, Schirmaier C, et al (2013) Fluid Flow and Cell Proliferation of Mesenchymal Adipose-Derived Stem Cells in Small-Scale, Stirred, Single-Use Bioreactors. Chemie Ingenieur Technik 85:95–102. https://doi.org/10.1002/cite.201200180

Karimi Alavijeh M, Baker I, Lee YY, Gras SL (2022) Digitally enabled approaches for the scale up of mammalian cell bioreactors. Digital Chemical Engineering 4:100040. https://doi.org/10.1016/j.dche.2022.100040

Kaul H, Cui Z, Ventikos Y (2013) A Multi-Paradigm Modeling Framework to Simulate Dynamic Reciprocity in a Bioreactor. PLOS ONE 8:e59671. https://doi.org/10.1371/journal.pone.0059671

Kelly WJ (2008) Using computational fluid dynamics to characterize and improve bioreactor performance. Biotechnology and Applied Biochemistry 49:225–238. https://doi.org/10.1042/BA20070177

Khademi R, Mohebbi-Kalhori D, Hadjizadeh A (2014) Computational study of culture conditions and nutrient supply in a hollow membrane sheet bioreactor for large-scale bone tissue engineering. J Artif Organs 17:69–80. https://doi.org/10.1007/s10047-013-0732-2

Kiener A, Langer S, Bekemeyer P (2023) Data-driven correction of coarse grid CFD simulations. Computers & Fluids 264:105971. https://doi.org/10.1016/j.compfluid.2023.105971

Kochkov D, Smith JA, Alieva A, et al (2021) Machine learning–accelerated computational fluid dynamics. Proc Natl Acad Sci USA 118:e2101784118. https://doi.org/10.1073/pnas.2101784118

Kolkmann AM, Post MJ, Rutjens MAM, et al (2020) Serum-free media for the growth of primary bovine myoblasts. Cytotechnology 72:111–120. https://doi.org/10.1007/s10616-019-00361-y

Konijn BJ, Sanderink OBJ, Kruyt NP (2014) Experimental study of the viscosity of suspensions: Effect of solid fraction, particle size and suspending liquid. Powder Technology 266:61–69. https://doi.org/10.1016/j.powtec.2014.05.044

Kreitmayer D, Gopireddy SR, Aki Y, et al (2023) Scale-up analysis of geometrically dissimilar single-use bioreactors. Biotechnol Bioeng. https://doi.org/10.1002/bit.28529

Kreitmayer D, Gopireddy SR, Matsuura T, et al (2022) Numerical and experimental characterization of the single-use bioreactor Xcellerex^{TM} XDR-200. Biochemical Engineering Journal 177:108237. https://doi.org/10.1016/j.bej.2021.108237

Launder BE, Spalding DB (1974) The numerical computation of turbulent flows. Computer Methods in Applied Mechanics and Engineering 3:269–289. https://doi.org/10.1016/0045-7825(74)90029-2

Le DK, Guo M, Yoon JY (2023) A hybrid CFD – Deep Learning methodology to improve the accuracy of cut-off diameter prediction in coarse-grid simulations for cyclone separators. Journal of Aerosol Science 170:106143. https://doi.org/10.1016/j.jaerosci.2023.106143

Levenberg K (1944) A method for the solution of certain non-linear problems in least squares. Quarterly of Applied Mathematics 2:164–168

Li X, Zhang G, Zhao X, et al (2020) A conceptual air-lift reactor design for large scale animal cell cultivation in the context of in vitro meat production. Chemical Engineering Science 211:115269. https://doi.org/10.1016/j.ces.2019.115269

Liu B, Tang J, Huang H, Lu X-Y (2020) Deep learning methods for super-resolution reconstruction of turbulent flows. Physics of Fluids 32:025105. https://doi.org/10.1063/1.5140772

Liu G, Zhao H, Deng J, et al (2023) Performance improvement of CO2 two-phase ejector by combining CFD modeling, artificial neural network and genetic algorithm.

International Journal of Refrigeration S0140700723001998. https://doi.org/10.1016/j.ijrefrig.2023.07.005

Liu Z, Zhang R, Li L, et al (2022) Prediction of the viscosity of solid–liquid mixtures using a virtual viscometer based on computational fluid dynamics. Arch Appl Mech 92:3769–3779. https://doi.org/10.1007/s00419-022-02261-8

Lucena-Thomas JP de, Boonprasirt P, Luetchford K, et al (2020) Bed expansion properties of tissue engineering particles in a fluidised bed bioreactor. Biochemical Engineering Journal 160:107632. https://doi.org/10.1016/j.bej.2020.107632

Lynch J, Pierrehumbert R (2019) Climate Impacts of Cultured Meat and Beef Cattle. Frontiers in Sustainable Food Systems 3:

Marquardt DW (1963) An Algorithm for Least-Squares Estimation of Nonlinear Parameters. Journal of the Society for Industrial and Applied Mathematics 11:431–441. https://doi.org/10.1137/0111030

Marsh DTJ (2017) Engineering Characterisation of a Rocked Bag Bioreactor for Improved Process Development and Scale-Up. Doctoral, UCL (University College London)

Masters JR, Stacey GN (2007) Changing medium and passaging cell lines. Nat Protoc 2:2276–2284. https://doi.org/10.1038/nprot.2007.319

Mattick CS (2018) Cellular agriculture: The coming revolution in food production. Bulletin of the Atomic Scientists 74:32–35. https://doi.org/10.1080/00963402.2017.1413059

Mattick CS, Landis AE, Allenby BR, Genovese NJ (2015) Anticipatory Life Cycle Analysis of In Vitro Biomass Cultivation for Cultured Meat Production in the United States. Environ Sci Technol 49:11941–11949. https://doi.org/10.1021/acs.est.5b01614

McClure DD, Kavanagh JM, Fletcher DF, Barton GW (2016) Characterizing bubble column bioreactor performance using computational fluid dynamics. Chemical Engineering Science 144:58–74. https://doi.org/10.1016/j.ces.2016.01.016

Mendonça da Silva J, Erro E, Awan M, et al (2020) Small-Scale Fluidized Bed Bioreactor for Long-Term Dynamic Culture of 3D Cell Constructs and in vitro Testing. Frontiers in Bioengineering and Biotechnology 8:

Menshutina NV, Guseva EV, Safarov RR, Boudrant J (2020) Modelling of hollow fiber membrane bioreactor for mammalian cell cultivation using computational hydrodynamics. Bioprocess Biosyst Eng 43:549–567. https://doi.org/10.1007/s00449-019-02249-9

Messmer T, Klevernic I, Furquim C, et al (2022) A serum-free media formulation for cultured meat production supports bovine satellite cell differentiation in the absence of serum starvation. Nat Food 3:74–85. https://doi.org/10.1038/s43016-021-00419-1

Mohebbi-Kalhori D, Behzadmehr A, Doillon CJ, Hadjizadeh A (2012) Computational modeling of adherent cell growth in a hollow-fiber membrane bioreactor for large-scale 3-D bone tissue engineering. J Artif Organs 15:250–265. https://doi.org/10.1007/s10047-012-0649-1

Mueller S, Llewellin EW, Mader HM (2010) The rheology of suspensions of solid particles. Proc R Soc A 466:1201–1228. https://doi.org/10.1098/rspa.2009.0445

Nadal-Rey G, McClure DD, Kavanagh JM, et al (2022) Computational fluid dynamics modelling of hydrodynamics, mixing and oxygen transfer in industrial bioreactors with Newtonian broths. Biochemical Engineering Journal 177:108265. https://doi.org/10.1016/j.bej.2021.108265

Nadal-Rey G, McClure DD, Kavanagh JM, et al (2021) Development of dynamic compartment models for industrial aerobic fed-batch fermentation processes. Chemical Engineering Journal 420:130402. https://doi.org/10.1016/j.cej.2021.130402

Naskar S, Kumaran V, Basu B (2017) On The Origin of Shear Stress Induced Myogenesis Using PMMA Based Lab-on-Chip. ACS Biomater Sci Eng 3:1154–1171. https://doi.org/10.1021/acsbiomaterials.7b00206

OECD, Food, Nations AO of the U (2021) OECD-FAO Agricultural Outlook 2021-2030

Öncül AA, Kalmbach A, Genzel Y, et al (2010) Characterization of flow conditions in 2 L and 20 L wave bioreactors® using computational fluid dynamics. Biotechnol Progress 26:101–110. https://doi.org/10.1002/btpr.312

Papoutsakis E (1991) Fluid-mechanical damage of animal cells in bioreactors. Trends in Biotechnology 9:427–437. https://doi.org/10.1016/0167-7799(91)90145-8

Patel P, Vaidya, P, Singh G (2014) An overview of impellers, velocity profile and reactor design. Bangalore

Pirnia P, Duhaime F, Ethier Y, Dubé J-S (2019) Drag Force Calculations in Polydisperse DEM Simulations with the Coarse-Grid Method: Influence of the Weighting Method and Improved Predictions Through Artificial Neural Networks. Transp Porous Med 129:837–853. https://doi.org/10.1007/s11242-019-01308-9

Ponnuru K, Wu J, Ashok P, et al (2014) Analysis of stem cell culture performance in a microcarrier bioreactor system. Technical Proceedings of the 2014 NSTI Nanotechnology Conference and Expo, NSTI-Nanotech 2014 2:132–135

Poon C (2022) Measuring the density and viscosity of culture media for optimized computational fluid dynamics analysis of in vitro devices. Journal of the Mechanical Behavior of Biomedical Materials 126:105024. https://doi.org/10.1016/j.jmbbm.2021.105024

Pörtner R (2015) Bioreactors for Mammalian Cells. In: Al-Rubeai M (ed) Animal cell culture. Springer International Publishing, Cham, pp 89–135

Post MJ (2014) Cultured beef: medical technology to produce food. Journal of the Science of Food and Agriculture 94:1039–1041. https://doi.org/10.1002/jsfa.6474

Post MJ (2012) Cultured meat from stem cells: Challenges and prospects. Meat Science 92:297–301. https://doi.org/10.1016/j.meatsci.2012.04.008

Post MJ, Levenberg S, Kaplan DL, et al (2020) Scientific, sustainability and regulatory challenges of cultured meat. Nature Food 1:403–415. https://doi.org/10.1038/s43016-020-0112-z

Raissi M, Karniadakis GE (2018) Hidden physics models: Machine learning of nonlinear partial differential equations. Journal of Computational Physics 357:125–141. https://doi.org/10.1016/j.jcp.2017.11.039

Ranade R, Hill C, Pathak J (2021) DiscretizationNet: A machine-learning based solver for Navier–Stokes equations using finite volume discretization. Computer Methods in Applied Mechanics and Engineering 378:113722. https://doi.org/10.1016/j.cma.2021.113722

Rousseau PM, Soulaïmani A, Sabourin M (2013) Comparison between structured hexahedral and hybrid tetrahedral meshes generated by commercial software for CFD hydraulic turbine analysis. https://doi.org/10.13140/2.1.2574.4960

Runstadler PW, Tung AS, Hayman EG, et al (1990) Continuous Culture with Macroporous Matrix, Fluidized Bed Systems. In: Large-Scale Mammalian Cell Culture Technology. Routledge

Scully J, Considine LB, Smith MT, et al (2020) Beyond heuristics: CFD-based novel multiparameter scale-up for geometrically disparate bioreactors demonstrated at industrial 2kL–10kL scales. Biotechnology and Bioengineering 117:1710–1723. https://doi.org/10.1002/bit.27323

Seb Rengma T, Kumar S, Kumar Gupta M, Subbarao PMV (2023) Performance investigation on blade arc angle and blade shape factor of a Savonius hydrokinetic turbine using artificial neural network. Energy Sources, Part A: Recovery, Utilization, and Environmental Effects 45:8104–8124. https://doi.org/10.1080/15567036.2023.2226096

Simion AI, Grigoras CG, Bardaşu LE, Dabija A (2017) Modelling of the thermophysical lactic acid aqueous solutions. Density and viscosity. Food and Environment Safety Journal; Vol 11, No 4 (2012)

Singh D, Singh B (2022) Feature wise normalization: An effective way of normalizing data. Pattern Recognition 122:108307. https://doi.org/10.1016/j.patcog.2021.108307

Singh H, Fletcher DF, Nijdam JJ (2011) An assessment of different turbulence models for predicting flow in a baffled tank stirred with a Rushton turbine. Chemical Engineering Science 66:5976–5988. https://doi.org/10.1016/j.ces.2011.08.018

Smetana S, Mathys A, Knoch A, Heinz V (2015) Meat alternatives: life cycle assessment of most known meat substitutes. Int J Life Cycle Assess 20:1254–1267. https://doi.org/10.1007/s11367-015-0931-6

Spann R, Glibstrup J, Pellicer-Alborch K, et al (2019) CFD predicted pH gradients in lactic acid bacteria cultivations. Biotechnology and Bioengineering 116:769–780. https://doi.org/10.1002/bit.26868

Stickel JJ, Powell RL (2005) Fluid Mechanics and Rheology of Dense Suspensions. Annual Review of Fluid Mechanics 37:129–149. https://doi.org/10.1146/annurev.fluid.36.050802.122132

Stout AJ, Mirliani AB, Rittenberg ML, et al (2022) Simple and effective serum-free medium for sustained expansion of bovine satellite cells for cell cultured meat. Commun Biol 5:1–13. https://doi.org/10.1038/s42003-022-03423-8

Svay K, Urrea C, Shamlou PA, Zhang H (2020) Computational fluid dynamics analysis of mixing and gas–liquid mass transfer in wave bag bioreactor. Biotechnology Progress 36:e3049. https://doi.org/10.1002/btpr.3049

Taya M, Kino-oka M (2011) Bioreactors for Animal Cell Cultures. In: Comprehensive Biotechnology. Elsevier, pp 373–382

Telis VRN, Telis-Romero J, Mazzotti HB, Gabas AL (2007) Viscosity of Aqueous Carbohydrate Solutions at Different Temperatures and Concentrations. International Journal of Food Properties 10:185–195. https://doi.org/10.1080/10942910600673636

Teo A, Mantalaris A, Song K, Lim M (2014) A novel perfused rotary bioreactor for cardiomyogenesis of embryonic stem cells. Biotechnol Lett 36:947–960. https://doi.org/10.1007/s10529-014-1456-y

Till Z, Molnár B, Egedy A, Varga T (2018) CFD Based Qualification of Mixing Efficiency of Stirred Vessels. Period Polytech Chem Eng 63:226–238. https://doi.org/10.3311/PPch.12245

Tuomisto HL, Teixeira de Mattos MJ (2011) Environmental Impacts of Cultured Meat Production. Environ Sci Technol 45:6117–6123. https://doi.org/10.1021/es200130u

Ueki M, Tansho N, Sato M, et al (2021) Improved cultivation of Chinese hamster ovary cells in bioreactor with reciprocal mixing. Journal of Bioscience and Bioengineering 132:531–536. https://doi.org/10.1016/j.jbiosc.2021.08.003

Valdiani A, Hansen OK, Nielsen UB, et al (2019) Bioreactor-based advances in plant tissue and cell culture: challenges and prospects. Critical Reviews in Biotechnology 39:20–34. https://doi.org/10.1080/07388551.2018.1489778

Van Beylen K, Papantoniou I, Aerts J-M (2021) Microcarrier Screening and Evaluation for Dynamic Expansion of Human Periosteum-Derived Progenitor Cells in a Xenogeneic Free Medium. Front Bioeng Biotechnol 9:624890. https://doi.org/10.3389/fbioe.2021.624890

Van Liedekerke P, Palm MM, Jagiella N, Drasdo D (2015) Simulating tissue mechanics with agent-based models: concepts, perspectives and some novel results. Comp Part Mech 2:401–444. https://doi.org/10.1007/s40571-015-0082-3

Verma R, Mehan L, Kumar R, et al (2019) Computational fluid dynamic analysis of hydrodynamic shear stress generated by different impeller combinations in stirred bioreactor. Biochemical Engineering Journal 151:107312. https://doi.org/10.1016/j.bej.2019.107312

Villiger TK, Neunstoecklin B, Karst DJ, et al (2018) Experimental and CFD physical characterization of animal cell bioreactors: From micro- to production scale. Biochemical Engineering Journal 131:84–94. https://doi.org/10.1016/j.bej.2017.12.004

Vinuesa R, Brunton SL (2022) Enhancing computational fluid dynamics with machine learning. Nat Comput Sci 2:358–366. https://doi.org/10.1038/s43588-022-00264-7

Wadaugsorn K, Limtrakul S, Vatanatham T, Ramachandran PA (2016) Hydrodynamic behaviors and mixing characteristics in an internal loop airlift reactor based on CFD simulation. Chemical Engineering Research and Design 113:125–139. https://doi.org/10.1016/j.cherd.2016.07.017

Wang B, Wang J (2021) Application of Artificial Intelligence in Computational Fluid Dynamics. Ind Eng Chem Res 60:2772–2790. https://doi.org/10.1021/acs.iecr.0c05045

Werner S, Kaiser SC, Kraume M, Eibl D (2014) Computational fluid dynamics as a modern tool for engineering characterization of bioreactors. Pharmaceutical Bioprocessing 2:85–99

Wilcox DC (2006) Turbulence modeling for CFD, 3rd ed. DCW Industries, La Cãnada, Calif

Wu T, Liu X, An W, et al (2022) A mesh optimization method using machine learning technique and variational mesh adaptation. Chinese Journal of Aeronautics 35:27–41. https://doi.org/10.1016/j.cja.2021.05.018

Wung N, Acott SM, Tosh D, Ellis MJ (2014) Hollow fibre membrane bioreactors for tissue engineering applications. Biotechnol Lett 36:2357–2366. https://doi.org/10.1007/s10529-014-1619-x

Wyma A, Martin-Alarcon L, Walsh T, et al (2018) Non-Newtonian rheology in suspension cell cultures significantly impacts bioreactor shear stress quantification. Biotechnology and Bioengineering 115:2101–2113. https://doi.org/10.1002/bit.26723

Yamamoto K, Sokabe T, Watabe T, et al (2005) Fluid shear stress induces differentiation of Flk-1-positive embryonic stem cells into vascular endothelial cells in vitro. American Journal of Physiology-Heart and Circulatory Physiology 288:H1915–H1924. https://doi.org/10.1152/ajpheart.00956.2004

Yang J, Guertin P, Jia G, et al (2019) Large-scale microcarrier culture of HEK293T cells and Vero cells in single-use bioreactors. AMB Expr 9:70. https://doi.org/10.1186/s13568-019-0794-5

Yang L, Shami A (2020) On hyperparameter optimization of machine learning algorithms: Theory and practice. Neurocomputing 415:295–316. https://doi.org/10.1016/j.neucom.2020.07.061

Zhan C, Hagrot E, Brandt L, Chotteau V (2019) Study of hydrodynamics in wave bioreactors by computational fluid dynamics reveals a resonance phenomenon.

Chemical Engineering Science 193:53–65. https://doi.org/10.1016/j.ces.2018.08.017

Zhang G, Zhao X, Li X, et al (2020) Challenges and possibilities for bio-manufacturing cultured meat. Trends in Food Science & Technology 97:443–450. https://doi.org/10.1016/j.tifs.2020.01.026

Zhang J, Li X, Liu H, et al (2021) Hydrodynamics and mass transfer in spinner flasks: Implications for large scale cultured meat production. Biochemical Engineering Journal 167:107864. https://doi.org/10.1016/j.bej.2020.107864

ANSYS FLUENT 12.0 User's Guide. https://www.afs.enea.it/project/neptunius/docs/fluent/html/ug/main_pre.htm. Accessed 4 Aug 2022

APPENDIX

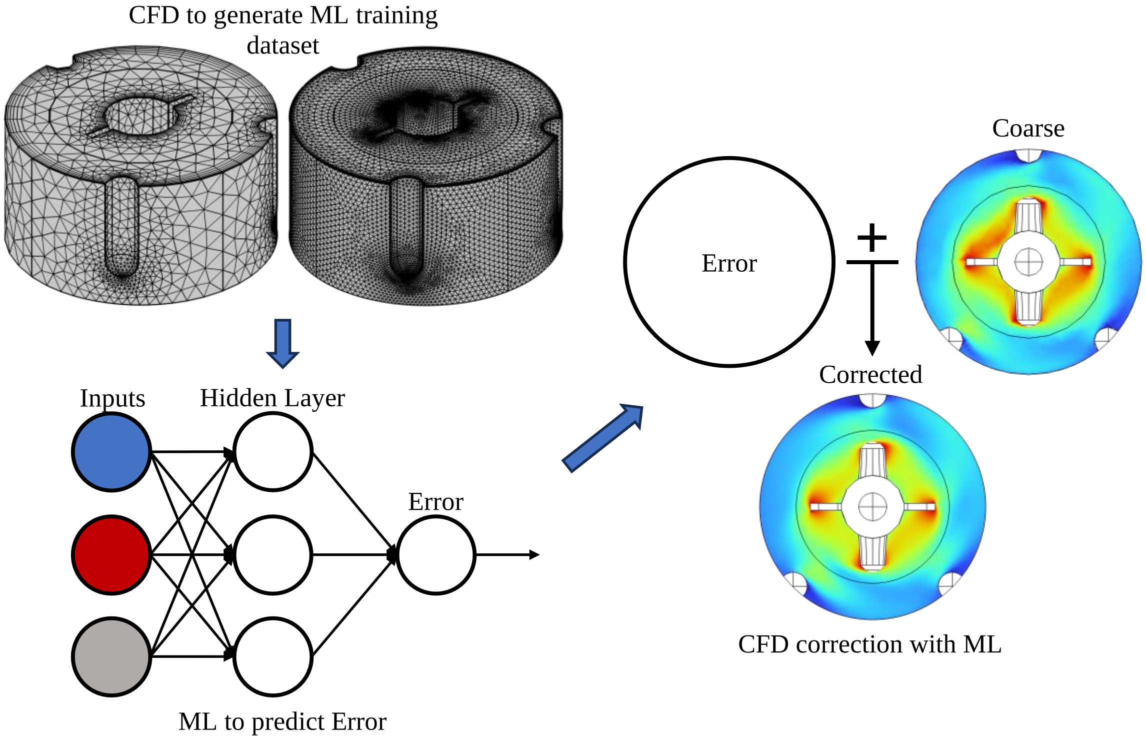

Figure 2.1. Three steps of ANN-based ML model to predict and correct coarse mesh-induced CFD modeling errors in a spinner flask bioreactor.

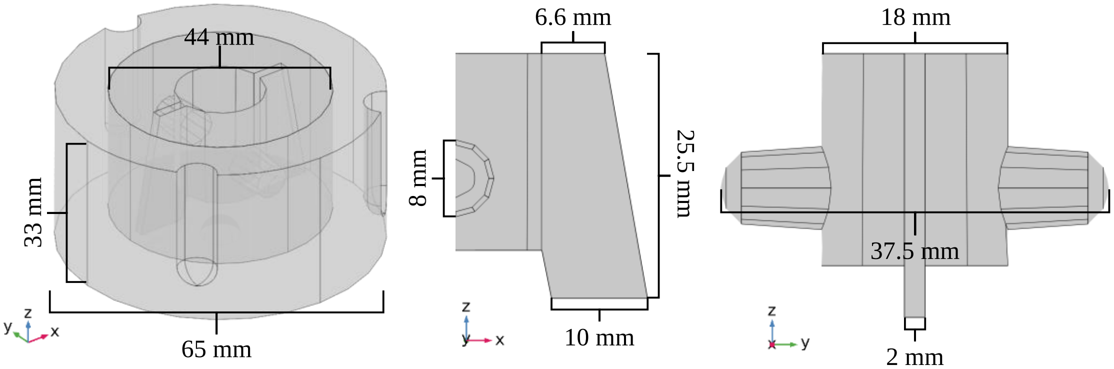

Figure 2.2. The three-dimensional model with dimensions of a Corning®, Series 4500-125spinner flask, with 100 mL working volume. (a) 3D snapshot of whole geometry and impeller side views at (b) xz-coordinate plane and (c) yz-coordinate plane.

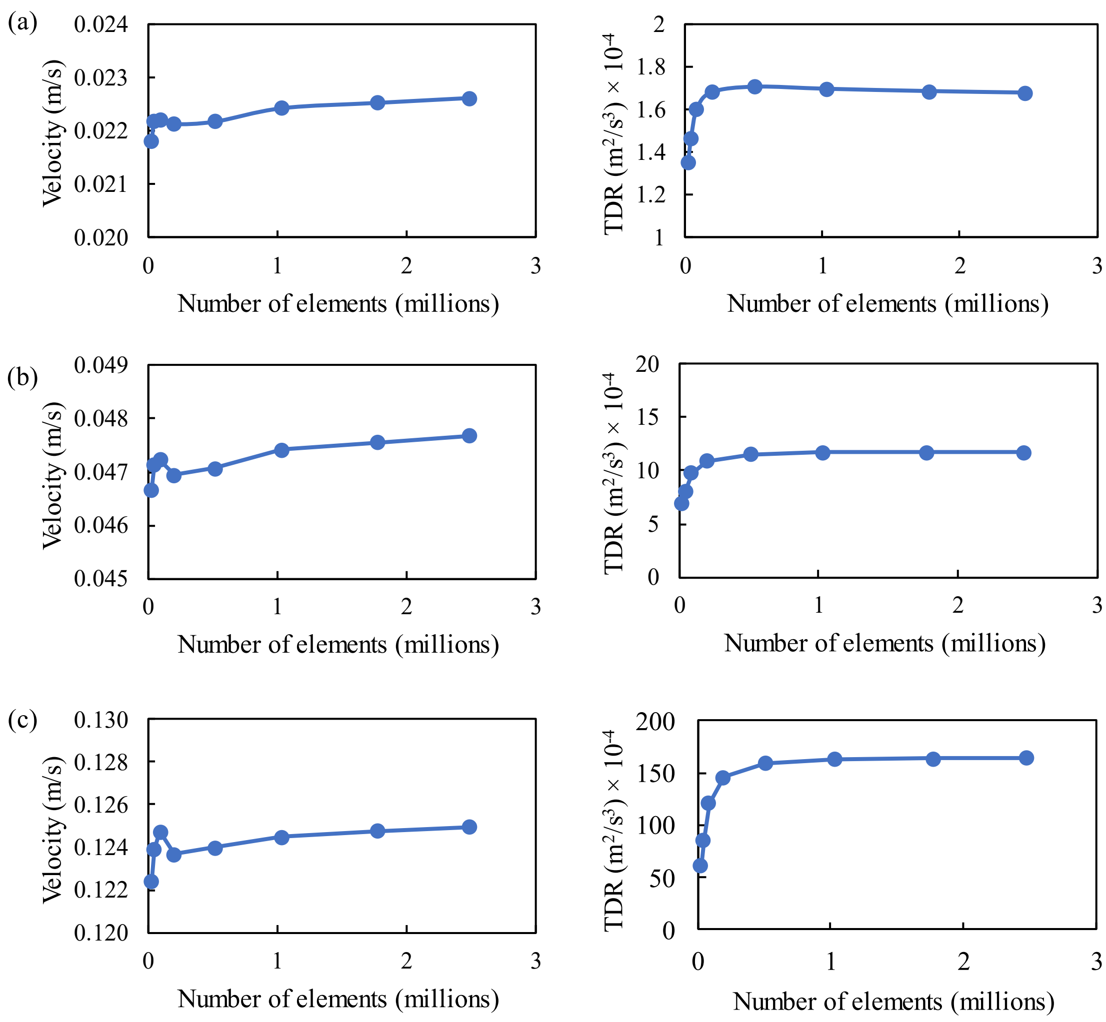

Figure 2.3. Average volumetric velocity magnitude and turbulent dissipation rate (TDR) mesh independence study for spinner flask model at (a) 30, (b) 60, and (c) 150 rpm.

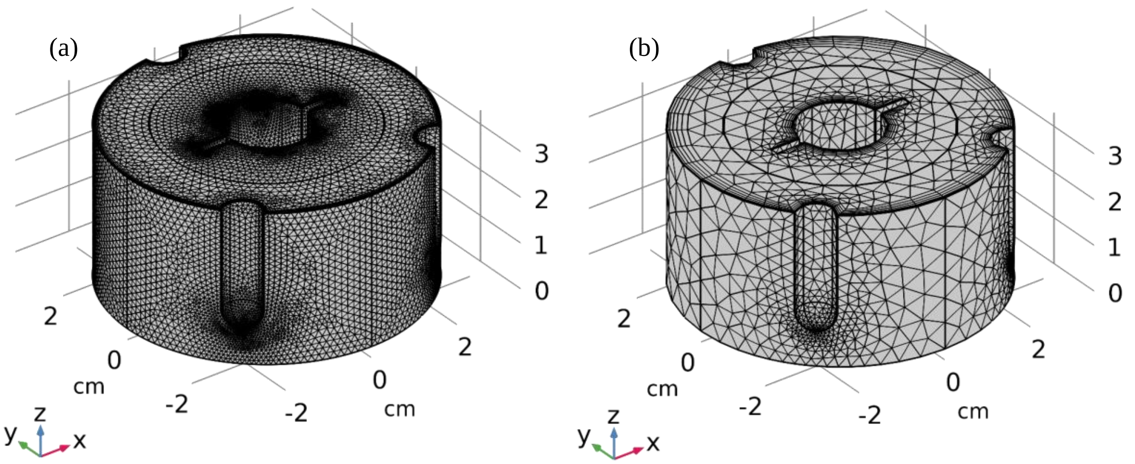

Figure 2.4. (a) Optimized and (b) coarse meshes used to generate data for ANN.

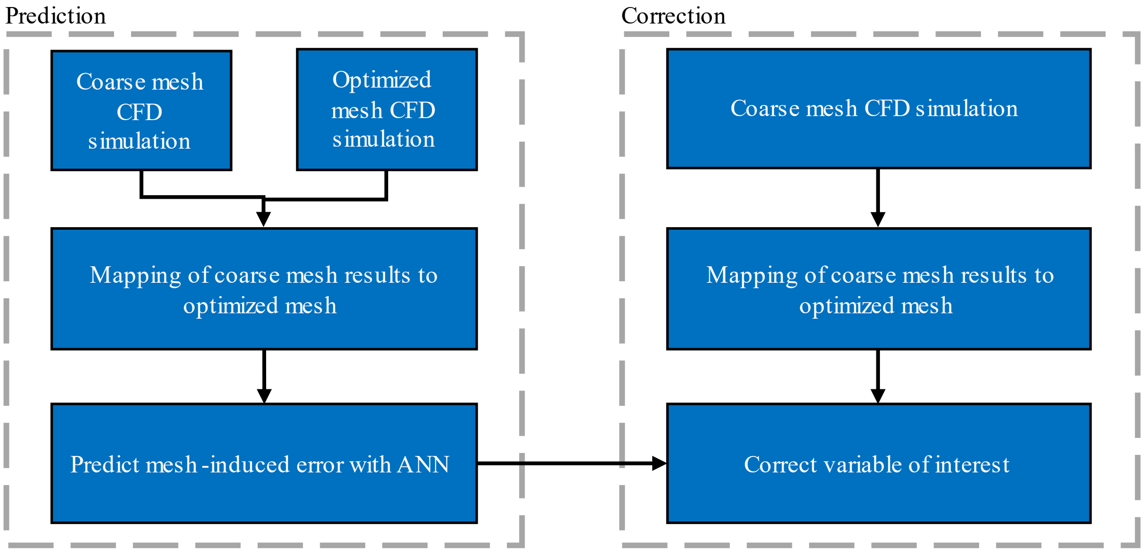

Figure 2.5. The workflow of ANN-based ML model to predict and correct errors in coarse mesh modeling results.

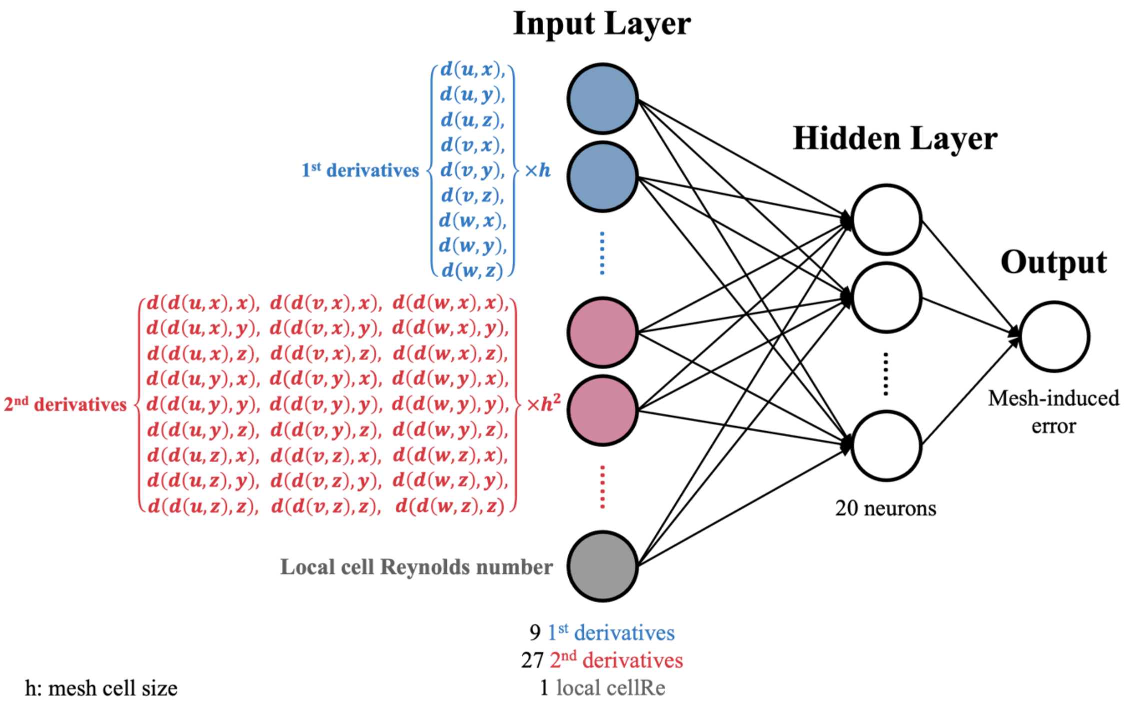

Figure 2.6. Schematic of the ANN baseline model with 37 inputs, 1 hidden layer (20 neurons), and 1 output.

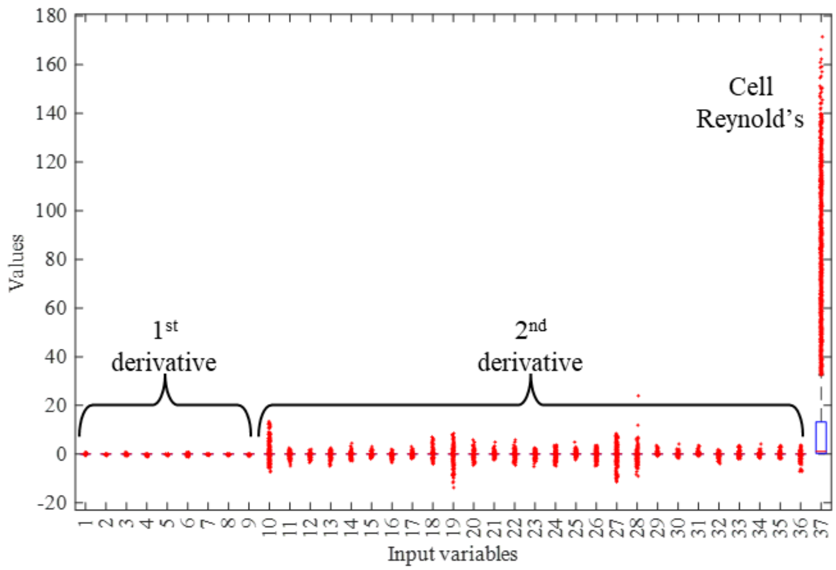

Figure 2.7. Boxplots of input variables used in the baseline ANN model before normalization.

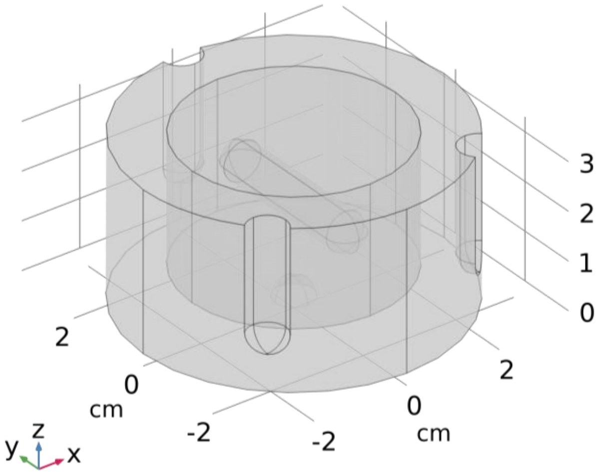

Figure 2.8. Simplified geometry used in the case study of different impeller geometry.

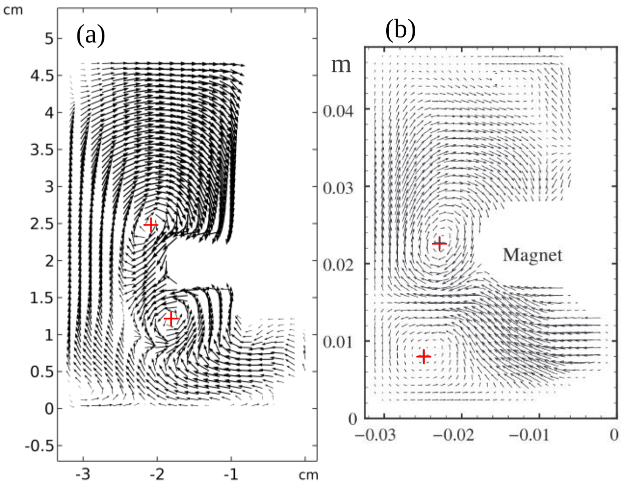

Figure 2.9. Comparison of (a) CFD flow profile to an (b) instantaneous velocity field captured with PIV by (Berry et al. 2016) for a rotational speed of 60 rpm for CFD modeling validation. Vortex centers highlighted with red cross.

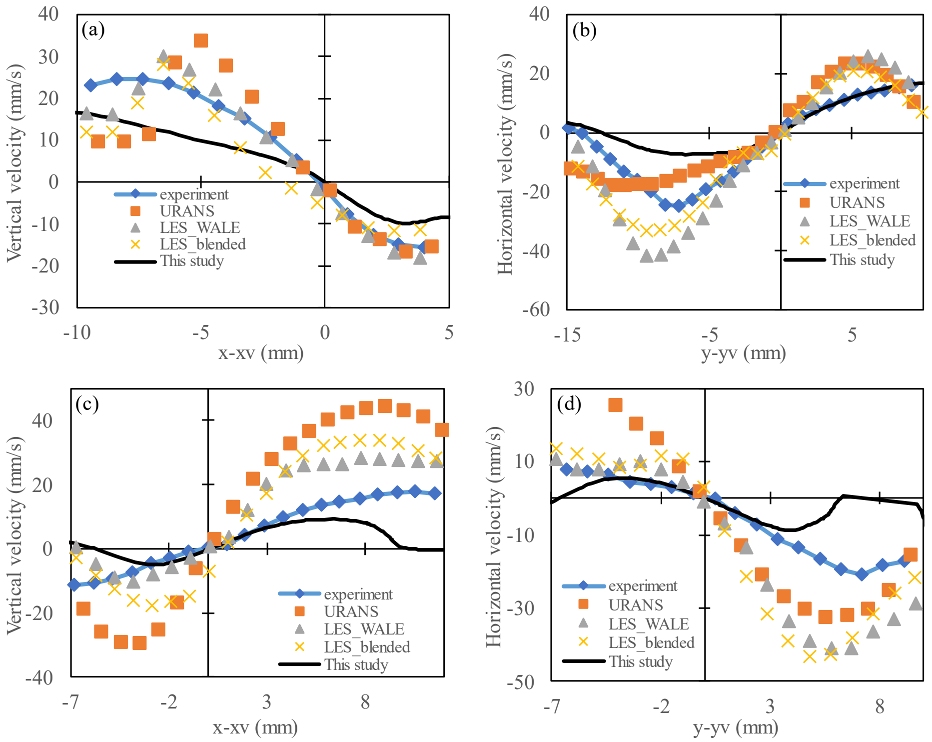

Figure 2.10. Comparison of this study against Berry et al. 2016 experimental PIV and CFD models values for the velocity components through the center of vortices. Top vortex (a) vertical-velocity on horizontal line and (b) horizontal-velocity on vertical line. Bottom vortex (c) vertical-velocity on horizontal line and (d) horizontal-velocity on vertical line.

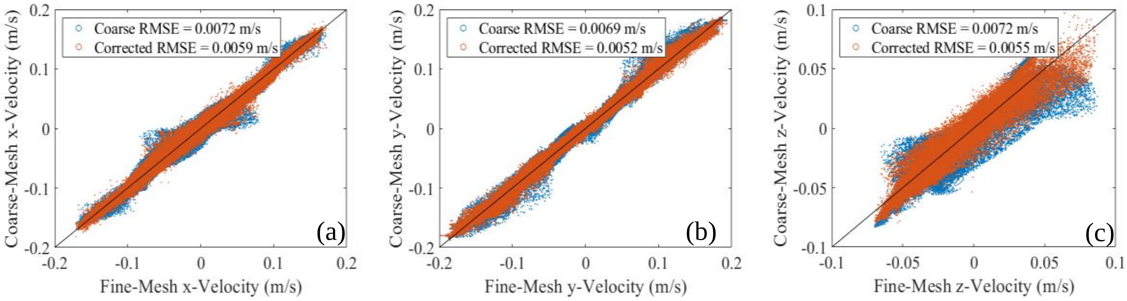

Figure 2.11. Correlation scatterplots between coarse and corrected velocity components against reference values from optimized mesh at 90 rpm using the baseline ANN model. (a) x, (b) y, and (c) z-direction velocity component.

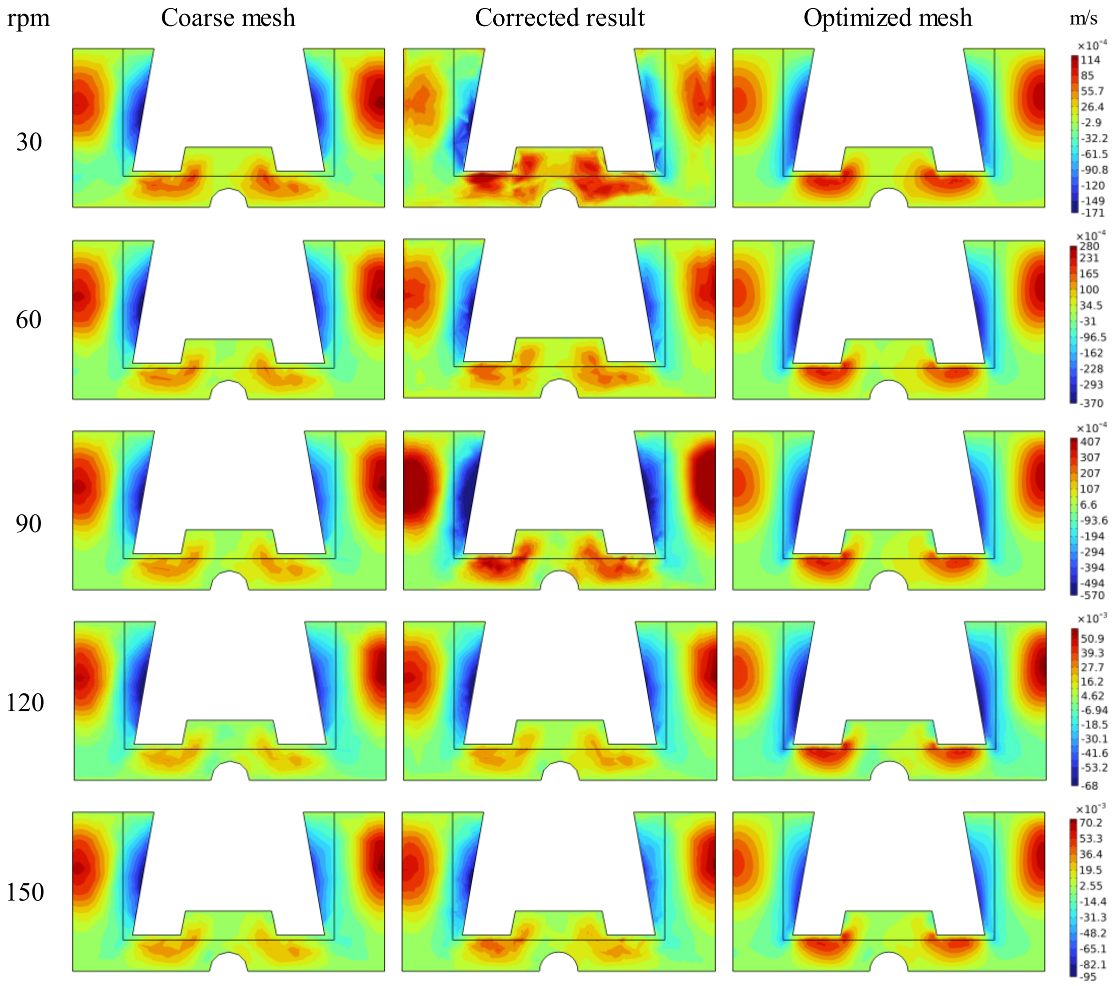

Figure 2.12. Surface plots of the coarse, corrected, and optimized z-velocity profiles at all five rotational speeds: 30, 60, 90, 120, and 150 rpm. Corrected z-velocity calculated with baseline model using 90 rpm as training. All results are shown in the xz-coordinate plane.

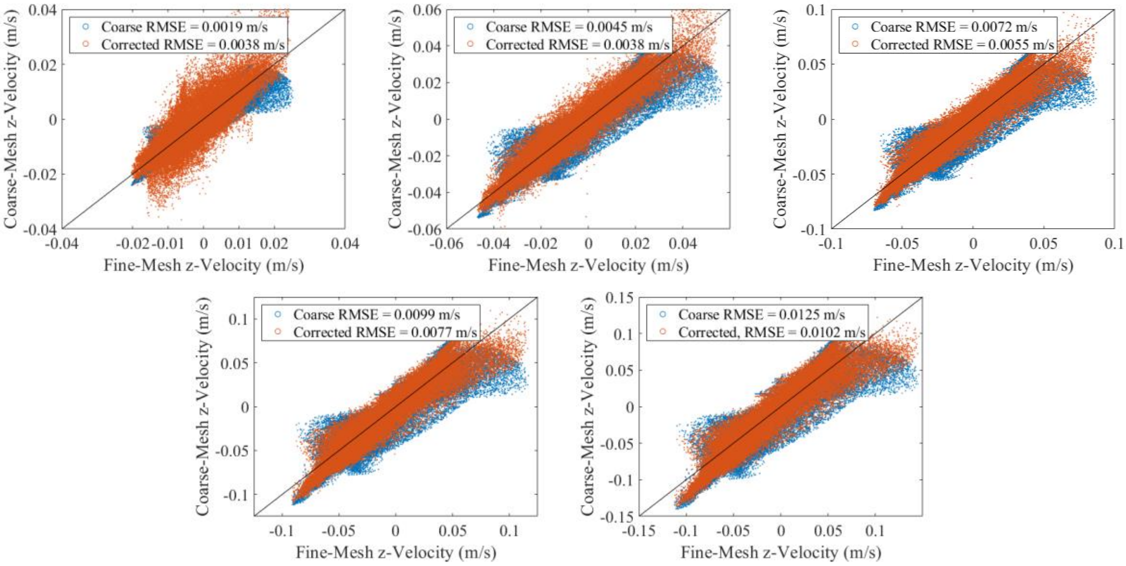

Figure 2.13. Correlation scatterplots between coarse and corrected z-velocity against reference z-velocity at (a) 30, (b) 60, (c) 90, (d) 120, and (e) 150 rpm using the baseline ANN model.

Table 2.1. Training and correction of z-velocity using ANN with varying number of neurons in a single hidden layer at 90 rpm.

# Neurons	Training Regression (R)	Training MSE (m^2/s^2)	Training time (hh:mm:ss)	Coarse RMSE (m/s)	Prediction RMSE (m/s)	ΔRMSE (%)
5	0.4725	3.96×10^{-5}	00:00:29	0.0072	0.0063	-12.42%
10	0.5578	3.55×10^{-5}	00:02:04	0.0072	0.0060	-17.36%
20	0.6529	2.94×10^{-5}	00:05:06	0.0072	0.0055	-24.32%
30	0.6991	2.62×10^{-5}	00:16:46	0.0072	0.0052	-28.55%
50	0.7561	2.20×10^{-5}	00:31:55	0.0072	0.0047	-34.58%
100	0.8079	1.76×10^{-5}	02:10:36	0.0072	0.0043	-40.48%

Table 2.2. Training and correction of z-velocity using ANN with varying number of hidden layers with 20 neurons each at 90 rpm.

Hidden layers	Training Regression (R)	Training MSE (m^2/s^2)	Training time (hh:mm:ss)	Coarse RMSE (m/s)	Prediction RMSE (m/s)	ΔRMSE (%)
1	0.6529	2.94×10^{-5}	00:05:06	0.0072	0.0055	-24.32%
2	0.7748	2.05×10^{-5}	00:06:43	0.0072	0.0046	-36.64%
3	0.8397	1.50×10^{-5}	00:15:14	0.0072	0.0039	-45.57%
4	0.8578	1.36×10^{-5}	00:20:22	0.0072	0.0037	-48.17%
5	0.8749	1.18×10^{-5}	00:24:26	0.0072	0.0035	-50.98%

Table 2.3. Training and correction of z-velocity using ANN with 100 neurons evenly distributed in varying number of hidden layers at 90 rpm.

# Neurons /layer	Training Regression (R)	Training MSE (m^2/s^2)	Training time (hh:mm:ss)	Coarse RMSE (m/s)	Prediction RMSE (m/s)	ΔRMSE (%)
[100]	0.8079	1.76×10^{-5}	02:10:36	0.0072	0.0043	-40.48%
[50 50]	0.7913	1.85×10^{-5}	01:26:36	0.0072	0.0044	-38.59%
[34 33 33]	0.8861	1.08×10^{-5}	01:08:36	0.0072	0.0034	-52.69%
[25 25 25 25]	0.8952	1.02×10^{-5}	01:17:53	0.0072	0.0033	-54.67%
[20 20 20 20 20]	0.8749	1.18×10^{-5}	00:24:26	0.0072	0.0035	-50.98%

Table 2.4. Training and correction of z-velocity using ANN model with varying normalization methods for the inputs.

Normalization	Correction rotational speed (rpm)	Coarse RMSE (m/s)	Prediction RMSE (m/s)	ΔRMSE %
None (Baseline)	30	0.0019	0.0038	98.90%
	60	0.0045	0.0038	-14.60%
	90	0.0072	0.0055	-24.13%
	120	0.0099	0.0077	-21.69%
	150	0.0125	0.0102	-18.37%
Scale all from -1 to 1 & CellRe from 0 to 1	30	0.0019	0.0038	101.34%
	60	0.0045	0.0038	-14.98%
	90	0.0072	0.0054	-24.98%
	120	0.0099	0.0076	-22.48%
	150	0.0125	0.0101	-19.04%
Scale 0 to 1	30	0.0019	0.0039	104.73%
	60	0.0045	0.0038	-15.72%
	90	0.0072	0.0053	-26.14%
	120	0.0099	0.0076	-23.42%
	150	0.0125	0.0100	-19.76%
Z-score	30	0.0019	0.0038	100.42%
	60	0.0045	0.0038	-14.78%
	90	0.0072	0.0054	-24.68%
	120	0.0099	0.0077	-22.26%
	150	0.0125	0.0101	-18.90%
Euclidean norm	30	0.0019	0.0038	100.42%
	60	0.0045	0.0038	-14.87%
	90	0.0072	0.0054	-24.61%
	120	0.0099	0.0077	-22.11%
	150	0.0125	0.0102	-18.71%

Table 2.5. Training and correction of z-velocity using ANN model with varying training datasets of rotational speeds

Training rotational speed (rpm)	Correction rotational speed (rpm)	Coarse RMSE (m/s)	Prediction RMSE (m/s)	ΔRMSE (%)
30	30	0.0019	0.0012	-37.68%
	60	0.0045	0.0036	-20.81%
	90	0.0072	0.0063	-13.26%
	120	0.0099	0.0089	-9.62%
	150	0.0125	0.0116	-7.45%
60	30	0.0019	0.0022	18.66%
	60	0.0045	0.0033	-26.00%
	90	0.0072	0.0057	-21.08%
	120	0.0099	0.0083	-16.29%
	150	0.0125	0.0109	-12.92%
90 (baseline)	30	0.0019	0.0038	98.90%
	60	0.0045	0.0038	-14.60%
	90	0.0072	0.0055	-24.13%
	120	0.0099	0.0077	-21.69%
	150	0.0125	0.0102	-18.37%
120	30	0.0019	0.0055	188.46%
	60	0.0045	0.0049	9.90%
	90	0.0072	0.0057	-20.63%
	120	0.0099	0.0075	-24.39%
	150	0.0125	0.0097	-22.70%
150	30	0.0019	0.0069	265.72%
	60	0.0045	0.0063	39.54%
	90	0.0072	0.0066	-8.76%
	120	0.0099	0.0078	-20.69%
	150	0.0125	0.0097	-22.56%

Table 2.5. Continued

Training rotational speed (rpm)	Correction rotational speed (rpm)	Coarse RMSE (m/s)	Prediction RMSE (m/s)	ΔRMSE (%)
30 & 60	30	0.0019	0.0021	13.49%
	60	0.0045	0.0033	-27.00%
	90	0.0072	0.0057	-21.22%
	120	0.0099	0.0083	-16.26%
	150	0.0125	0.0109	-12.84%
120 & 150	30	0.0019	0.0069	265.78%
	60	0.0045	0.0062	37.58%
	90	0.0072	0.0064	-11.11%
	120	0.0099	0.0076	-22.66%
	150	0.0125	0.0095	-24.05%
30 & 150	30	0.0019	0.0071	274.91%
	60	0.0045	0.0063	40.64%
	90	0.0072	0.0065	-10.25%
	120	0.0099	0.0076	-22.89%
	150	0.0125	0.0094	-24.75%
60 & 120	30	0.0019	0.0051	171.97%
	60	0.0045	0.0047	4.39%
	90	0.0072	0.0056	-22.28%
	120	0.0099	0.0074	-24.56%
	150	0.0125	0.0097	-22.35%
30, 90 & 150	30	0.0019	0.0067	252.91%
	60	0.0045	0.0060	32.63%
	90	0.0072	0.0063	-12.88%
	120	0.0099	0.0076	-22.95%
	150	0.0125	0.0095	-23.73%

Table 2.6. Mesh error correction of Kolmogorov length at varying mixing speeds with baseline ANN trained with 90 rpm.

Correction rotational speed (rpm)	Coarse RMSE (mm)	Prediction RMSE (mm)	ΔRMSE (%)
30	0.0182	0.0149	-18.34%
60	0.0181	0.0096	-47.07%
90	0.0174	0.0079	-54.37%
120	0.0165	0.0073	-55.97%
150	0.0157	0.0070	-55.03%

Table 2.7. Correction performance of ANN model predicting fluid z-velocity and Kolmogorov length generated by varying viscosity of bulk liquid at 90 rpm.

Corrected Parameter	Training viscosity (mPa·s)	Prediction viscosity (mPa·s)	Coarse RMSE	Prediction RMSE	ΔRMSE (%)
z-velocity (m/s)	1	0.5	0.0076	0.0060	-21.18%
		1	0.0072	0.0055	-24.13%
		2	0.0063	0.0048	-23.60%
Kolmogorov length (mm)	1	0.5	0.0148	0.0070	-52.99%
		1	0.0174	0.0079	-54.37%
		2	0.0182	0.0112	-38.24%

Table 2.8. Prediction performance of ANN trained with original geometry and predicting/correcting the simplified geometry.

Corrected Parameter	Training rpm	Prediction rpm	Coarse RMSE	Prediction RMSE	% ΔRMSE
z-velocity (m/s)	90	30	0.0005	0.0026	382.73%
		60	0.0016	0.0031	90.85%
		90	0.0030	0.0041	35.71%
		120	0.0045	0.0054	18.94%
		150	0.0060	0.0067	11.75%
Kolmogorov length (mm)	90	30	0.0488	0.0421	-13.67%
		60	0.0526	0.0461	-12.29%
		90	0.0517	0.0451	-12.67%
		120	0.0501	0.0434	-13.44%
		150	0.0488	0.0419	-14.20%

3. CHAPTER III.

A 3D CNN MODEL FOR CORRECTION OF COARSE MESH CFD MODELS OF CELL CULTURE BIOREACTORS

Abstract

Computational Fluid Dynamics (CFD) is a valuable tool for studying fluid environments within cell culture bioreactors and optimizing processing parameters, but it can be computationally expensive. This study developed a three-dimensional (3D) Convolutional Neural Network (CNN) machine learning model to improve the CFD model efficiency by predicting high-resolution fluid profiles of a spinner flask bioreactor from a low-resolution counterpart. The CNN model was initially trained to predict shear stress profiles with an average improvement of the coarse profile of 67% with optimized number of residual blocks, filters, and batch size. The optimization process showed that a deeper network did not generate better results and that a smaller batch size and fewer filters increased generalization and decreased computational resources needed to train and use the trained model. The optimized model was also able to predict Kolmogorov length with average improvement on the low-resolution profile of 30% and z-velocity component with an improvement of 6%. The model's generalization capabilities were further evaluated by predicting shear stress and Kolmogorov length across bioreactors with three different impeller geometries. Results suggested that the model was able to properly generalize for Kolmogorov length but not shear stress when trained with data from a single impeller geometry. When using data from all impeller geometries for training, the model was able to properly generalize across all evaluated scenarios with an average improvement on coarse profile of 57%. With some modifications, this model's prediction speed may also be useful to develop real-time feedback loops between a real bioreactor to calculate the desired processing parameters, modify the corresponding controls, and therefore establish a digital twin system.

Keywords: Machine learning, mesh resolution, Kolmogorov length, shear stress, spinner flask, cell culture

1 Introduction

Computational fluid dynamics (CFD) models have been used to generate reliable high-resolution data and avoid incurring high experimental costs. They have proven useful to characterize the fluid profiles of many biomanufacturing processes such as bacterial fermentation (Spann et al. 2019), monoclonal antibody production (Mishra et al. 2021), and recombinant protein production (Han et al. 2022). Recently, CFD models have been used to understand the hydrodynamics inside animal cell culture bioreactors and optimize their processing parameters. Many of the CFD studies have focused on stirred tank bioreactors, since they are the most commonly used, to predict the turbulent energy dissipation rates and mass transfer of oxygen (Ghasemian et al. 2020; Ramírez et al. 2020; Zhang et al. 2021). Other models have been used to improve impeller or vessel design to improve overall conditions for cell culture (Bliatsiou et al. 2019; Ueki et al. 2021). Furthermore, these CFD models have been used to help with scaling up production to industrial volumes (~100 m^3) and meet expected consumer demands in the near future (Villiger et al. 2018; Scully et al. 2020; Seidel et al. 2023). In this study, we focused mainly on shear stress and Kolmogorov length due to their relevance to animal cell cultures and the negative impacts this variable may have on final yields if not properly monitored and controlled (Cherry and Kwon 1990; Choi et al. 2017; Alfieri et al. 2019; ‘t Hart et al. 2021).

Although these models provide high-resolution data with considerably less experimental costs, they still have limitations of their own such as high computational cost, long time for simulation, and require extensive knowledge of the underlying physics to simulate properly (Ferziger and Perić 2002). At smaller scales, a simple mesh refinement process can be used to increase the accuracy of the models. However, at industrial scale, such methods can take up to days to generate results with the same level of resolution and become more computationally expensive leading to a trade between quality and speed of results (Panchigar et al. 2022). Because of these limitations, multiple modeling assumptions are made, and meshing resolution is sacrificed for faster simulation results. Ideally, the high-resolution flow data could be generated quickly enough that any modifications to the processing parameters of bioreactors can be adjusted in real-time. It becomes essential to develop a time-efficient way to obtain high-resolution CFD results without sacrificing accuracy.

Recent advances in machine learning (ML) methods offer a promising solution to generate high-resolution flow fields quickly without needing to solve computationally intensive CFD models for every new condition. Several ML algorithms and techniques have been implemented to reduce computational time while retaining accuracy (Kochkov et al. 2021; Hammond et al. 2022; Vinuesa and Brunton 2022; Panchigar et al. 2022). One method to reduce computational time is to simulate CFD model using low-resolution mesh and then train a ML model to correct the coarse-mesh-induced error and obtain more accurate results at high-resolution mesh. Promising results where obtained in predicting the cut-off diameter of cyclone separators using coarse-grid CFD simulations and training an Artificial Neural Network (ANN) to correct the mesh-induced errors (Le et al. 2023). Hanna et al. (2020) trained an Artificial Neural Network (ANN) model to predict and correct local turbulent flow errors of a lid-driven cavity at different Reynolds numbers. A similar ANN model was developed to correct coarse-mesh-induced errors in 3D CFD models of a cell culture bioreactor (Cantarero-Rivera et al. 2024). However, the ANN-based ML models had limited generalization capabilities where good correction capability was only observed at similar training and prediction conditions. Another significant limitation of the ANN-corrected CFD results did not show smooth gradient between adjacent meshing nodes, which was because the ANN model applied error corrections on each individual node without considering the gradients of adjacent nodal points (Cantarero-Rivera et al. 2024).

Built upon the basic ANN principle, Convolutional Neural Network (CNN)-based ML learning models that process grid-like data could address the limitations of ANN. CNN models have been widely used in image processing, which always process the adjacent image pixels together (Dong et al. 2016; Fukami et al. 2019). The first application of a CNN for super-resolution was proposed as a method to learn the end-to-end mapping from input to output data without the need of such deep networks leading to reduced computational times while retaining quality (Dong et al. 2016). Similar to processing images, CNN models have been used in processing CFD modeling results of flow profiles, specifically to reconstruct turbulent flows in theoretical conditions in two dimensions (Jin et al. 2018; Fukami et al. 2019) and more recently in three dimensions

(Zhou et al. 2022). In these studies, the models are trained to learn the direct mapping from the low to the high-resolution datasets. Their results showed the capability of CNN models in predicting high-resolution laminar and turbulent flow fields from low-resolution data. However, these CNN models only used the sliced 2D CFD results to generate CFD results at high resolutions. Zhou et al. (2022) developed a turbulence volumetric super-resolution (TVSR) model using CNN to reconstruct 3D homogeneous isotropic turbulence. The TVSR model was trained using 3-D data from two low Reynold's scenarios and found accurate results in predicting the high-resolution flow fields of scenarios with higher Reynolds numbers. However, the model's generalization capabilities where limited to this single test and not explored in depth and also not applied to real-world scenarios.

All the CNN models mentioned previously show promising results; however, their structures are all different as some include some layers and skip connections that others do not. Some popular models for their novel structures and hyperparameters include AlexNet, for introducing the Rectified Linear Unit (ReLU) activation functions (Krizhevsky et al. 2017), GoogLeNet, for eliminating the need for fully connected layers within the structure (Szegedy et al. 2015), and ResNet for introducing the concept of residual blocks (He et al. 2016). The TVSR model developed by Zhou et al. (2022) used this residual block structure to extract the features and pass down information from previous layers before using deconvolution layers to up-sample the results to match the original's data dimensions. Another structure that has shown great results for turbulent flow reconstructions is the U-net structure, which was first introduced for biomedical image segmentation (Ronneberger et al. 2015; Çiçek et al. 2016; Mehta and Arbel 2019) and has also been used in CFD models to mimic classical multigrid solvers (Ajuria Illarramendi et al. 2023). Thuerey et al. (2020) used a CNN U-Net to predict the high-resolution pressure and velocity distributions around two-dimensional airfoils with varying shapes with an error of less than 3% with their best models. The U-Net structure consists of a down-sampling or encoder section followed by an up-sampling or decoder section. The U-Net architecture translates spatial information into extracted features via convolutional layers, and uses skip-connections between encoder and decoder layers to ensure the availability of as much input information in the output layers for solution inference (Thuerey et al. 2020). This architecture has been modified for super-resolution tasks by removing batch normalization layers and one convolution layer in each block, reducing computational cost while maintaining reconstruction performance (Lu and Chen 2022). The U-Net's encoding part progressively down-samples the image size, allowing for the extraction of increasingly abstract information, while the decoding part increases spatial resolution and reduces the number of feature layers. The skip connections concatenate all channels from the encoding branch to the corresponding branch of the decoding part, effectively doubling the number of channels for each decoding block. These modifications have resulted in superior performance and time consumption compared to existing super-resolution algorithms (Thuerey et al. 2020).

The overall goal of this study is to use a CNN-based U-Net model using coarse and fine mesh CFD simulations of a spinner flask to reconstruct the flow profile within at different mixing conditions, i.e., varying mixing speeds and cell culture viscosities. The CNN was chosen due to its ability to handle high dimensional data and learn the mapping function directly from the input data provided (Fukami et al. 2019). Inspired by the 3D CNN model developed by Zhou et al. (2022) and the promising results of the U-Net developed by Thuerey et al. (2020), we propose to develop a 3D CNN U-Net model that could use low-resolution modeling results to generates high-resolution fluid profiles with improved modeling accuracy and good generalization. The objectives of this study are to:

(1) Develop a 3D CNN U-Net model and optimize its structure and hyperparameters to predict high-resolution shear stress profiles from low-resolution input data.

(2) Compare 3D CNN U-Net model performance to previously developed ANN model in terms of prediction accuracy and computational requirements.

(3) Test the generalization capabilities of the trained 3D CNN U-Net model when predicting shear stress and Kolmogorov length flow profiles in cell culture bioreactors with different impeller geometries.

2 Materials and method

2.1 CFD models development and validation

The Corning® Series 4500–125 spinner flask (Corning, NY) with a working volume of 100 mL was modelled in COMSOL Multiphysics® 6.1 (COMSOL Inc., Burlington, MA). The base geometry with exact measurements used for this coupled approach was built and validated in previous experiments and models (Cantarero-Rivera et al. 2024) (**Figure 3.1**a). The geometry was discretized into two separate meshes to generate the low and high-resolution CFD results. The coarse mesh consisted of 44,497 elements (**Figure 3.1**b) while the high-resolution data was obtained by solving the models with a fine mesh with 1.03 million elements (**Figure 3.1**c). The decision to use these different meshes was based on a mesh refinement study performed in the previous study (Cantarero-Rivera et al. 2024).

All simulations assumed steady state and used the Reynolds averaged Navier-Stokes (RANS) κ-ε turbulence model to describe the incompressible fluid profile. The RANS equations are expressed as:

$$\rho \boldsymbol{u} \cdot \nabla \boldsymbol{u} = -P\nabla + (\mu + \mu_t)\nabla^2 \boldsymbol{u} \qquad \textbf{(3.1)}$$

$$\rho \nabla \cdot \boldsymbol{u} = 0 \qquad \textbf{(3.2)}$$

where ρ is the density, $\boldsymbol{u}$ is the velocity magnitude, P is the pressure, μ is the dynamic viscosity, and μ_t is the eddy viscosity, also known as the turbulent viscosity. The turbulent viscosity modeled as:

$$\mu_t = \rho C_\mu \frac{k^2}{\varepsilon} \qquad \textbf{(3.3)}$$

where $C\mu$ is one of the five turbulence constants, k is the turbulent kinetic energy, and ε is the turbulent dissipation rate. The transport equation for k is:

$$\rho \boldsymbol{u} \cdot \nabla k = \nabla \cdot \left(\left(\mu + \frac{\mu_t}{\sigma_k} \right) \nabla k \right) + P_k - \rho \varepsilon \qquad \textbf{(3.4)}$$

and the transport equation for ε is:

$$\rho \boldsymbol{u} \cdot \nabla \varepsilon = \nabla \cdot \left(\left(\mu + \frac{\mu_t}{\sigma_\varepsilon} \right) \nabla \varepsilon \right) + C_{\varepsilon 1} \frac{\varepsilon}{k} P_k - C_{\varepsilon 2} \rho \frac{\varepsilon^2}{k} \qquad \textbf{(3.5)}$$

where σ_k and σ_ε are the turbulent Prandtl numbers for k and ε, respectively, and P_k is the production term expressed as:

$$P_k = \mu_t \left(\nabla \boldsymbol{u} \colon (\nabla \boldsymbol{u} + (\nabla \boldsymbol{u})^T) - \frac{2}{3} (\nabla \cdot \boldsymbol{u})^{\mathbf{2}} \right) - \frac{2}{3} \rho k \nabla \cdot \boldsymbol{u} \qquad \textbf{(3.6)}$$

This turbulence model uses five turbulence constants $C_\mu = 0.09$, $C_{\varepsilon 1} = 1.44$, $C_{\varepsilon 2} = 1.92$, $\sigma_k = 1$, and $\sigma_\varepsilon = 1.3$ previously determined experimentally in simple flows (Launder and Spalding 1974; Wilcox 2006). The COMSOL κ-ε turbulence model has been widely used for suspension bioreactors (Borys et al. 2019; Freiberger et al. 2022) and has been validated for spinner flasks through light attenuation (Delafosse et al. 2018) and particle image velocimetry (Berry et al. 2016).

2.2 Machine learning model

2.2.1 3D CNN U-Net model base structure

The base structure for our proposed model was inspired on the TVSR model developed by Zhou et al. (2022). The model consists of using a combination of residual blocks for feature extraction and upscale modules to generate the high-resolution fluid profiles from the low-resolution inputs. The residual blocks consist of two convolution layers, a ReLU activation layer, and a short skip connection between the input of the first convolution layer and the output of the second combined in an addition layer at the end of the residual block. The upscale modules consist of a convolution layer followed by a deconvolution (also called transposed convolution) layer. The model also uses a long skip connection between the output of the first convolution layer to the output of the last residual block to avoid the gradient vanishing and exploding problems in deep networks (Zhou et al. 2022). The reported TVSR model has 8 residual blocks with a batch size of 16 and 128 filters at every convolutional layer with sizes of 3x3x3 since it was common practice on previous studies (Tai et al. 2017; Liu et al. 2020; Zhou et al. 2022)

The base structure from Zhou et al. (2022) was modified from a straight residual block network to a U-Net structure by matching the number of residual and upscale blocks and adding a skip connection between them essentially separating the model into an encoder-decoder structure (**Figure 3.2**). These skip connections help the network by using the outputs of previous layers at later stages; therefore, any information lost from the filters of the convolution layers of the residual blocks or the encoder part is recovered (Thuerey et al. 2020).

2.2.2 Training 3D CNN U-Net model

A large training dataset is typically required to create a robust model. Since the objective of the study was to improve computational models of cell culture bioreactors, fluid flows with combinations of mixing speeds from 30 – 300 rpm and viscosities from 0.75 – 1.5 mPa·s were used in CFD models. However, instead of modelling all possible combinations, the Latin Hypercube method (Mckay et al. 2000; Kiener et al. 2023) was used to generate 50 different simulations (**Figure 3.3**) that would be statistically representative of both ranges. This method uses a specified range for at least two parameters, a defined amount of points desired, and considers the position of previously chosen points to prevent similar points from being chosen (Li and Yang 2023). This provided a dataset with points that are fully turbulent and some in the transition region. In contrast to previous super-resolution studies that generated the low-resolution data by applying filters to the high-resolution data (Liu et al. 2020; Zhou et al. 2022), the model in this study was solved using two meshes with different refinement levels. As mentioned previously, the low-resolution data was solved using a coarse mesh consisting of 44,497 elements (**Figure 3.1**b) while the high-resolution data was obtained by solving the models with a fine mesh with 1.03 million elements (**Figure 3.1**c).

To train the CNN model that correlate the low-resolution and high-resolution CFD results, the low-resolution flow profiles for the variable of interest, either shear stress, Kolmogorov length, or velocity components (*u, v, w*), were used as training inputs and their high-resolution counterparts were used as training outputs (**Figure 3.2**). Separate models were trained for each variable of shear stress, Kolmogorov length, or velocity components. All 50 simulations were randomly split into 80% (40) for training, 10% (5) for validation and the remaining 10% (5) for further evaluation (**Figure 3.3**). During the training process, the model used the ADAptive Moment estimation (ADAM) stochastic solver which uses a moving average to update the network parameters (Kandel and Castelli 2020). Using the moving average allows parameter updates to adapt to noisy gradients. It also includes a mechanism to attempt to correct the bias that typically appears at the beginning of training (Mustapha et al. 2021).

2.3 Optimizing 3D CNN U-Net structure and hyperparameters

The model structure and hyperparameters were optimized to enhance the prediction of high-resolution shear stress profiles from coarse mesh CFD data. There are many hyperparameters that can be optimized in a CNN model such as learning rate, batch sizes, number of filters, among others. In this study, optimization of number of filters, number of residual blocks, and batch size was carried out to determine the settings that would provide the model with the prediction performance during training with the shortest computational time and memory requirements as well. The performance of the proposed model is evaluated during the training process using the training and validation RMSE values between predicted and high-resolution flow profiles as the network’s weights and biases are updated instead of the typical loss function, mean squared error. The idea behind this being that RMSE will have the same units as the variable of interest and its physical meaning is easier to interpret and compare to the absolute values of the variable of interest. The training RMSE is indicative of how well the model fitted the provided training datasets with their high-resolution counterparts. On the other hand, the validation RMSE is indicative of the model’s performance when predicting a new dataset different from training and lower values indicate better performance.

2.4 Evaluation of 3D CNN U-Net flow profile reconstruction capabilities compared to ANN approach

The prediction performance of the optimized 3D CNN U-Net model was then compared against our previously reported ANN-based mesh error correction method (Cantarero-Rivera et al. 2024). This previous method is trained to learn the mesh error between the coarse and fine mesh CFD modeling results at specific mixing speeds. The trained model is then used to predict the mesh-induced error of a test coarse dataset. This predicted error is added to the coarse flow profile to generate the high-resolution profile with fine meshes. In this case, the model was trained with CFD results for 4 mixing speeds 30, 60, 90, and 150 rpm. The 3D CNN U-Net model, on the other hand, is trained to correlate the high and low-resolution flow profiles and is used to predict a high-resolution profile from a test coarse dataset directly. The trained models were then used to predict the flow profiles of five mixing speeds: 30, 60, 90, 120, and 150 rpm. Viscosity and density of the bulk fluid were kept constant at 1 mPa·s and 1000 kg/m^3, respectively. All governing equations and boundary conditions in the simulations were kept the same The coarse input data for the ANN model would originally be mapped to the fine mesh coordinates (Cantarero-Rivera et al. 2024); however, to ensure proper comparison between the models, this mapping procedure was modified to match the 100×100×100 mapping employed and required by the 3D CNN U-Net model.

Qualitative comparison of the predicted, low-resolution, and high-resolution flow profiles for shear stress, Kolmogorov, and velocity components was done through surface plots at cross-planes between all three-dimensional axes. Quantitatively, the low-resolution and predicted flow profiles were compared against the high-resolution data by the RMSE; calculated as:

$$RMSE_{predicted} = \sqrt{\frac{1}{n}\sum_{i=1}^{n} |Predicted_i - HighResolution_i|^2} \qquad \textbf{(3.7)}$$

where *n* is the number of meshing nodes, $Predicted_i$, *and* $HighResolution_i$ are the predicted and high-resolution modeling results ($Predicted_i$ can be replaced by Low_I to calculate the RMSE for low-resolution profile). The percentage change of the RMSE value change from the low-resolution model results to the predicted was calculated as follows:

$$\Delta RMSE\ \% = \frac{RMSE_{predicted} - RMSE_{low}}{RMSE_{low}} \times 100 \qquad \textbf{(3.8)}$$

Lower RMSE values indicate that the model results match better with the high-resolution results. A negative number in the percentage change indicates an improvement in variable prediction.

2.5 Testing generalization of the trained 3D CNN U-Net model to predict flow profiles in bioreactors with different impeller geometries

To further evaluate the generalization capabilities of the proposed 3D CNN U-Net model, the flow profiles of cell culture bioreactors with two other impeller geometries were considered; a simple rod impeller, similar to a magnetic stir bar, and a Rushton impeller, which is typically observed in large scale bioreactors (Joshi et al. 2011) (**Figure 3.4**). All impellers were designed to have the same diameter to ensure the size of the rotating domain remained the same regardless of impeller geometry. The optimized 3D CNN U-Net trained with the original paddle impeller geometry data was used to predict the shear stress, Kolmogorov length, and velocity component profiles from the other two geometries. Qualitative and quantitative comparisons were carried out in the same manner as the previous section.

3 Results and discussion

3.1 Optimizing CNN structure and hyperparameters

The model structure and hyperparameters were optimized to enhance the prediction of high-resolution shear stress profiles from coarse mesh CFD data. The first setting optimized was the number of residual blocks. The residual blocks are used to extract the features of the original dataset and help the model learn from these features (He et al. 2016). A deeper network with more residual blocks would extract more features and learn more from the input dataset but runs the risk of overfitting and therefore would struggle to properly predict datasets not used in training (Kim et al. 2016). Skip connections were added as required between the newly added residual and upscale blocks. No other settings were changed during this optimization process.

The effect of changing the number of residual and upscale blocks on training and validation RMSE is shown in **Figure 3.5**. The curves showing RMSE during training epochs indicate consistent performance across all models regardless of number of blocks due to the noise present in all (**Figure 3.5**a). On the other hand, the model with only 8 blocks consistently had lower validation RMSE values than the others during training (**Figure 3.5**b). At the last iteration of training, the lowest training RMSE was obtained by the model with 4 blocks while the lowest validation RMSE was obtained by the model with 8 blocks (**Figure 3.5**c). These results are contrary to those found when employing ResNet for computer vision problems where deeper networks resulted in better performance (Kim et al. 2016; Lim et al. 2017; Tai et al. 2017). However, Dong et al. (2016) found a trend where increasing the depth of the network did not necessarily improve the performance similar to the results presented in this study. When applying to turbulence reconstruction, Zhou et al. (2022) compared models with 2, 4, and 8 residual blocks and found that the best results were obtained using 8 residual blocks.

Furthermore, as more layers were added, the memory requirements increased and therefore the training time also increased. Training time increased from 226 CPU (core) hours for the model with 4 blocks to 469 CPU hours for 8 blocks and up to 831 CPU hours for 16 blocks. CPU hours were calculated as the product of total time required for training times the number of cores available in the computer running the algorithm. Considering both validation RMSE and computational time, the model with 8 blocks was chosen as the best of the explored options.

The number of filters in all convolutional layers was optimized after optimizing the number of residual blocks. Using filters with larger dimensions and more of them would allow for expanded range of feature extraction from the data; however, computational costs increase correspondingly (Liu et al. 2020; Zhou et al. 2022). The effect of changing the number of filters in each convolution layer, while maintaining their size constant, is shown in **Figure 3.6**. Once more, the training RMSE curves indicate consistent performance across all models regardless of number of filters due to the noise present in all (**Figure 3.6**a). Using 128 and 64 filters had similar validation RMSE as the training progressed while using 32 filters was consistently higher than the others (**Figure 3.6**b).

At the last iteration of training, the lowest training RMSE was obtained by the model with 32 filters while the lowest validation RMSE was obtained by the model with 128 filters (**Figure 3.6**c). Although a lower validation RMSE is desirable since it is an indicator of the model's generalization ability, training time decreased from 105 hours with 128 filters to 48 hours with 64 filters to 29 hours with 32 filters. Based on this, the number of filters used for our proposed 3D CNN U-Net was set to 32 at every convolution layer to have the fastest training time.

Once the best number of residual and corresponding upscale blocks was identified, and optimal number of filters determined, the batch size was then optimized. All previous optimization results used a batch size of 16. The batch size determines the subset of the training data that is used to evaluate the loss function and update the weights within the network (Kandel and Castelli 2020). Using a larger batch size allows for more training data to be processed at once leading to a possible reduction in total training time. However, models tend to lose generalization ability as the batch size increases, leading to the "generalization gap" problem (Hoffer et al. 2017; Chen et al. 2018; Oyedotun et al. 2023).

The training and validation RMSE results are shown in **Figure 3.7**. Results indicate that decreasing batch size reduced both training and validation RMSE values and reached convergence much faster than when larger batch sizes were used. Kandel and Castelli (2020) developed a CNN model to classify medical images and found similar results where the model with the smallest batch size had the best performance when using a learning rate of 0.0001 which is the same used in our proposed model. Zhou et al. (2022) also found similar results where the best results were generated by the model with the smallest batch size. All models had similar total training times; however, the memory requirements decreased from ~150 GB for batch size of 16 to ~35 GB for batch size of 2. This is because fewer datasets are being processed through the model in every iteration, allowing the model to be run on computers with less memory. Considering computational expenses and validation RMSE values, which is a direct representation of generalization, a batch size of 2 was considered the best of the explored options to use in our model.

The optimized structure of the proposed 3D CNN U-Net model to predict high-resolution shear stress profiles is shown in Table 1. Compared against the settings used for the TVSR model (Zhou et al. 2022), the 3D CNN U-Net model used a reduced number of filters as it did not show a significant impact on training or validation RMSE but reduced training time significantly. It should be noted that the TVSR model uses a patch-wise preprocessing of the training data to separate each training dataset into smaller sections that are processed at a time. This is different from the batch size and is used to enhance the learning of the relationship between neighboring points. This adds more complexity to the model requiring more computational power and was therefore not explored in this study. Furthermore, the 3D CNN U-Net reduced the batch size from 16 to 2 since it showed better training and validation RMSE values and also required less memory allowing for easier use of the proposed model.

3.2 Evaluation of 3D CNN U-Net flow profile reconstruction capabilities compared to the ANN model

To have a better idea of the performance of the proposed CNN model, it was compared against our previously developed ANN model when used to predict shear stress, Kolmogorov length, and velocity components in all directions (x, y, and z). New ANN and CNN models need to be trained for each variable separately. The RMSE values between the predicted profiles and the fine mesh profiles for both models for all variables are shown in **Table 3.2**.

In a previous study, a baseline model with a single hidden layer and 20 neurons, trained with the dataset at 90 rpm was developed to correct mesh-error of z-velocity by ~20% and Kolmogorov length by ~50% on almost all evaluation conditions except for the lowest mixing speed, 30 rpm. The effect of number of neurons and hidden layers on mesh-error correction was also studied and found that a network with 5 hidden layers with 20 neurons each would generate the best results for z-velocity (Cantarero-Rivera et al. 2024). This optimized structure was used here to predict all variables and a combination of 4 mixing speeds was used for training (30, 60, 90, and 150 rpm) instead of a single dataset. By applying these changes, the ANN model was now able to correct z-velocity by up to 50% and Kolmogorov length by up to 73%; however, the model was unable to correct the scenarios with the lower mixing speeds, 30 and 60 rpm, for all variables. These results highlight that the ANN model struggles greatly to correct the mesh errors for the lower mixing speeds. This issue was discussed previously (Cantarero-Rivera et al. 2024) and is particularly present when there is a high mixing speed profile in the training dataset and the more distant this is from the dataset to be corrected, the more severe the issue becomes.

The 3D CNN U-Net model, on the other hand, was able to predict shear stress across all scenarios with an average improvement on coarse profile of 67% and Kolmogorov length, with an average improvement on coarse profile of 30%. The model had limited capability in predicting the velocity components; however, the RMSE values indicate that the 3D CNN model had similar performance across all mixing conditions for all variables. This is attributed to the difference in how both algorithms learn and what input data is being provided. The ANN-based models use the nodal values as independent datapoints and the prediction is highly affected by the features provided. In contrast, the CNN-based models are able to use the entire profile and the relationship between neighboring datapoints is taken into consideration (Guo et al. 2016). Furthermore, the convolution layers will extract the features directly while for the ANN models, these features must be selected beforehand by the user and if these are not properly selected, the prediction performance may be hindered (Hanna et al. 2020). The lack of error correction for the velocity components by the 3D CNN U-Net model was attributed to a couple of reasons. First, the model was optimized for shear stress predictions and not for velocity components whereas the ANN model was optimized to correct z-velocity data and can be reasonably expected to have a similar performance when predicting other velocity components. Second, the 3D CNN U-Net model used ReLU activation functions which eliminates negative values from the gradients and turns them into zero. Changing this to a sigmoid or an exponential linear unit activation functions (ELU) activation function which retains negative values may help improve performance with variables that rely on negative values (Kim et al. 2020). The ANN model used a sigmoid activation function and as mentioned previously, this allows for the values between neurons to have both positive and negative values thus allowing the model to predict velocity components with higher accuracy than our proposed 3D CNN U-Net model. Another significant difference between the models is the way they were trained. The ANN was trained with four of the five mixing speeds (30, 60, 90, and 150 rpm) that were to be predicted. On the other hand, the 3D CNN U-Net model was trained on 40 datasets with varying mixing speeds and viscosities and then used to predict the 5 scenarios presented here. This would allow the ANN model to perform better than our proposed model since it has already seen 80% of all the evaluation scenarios during training.

A comparison of the computational time required by both models is shown in **Table 3.3**. Since the 3D CNN U-Net model was trained with 40 datasets, the training time was considerably longer than the time it took to train the ANN model for most variables, except for z-velocity where the CNN model took less time for training. Furthermore, the efficiency of the 3D CNN model is readily seen in the time it required to predict every new dataset. Unlike the ANN model, which required nearly 2 hours to predict every new dataset, the 3D CNN model was able to do the same task in seconds.

3.2.1 Testing generalization - Using optimized CNN across different impeller geometries

The 3D CNN U-Net model was also retrained and used to predict shear stress and Kolmogorov length across bioreactors with different impeller geometries such as the simple rod and the Rushton impeller. As mentioned previously, the simple rod impeller mimics lab-scale equipment while the Rushton impeller is typically found in larger, industrial scale bioreactors. Prediction results for shear stress indicate that the model has trouble regenerating the high-resolution data across geometries when only trained with the paddle impeller shear stress data (**Table 3.4**). However, the model has great performance when predicting the high-resolution Kolmogorov length values across geometries with improvements up to 32% when predicting the simple rod impeller and up to 54% when predicting the Rushton impeller profile (**Table 3.5**). The results within the same impeller geometry are somewhat varied but a trend emerges here once more where the lower Reynolds' scenarios (Re = 1223 and 2374) are the ones with the worst performance.

These results are also compared qualitatively with surface plots that show the shear stress (**Figure 3.8**) and Kolmogorov length (**Figure 3.9**) for the first predicted dataset with Re = 4080 as an example. These results show that the model was able to recover the shear stress and Kolmogorov length profiles across bioreactors with different impeller geometries. The areas with the most improvement are those close to the impeller which would in turn have the most detrimental effect on cells grown in the bioreactors.

One way to improve these results is to include all geometries in the training process. All 50 simulations for each impeller geometry were combined into a single dataset of 150 shear stress flow profiles which was then randomly split into 80% for training, 10% for validation, and the last 10% for evaluation. Because of the increased number of training datasets, the training time increased considerably but time required to predict new datasets remained the same, ~5 seconds per prediction. The prediction results are shown in **Table 3.6**. These results show great improvement in the model's generalization capabilities as all predictions showed positive results with an average improvement on the coarse flow profiles of 57%. This highlights how important a larger dataset is for CNN-based models and the impact that can have on their prediction capabilities. It is known that CNN-based models perform better with a larger training dataset provided (Thuerey et al. 2020). Correlation plots and surface plots comparing the coarse, predicted, and high-resolution shear stress profiles for all the testing conditions can be found in supplementary figures 1 and 2, respectively.

3.3 Usefulness, limitations, and future work

This study demonstrated a modified version of the TVSR model developed by Zhou et al. (2022) that used the U-Net structure. This model, based on CNN, was able to predict a high-resolution fluid profile for various parameters (shear stress, Kolmogorov length, and z-velocity component) from a coarse, low-resolution, fluid profile. The proposed model was able to obtain similar results to the base TVSR model but was computationally more efficient because of the smaller batch size and number of filters being used at every convolution layer. Apart from the reduced computational time, having a smaller batch size and fewer filters at every convolution layer allows for computers with less memory to be able to train and run the model for predictions. The predictions for both CNN-based models only requires a couple of seconds while a high-resolution CFD model may take anywhere from 5 – 20 hours depending on the machine used to run the program.

The proposed model was able to generate reliable high-resolution profiles when applied to different mixing conditions within the same bioreactor. However, it had very limited generalization across bioreactors with different impeller geometries when trained with data from a single impeller geometry. This was resolved by including data from all impeller shapes in the training and the model was able to achieve an average improvement on the coarse data of 57%. Further improvements on generalization may be obtained by optimizing more settings such as the L2 regularization term, also called weight decay, which can help in preventing overfitting and improving generalization (Ide and Kurita 2017; Shi et al. 2019). Another way the proposed model could be improved, specifically for the velocity components and any other variables that may have negative values is by using ELU activation functions instead of the typical ReLU function. The ReLU function basically converts any negative gradient into zero while the ELU will retain the negative value which reduces the bias shift effect and pushes the mean of the activation function closer to zero (Kim et al. 2020).

The proposed approach may also be used to design bioreactors and impellers with improved computational efficiency with the ultimate goal being to develop a digital twin of the bioreactor for better process control. The digital twins combine real-time monitoring, statistical analysis, and numerical modeling of the bioprocess within an interactive platform for optimal control of relevant processing parameters (Park et al. 2021). These digital twins rely on highly accurate and reliable monitoring systems to provide continuous data on the physical component and on efficient comprehensive models that can be a comprehensive digital representation of the physical component in all aspects (Chen et al. 2020). Conventional CFD models, although they provide highly accurate data, are not feasible to use for a digital twin because of their high development and computational costs. A hybrid modeling strategy that leverages the speed and computational efficiency of machine learning models and the accuracy of the CFD models is ideal to develop a digital twin. A recent study proposed an automation platform to monitor and control relevant process variables on-line (Lee et al. 2021). The gPROMS Digital Applications Platform (gDAP) is an integrated framework to monitor a bioreactor by connecting the model, database, and plant. It is used to automate the online implementation of input values and activation of the gPROMS model.

4. Conclusions

The 3D CNN U-Net model was able to predict high-resolution fluid shear stress profiles within a bioreactor with a paddle impeller with an average improvement on the coarse, low-resolution data of 72%. This study demonstrated how increasing the number of residual blocks did not necessarily lead to better results as previously suggested by some studies (Kim et al. 2016; Lim et al. 2017; Tai et al. 2017). In our case, 8 residual blocks had better training and validation RMSE values compared against 4 and 16 residual blocks. Furthermore, reducing the batch size down to 2 was shown to have considerably lower training and validation RMSE values. Although using this setting may increase training time somewhat, as opposed to using a larger batch size, the memory required to run the model is significantly reduced as less data is being processed at every iteration.

This approach may be further optimized and used to predict other variables of interest for large-scale bioreactor cell culture such as oxygen spatial and temporal variation and metabolic yield coefficients. With some modifications, this model's prediction speed may also be useful to develop real-time feedback loops between a real bioreactor to calculate the desired processing parameters, modify the corresponding controls, and therefore establish a digital twin system.

Acknowledgments

This work was supported by the AI Tennessee Initiative at the University of Tennessee.

REFERENCES

Ajuria Illarramendi E, Bauerheim M, Ashton N, et al (2023) Performance Study of Convolutional Neural Network Architectures for 3D Incompressible Flow Simulations. In: Proceedings of the Platform for Advanced Scientific Computing Conference. Association for Computing Machinery, New York, NY, USA, pp 1–11

Alfieri R, Vassalli M, Viti F (2019) Flow-induced mechanotransduction in skeletal cells. Biophys Rev 11:729–743. https://doi.org/10.1007/s12551-019-00596-1

Berry JD, Liovic P, Šutalo ID, et al (2016) Characterisation of stresses on microcarriers in a stirred bioreactor. Applied Mathematical Modelling 40:6787–6804. https://doi.org/10.1016/j.apm.2016.02.025

Bliatsiou C, Malik A, Böhm L, Kraume M (2019) Influence of Impeller Geometry on Hydromechanical Stress in Stirred Liquid/Liquid Dispersions. Ind Eng Chem Res 58:2537–2550. https://doi.org/10.1021/acs.iecr.8b03654

Borys BS, Le A, Roberts EL, et al (2019) Using computational fluid dynamics (CFD) modeling to understand murine embryonic stem cell aggregate size and pluripotency distributions in stirred suspension bioreactors. Journal of Biotechnology 304:16–27. https://doi.org/10.1016/j.jbiotec.2019.08.002

Cantarero-Rivera FJ, Yang R, Li H, et al (2024) An artificial neural network-based machine learning approach to correct coarse-mesh-induced error in computational fluid dynamics modeling of cell culture bioreactor. Food and Bioproducts Processing 143:128–142. https://doi.org/10.1016/j.fbp.2023.11.004

Chen L, Wang H, Zhao J, et al (2018) The Effect of Network Width on the Performance of Large-batch Training. In: Bengio S, Wallach H, Larochelle H, et al. (eds) Advances in Neural Information Processing Systems. Curran Associates, Inc.

Chen Y, Yang O, Sampat C, et al (2020) Digital Twins in Pharmaceutical and Biopharmaceutical Manufacturing: A Literature Review. Processes 8:1088. https://doi.org/10.3390/pr8091088

Cherry RS, Kwon K-Y (1990) Transient shear stresses on a suspension cell in turbulence. Biotechnology and Bioengineering 36:563–571. https://doi.org/10.1002/bit.260360603

Choi J, Lee SY, Yoo Y-M, Kim CH (2017) Maturation of Adipocytes is Suppressed by Fluid Shear Stress. Cell Biochem Biophys 75:87–94. https://doi.org/10.1007/s12013-016-0771-4

Çiçek Ö, Abdulkadir A, Lienkamp SS, et al (2016) 3D U-Net: Learning Dense Volumetric Segmentation from Sparse Annotation. In: Ourselin S, Joskowicz L, Sabuncu MR, et al. (eds) Medical Image Computing and Computer-Assisted Intervention – MICCAI 2016. Springer International Publishing, Cham, pp 424–432

Delafosse A, Loubière C, Calvo S, et al (2018) Solid-liquid suspension of microcarriers in stirred tank bioreactor – Experimental and numerical analysis. Chemical Engineering Science 180:52–63. https://doi.org/10.1016/j.ces.2018.01.001

Dong C, Loy CC, He K, Tang X (2016) Image Super-Resolution Using Deep Convolutional Networks. IEEE Transactions on Pattern Analysis and Machine Intelligence 38:295–307. https://doi.org/10.1109/TPAMI.2015.2439281

Ferziger JH, Perić M (2002) Efficiency and Accuracy Improvement. In: Ferziger JH, Perić M (eds) Computational Methods for Fluid Dynamics. Springer Berlin Heidelberg, Berlin, Heidelberg, pp 329–367

Freiberger F, Budde J, Ateş E, et al (2022) New Insights from Locally Resolved Hydrodynamics in Stirred Cell Culture Reactors. Processes 10:107. https://doi.org/10.3390/pr10010107

Fukami K, Fukagata K, Taira K (2019) Super-resolution reconstruction of turbulent flows with machine learning. J Fluid Mech 870:106–120. https://doi.org/10.1017/jfm.2019.238

Ghasemian M, Layton C, Nampe D, et al (2020) Hydrodynamic characterization within a spinner flask and a rotary wall vessel for stem cell culture. Biochemical Engineering Journal 157:107533. https://doi.org/10.1016/j.bej.2020.107533

Guo X, Li W, Iorio F (2016) Convolutional Neural Networks for Steady Flow Approximation. In: Proceedings of the 22nd ACM SIGKDD International Conference on Knowledge Discovery and Data Mining. Association for Computing Machinery, New York, NY, USA, pp 481–490

Hammond J, Pepper N, Montomoli F, Michelassi V (2022) Machine Learning Methods in CFD for Turbomachinery: A Review. IJTPP 7:16. https://doi.org/10.3390/ijtpp7020016

Han J-E, Lee H, Ho T-T, Park S-Y (2022) Brazzein protein production in transgenic carrot cells using air-lift bioreactor culture. Plant Biotechnol Rep 16:161–171. https://doi.org/10.1007/s11816-022-00743-3

Hanna BN, Dinh NT, Youngblood RW, Bolotnov IA (2020) Machine-learning based error prediction approach for coarse-grid Computational Fluid Dynamics (CG-CFD). Progress in Nuclear Energy 118:103140. https://doi.org/10.1016/j.pnucene.2019.103140

He K, Zhang X, Ren S, Sun J (2016) Deep Residual Learning for Image Recognition. In: 2016 IEEE Conference on Computer Vision and Pattern Recognition (CVPR). IEEE, Las Vegas, NV, USA, pp 770–778

Hoffer E, Hubara I, Soudry D (2017) Train longer, generalize better: closing the generalization gap in large batch training of neural networks. In: Guyon I, Luxburg UV, Bengio S, et al. (eds) Advances in Neural Information Processing Systems. Curran Associates, Inc.

Ide H, Kurita T (2017) Improvement of learning for CNN with ReLU activation by sparse regularization. In: 2017 International Joint Conference on Neural Networks (IJCNN). pp 2684–2691

Jin X, Cheng P, Chen W-L, Li H (2018) Prediction model of velocity field around circular cylinder over various Reynolds numbers by fusion convolutional neural networks based on pressure on the cylinder. Physics of Fluids 30:047105. https://doi.org/10.1063/1.5024595

Joshi JB, Nere NK, Rane CV, et al (2011) CFD simulation of stirred tanks: Comparison of turbulence models. Part I: Radial flow impellers. Can J Chem Eng 89:23–82. https://doi.org/10.1002/cjce.20446

Kandel I, Castelli M (2020) The effect of batch size on the generalizability of the convolutional neural networks on a histopathology dataset. ICT Express 6:312–315. https://doi.org/10.1016/j.icte.2020.04.010

Kiener A, Langer S, Bekemeyer P (2023) Data-driven correction of coarse grid CFD simulations. Computers & Fluids 264:105971. https://doi.org/10.1016/j.compfluid.2023.105971

Kim D, Kim J, Kim J (2020) Elastic exponential linear units for convolutional neural networks. Neurocomputing 406:253–266. https://doi.org/10.1016/j.neucom.2020.03.051

Kim J, Lee JK, Lee KM (2016) Accurate Image Super-Resolution Using Very Deep Convolutional Networks. In: 2016 IEEE Conference on Computer Vision and Pattern Recognition (CVPR). pp 1646–1654

Kochkov D, Smith JA, Alieva A, et al (2021) Machine learning–accelerated computational fluid dynamics. Proc Natl Acad Sci USA 118:e2101784118. https://doi.org/10.1073/pnas.2101784118

Krizhevsky A, Sutskever I, Hinton GE (2017) ImageNet classification with deep convolutional neural networks. Commun ACM 60:84–90. https://doi.org/10.1145/3065386

Launder BE, Spalding DB (1974) The numerical computation of turbulent flows. Computer Methods in Applied Mechanics and Engineering 3:269–289. https://doi.org/10.1016/0045-7825(74)90029-2

Le DK, Guo M, Yoon JY (2023) A hybrid CFD – Deep Learning methodology to improve the accuracy of cut-off diameter prediction in coarse-grid simulations for cyclone separators. Journal of Aerosol Science 170:106143. https://doi.org/10.1016/j.jaerosci.2023.106143

Lee HJ, Fadda S, Souza LFS, Lee JM (2021) Digital application of bioreactor monitoring. In: 2021 21st International Conference on Control, Automation and Systems (ICCAS). pp 382–387

Li C-Q, Yang W (2023) Essential reliability methods. In: Time-Dependent Reliability Theory and Its Applications. Elsevier, pp 51–119

Lim B, Son S, Kim H, et al (2017) Enhanced Deep Residual Networks for Single Image Super-Resolution. In: 2017 IEEE Conference on Computer Vision and Pattern Recognition Workshops (CVPRW). pp 1132–1140

Liu B, Tang J, Huang H, Lu X-Y (2020) Deep learning methods for super-resolution reconstruction of turbulent flows. Physics of Fluids 32:025105. https://doi.org/10.1063/1.5140772

Lu Z, Chen Y (2022) Single image super-resolution based on a modified U-net with mixed gradient loss. SIViP 16:1143–1151. https://doi.org/10.1007/s11760-021-02063-5

Mckay MD, Beckman RJ, Conover WJ (2000) A Comparison of Three Methods for Selecting Values of Input Variables in the Analysis of Output From a Computer Code. Technometrics 42:55–61. https://doi.org/10.1080/00401706.2000.10485979

Mehta R, Arbel T (2019) 3D U-Net for Brain Tumour Segmentation. In: Crimi A, Bakas S, Kuijf H, et al. (eds) Brainlesion: Glioma, Multiple Sclerosis, Stroke and Traumatic Brain Injuries. Springer International Publishing, Cham, pp 254–266

Mishra S, Kumar V, Sarkar J, Rathore AS (2021) CFD based mass transfer modeling of a single use bioreactor for production of monoclonal antibody biotherapeutics. Chemical Engineering Journal 412:128592. https://doi.org/10.1016/j.cej.2021.128592

Mustapha A, Mohamed L, Ali K (2021) Comparative study of optimization techniques in deep learning: Application in the ophthalmology field. Journal of Physics: Conference Series 1743:012002. https://doi.org/10.1088/1742-6596/1743/1/012002

Oyedotun OK, Papadopoulos K, Aouada D (2023) A new perspective for understanding generalization gap of deep neural networks trained with large batch sizes. Appl Intell 53:15621–15637. https://doi.org/10.1007/s10489-022-04230-8

Panchigar D, Kar K, Shukla S, et al (2022) Machine learning-based CFD simulations: a review, models, open threats, and future tactics. Neural Comput & Applic 34:21677–21700. https://doi.org/10.1007/s00521-022-07838-6

Park S-Y, Park C-H, Choi D-H, et al (2021) Bioprocess digital twins of mammalian cell culture for advanced biomanufacturing. Current Opinion in Chemical Engineering 33:100702. https://doi.org/10.1016/j.coche.2021.100702

Ramírez LA, Pérez EL, García Díaz C, et al (2020) CFD and Experimental Characterization of a Bioreactor: Analysis via Power Curve, Flow Patterns and k L a. Processes 8:878. https://doi.org/10.3390/pr8070878

Ronneberger O, Fischer P, Brox T (2015) U-Net: Convolutional Networks for Biomedical Image Segmentation. In: Navab N, Hornegger J, Wells WM, Frangi AF (eds) Medical Image Computing and Computer-Assisted Intervention – MICCAI 2015. Springer International Publishing, Cham, pp 234–241

Scully J, Considine LB, Smith MT, et al (2020) Beyond heuristics: CFD-based novel multiparameter scale-up for geometrically disparate bioreactors demonstrated at industrial 2kL–10kL scales. Biotechnology and Bioengineering 117:1710–1723. https://doi.org/10.1002/bit.27323

Seidel S, Mozaffari F, Maschke RW, et al (2023) Automated Shape and Process Parameter Optimization for Scaling Up Geometrically Non-Similar Bioreactors. Processes 11:2703. https://doi.org/10.3390/pr11092703

Shi G, Zhang J, Li H, Wang C (2019) Enhance the Performance of Deep Neural Networks via L2 Regularization on the Input of Activations. Neural Process Lett 50:57–75. https://doi.org/10.1007/s11063-018-9883-8

Spann R, Glibstrup J, Pellicer-Alborch K, et al (2019) CFD predicted pH gradients in lactic acid bacteria cultivations. Biotechnology and Bioengineering 116:769–780. https://doi.org/10.1002/bit.26868

Szegedy C, Liu W, Jia Y, et al (2015) Going deeper with convolutions. In: 2015 IEEE Conference on Computer Vision and Pattern Recognition (CVPR). pp 1–9

‘t Hart DC, van der Vlag J, Nijenhuis T (2021) Laminar flow substantially affects the morphology and functional phenotype of glomerular endothelial cells. PLoS ONE 16:e0251129. https://doi.org/10.1371/journal.pone.0251129

Tai Y, Yang J, Liu X (2017) Image Super-Resolution via Deep Recursive Residual Network. In: 2017 IEEE Conference on Computer Vision and Pattern Recognition (CVPR). pp 2790–2798

Thuerey N, Weißenow K, Prantl L, Hu X (2020) Deep Learning Methods for Reynolds-Averaged Navier–Stokes Simulations of Airfoil Flows. AIAA Journal 58:25–36. https://doi.org/10.2514/1.J058291

Ueki M, Tansho N, Sato M, et al (2021) Improved cultivation of Chinese hamster ovary cells in bioreactor with reciprocal mixing. Journal of Bioscience and Bioengineering 132:531–536. https://doi.org/10.1016/j.jbiosc.2021.08.003

Villiger TK, Neunstoecklin B, Karst DJ, et al (2018) Experimental and CFD physical characterization of animal cell bioreactors: From micro- to production scale. Biochemical Engineering Journal 131:84–94. https://doi.org/10.1016/j.bej.2017.12.004

Vinuesa R, Brunton SL (2022) Enhancing computational fluid dynamics with machine learning. Nat Comput Sci 2:358–366. https://doi.org/10.1038/s43588-022-00264-7

Wilcox DC (2006) Turbulence modeling for CFD, 3rd ed. DCW Industries, La Cãnada, Calif

Zhang J, Li X, Liu H, et al (2021) Hydrodynamics and mass transfer in spinner flasks: Implications for large scale cultured meat production. Biochemical Engineering Journal 167:107864. https://doi.org/10.1016/j.bej.2020.107864

Zhou Z, Li B, Yang X, Yang Z (2022) A robust super-resolution reconstruction model of turbulent flow data based on deep learning. Computers & Fluids 239:105382. https://doi.org/10.1016/j.compfluid.2022.105382

APPENDIX

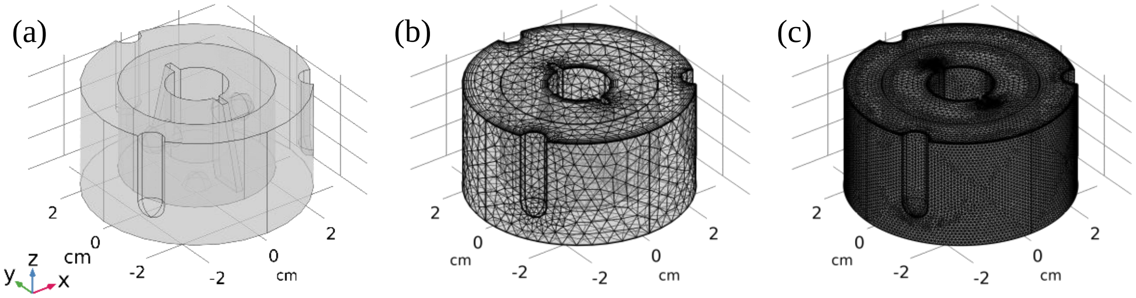

Figure 3.1. Spinner flask model of a Corning®, Series 4500-125spinner flask, with 100 mL working volume. (a) 3D snapshot of whole geometry, (b) coarse, and (c) fine mesh used to generate low and high-resolution results.

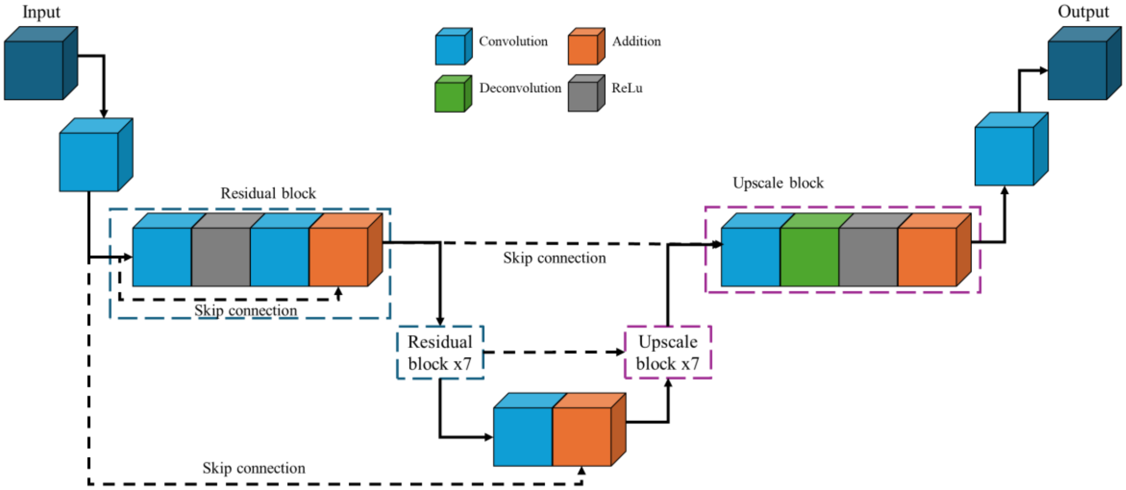

Figure 3.2. Diagram of the proposed 3D CNN U-Net model.

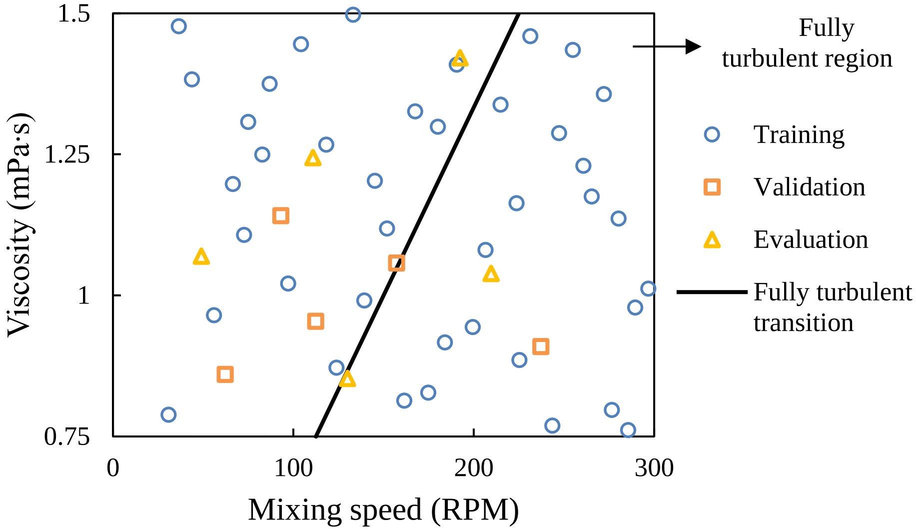

Figure 3.3. All 50 conditions simulated obtained through Latin Hypercube sampling method and separated into training, validation, and evaluation for 3D CNN U-Net model training and evaluation.

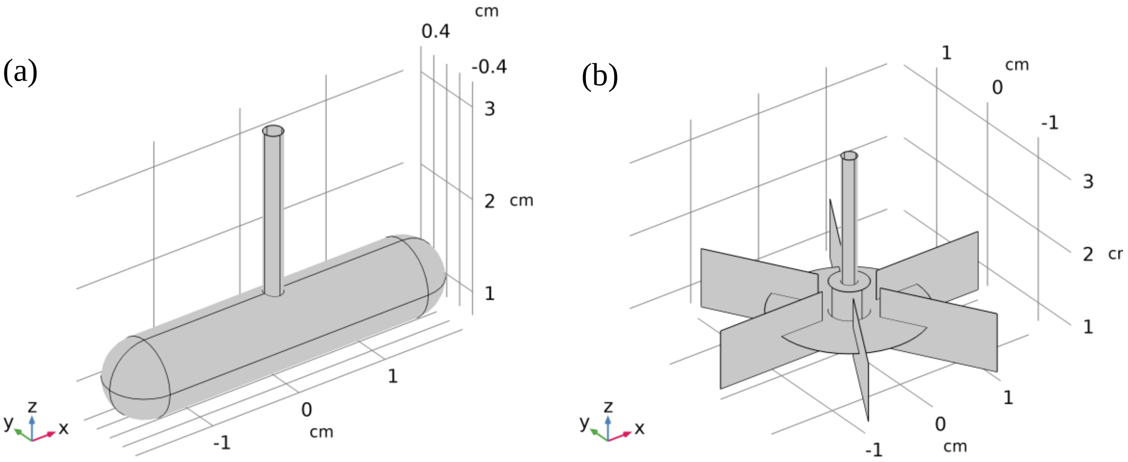

Figure 3.4. Geometries for (a) simple rod and (b) Rushton impeller.

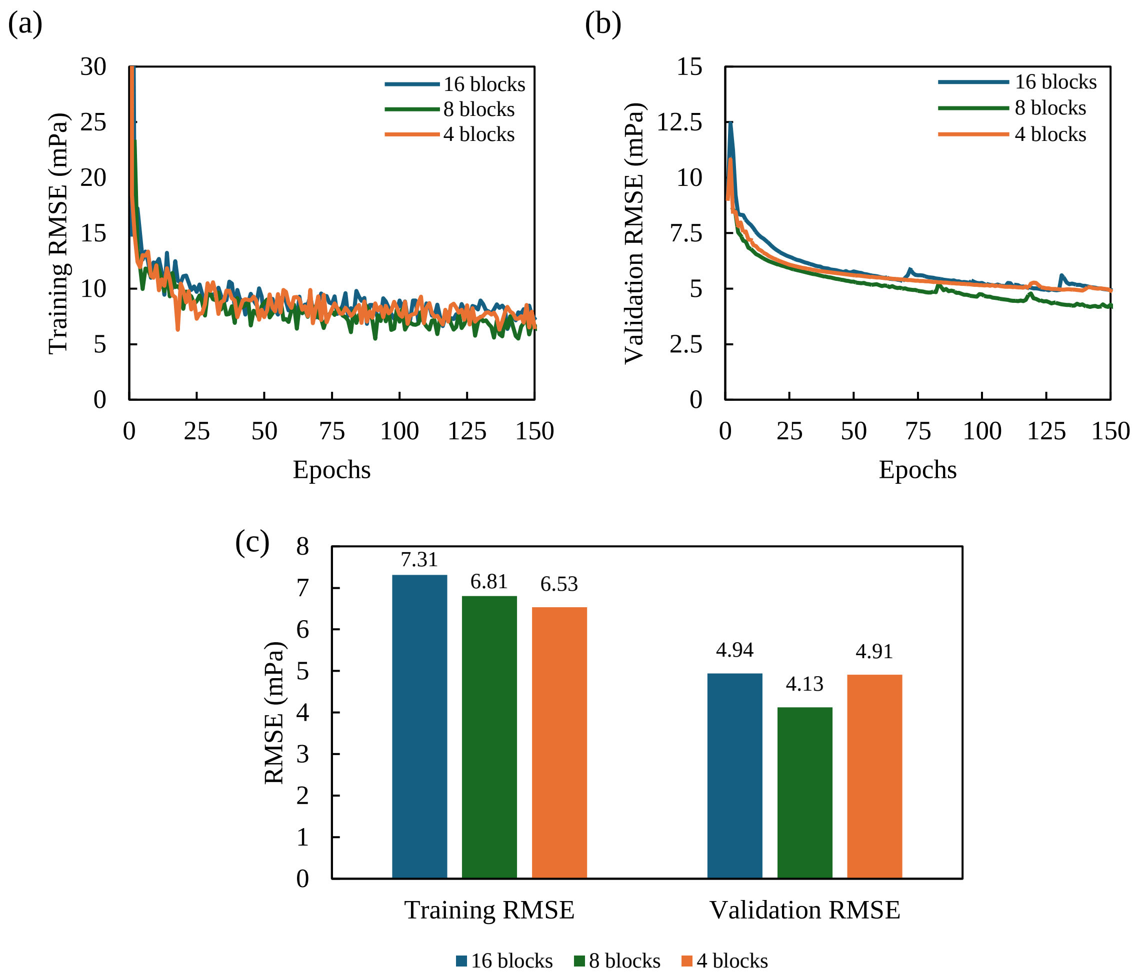

Figure 3.5. Variations of (a) training and (b) validation RMSE with training epochs and (c) their values at the last iteration of training when changing number of blocks in encoder and decoder parts. Model trained with shear stress CFD data.

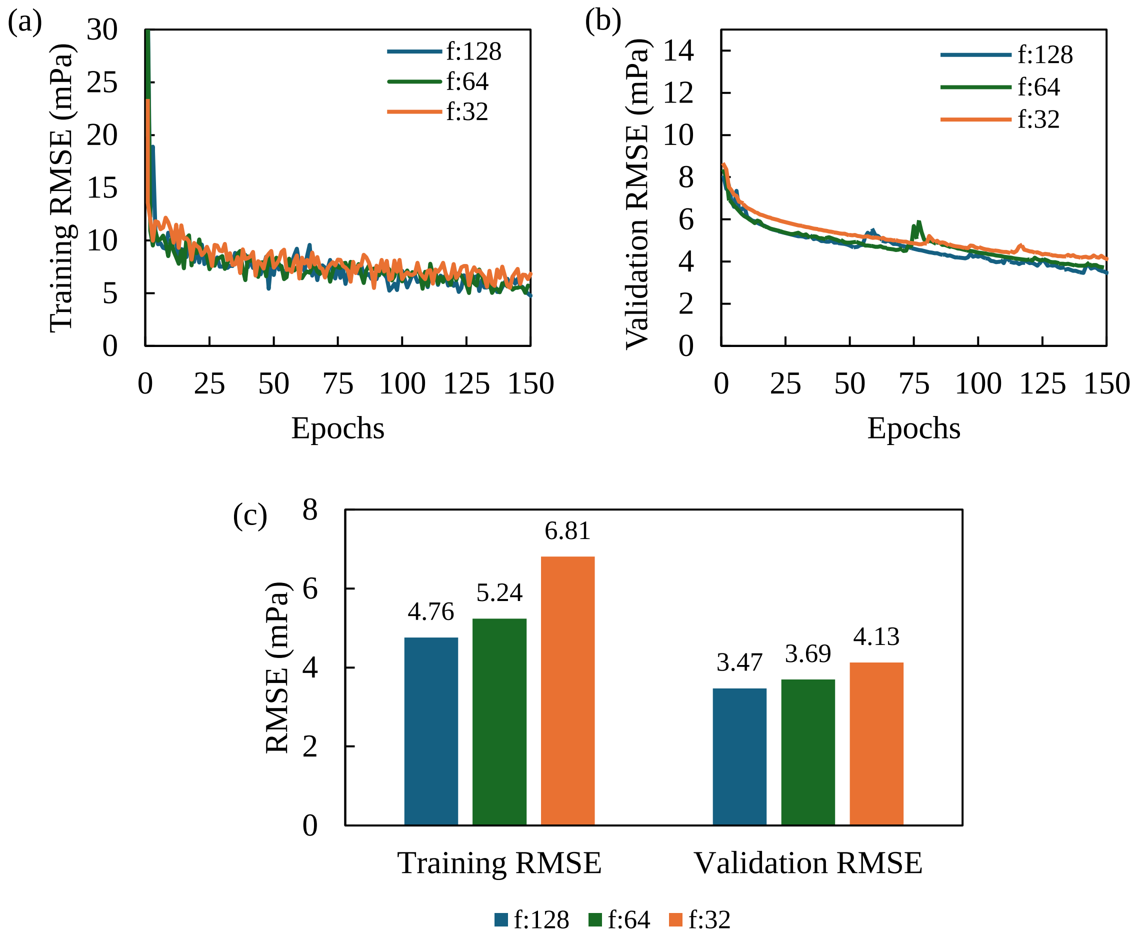

Figure 3.6. Variations of (a) training and (b) validation RMSE with training epochs and (c) their values at the last iteration of training when changing number of filters (f) in every convolution layer. Model trained with shear stress CFD data.

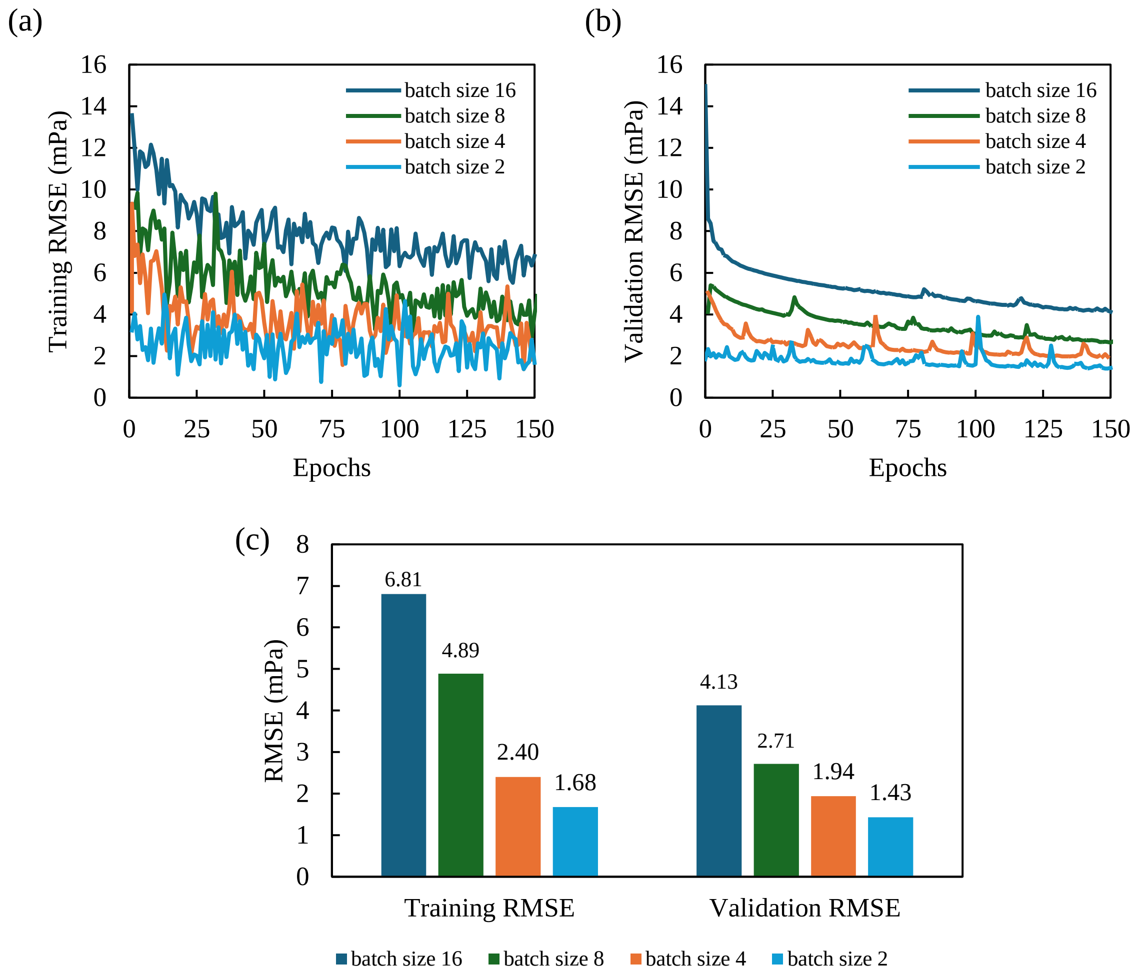

Figure 3.7. Variations of (a) training and (b) validation RMSE with training epochs and (c) their values at the last iteration of training when changing batch size. Model trained with shear stress CFD data.

Table 3.1. Hyperparameters settings of optimized 3D CNN U-Net model.

Hyperparameters of 3D CNN U-Net model	
Number of residual blocks	8
Number of upscale modules	8
Number of filters per convolution layer	32
Filter size	3×3×3
Activation function	ReLu
Input normalization	None
Batch size	2
Learning rate	0.0001

Table 3.2. Prediction performance comparison between ANN and 3D CNN U-Net models for shear stress, Kolmogorov length, and velocity components in all directions (x, y, and z).

Variable	Mixing speed (RPM)	Reynold's Number	Coarse RMSE	ANN		3D CNN U-Net	
				Prediction RMSE	ΔRMSE (%)	Prediction RMSE	ΔRMSE (%)
Shear stress (mPa)	30	800	1.00	2.91	190	0.52	-48
	60	1600	2.42	3.01	25	0.85	-65
	90	2400	3.91	3.73	-5	1.10	-72
	120	3200	5.42	4.82	-11	1.34	-75
	150	4000	6.92	6.10	-12	1.60	-77
Kolmogorov length (mm)	30	800	0.0148	0.0149	0	0.0184	24
	60	1600	0.0176	0.0074	-58	0.0126	-28
	90	2400	0.0178	0.0056	-68	0.0102	-43
	120	3200	0.0169	0.0047	-72	0.0086	-49
	150	4000	0.0157	0.0043	-73	0.0076	-52
x-velocity (m/s)	30	800	0.0015	0.0055	258	0.0021	35
	60	1600	0.0031	0.0043	40	0.0034	9
	90	2400	0.0047	0.0036	-23	0.0049	4
	120	3200	0.0064	0.0037	-42	0.0065	2
	150	4000	0.0080	0.0045	-44	0.0081	1
y-velocity (m/s)	30	800	0.0015	0.0060	301	0.0015	5
	60	1600	0.0030	0.0047	56	0.0030	0
	90	2400	0.0047	0.0039	-18	0.0047	-1
	120	3200	0.0065	0.0037	-43	0.0063	-2
	150	4000	0.0083	0.0044	-46	0.0081	-3
z-velocity (m/s)	30	800	0.0008	0.0057	605	0.0009	9
	60	1600	0.0023	0.0044	89	0.0022	-4
	90	2400	0.0040	0.0034	-15	0.0036	-9
	120	3200	0.0057	0.0030	-47	0.0050	-12
	150	4000	0.0073	0.0035	-53	0.0063	-14

Table 3.3. Comparison of computational core hours required to train and predict a new dataset between ANN and 3D CNN U-Net models

Variable	Model	Training time (h)	Cores	Training time (cores*h)	Prediction time (min/dataset)	Prediction time (cores*min/dataset)
Shear stress	ANN	7.76	16	124.16	123.33	1973.33
(mPa)	3D CNN	27.79	24	667.07	0.08	1.84
Kolmogorov	ANN	24.40	16	390.44	118.77	1900.39
length (mm)	3D CNN	25.47	24	611.29	0.07	1.74
x-velocity	ANN	7.73	24	185.42	102.30	2455.10
(m/s)	3D CNN	35.58	16	569.30	0.07	1.07
y-velocity	ANN	18.08	24	433.96	93.82	2251.79
(m/s)	3D CNN	35.91	16	574.60	0.07	1.12
z-velocity	ANN	8.18	24	196.25	97.87	2348.79
(m/s)	3D CNN	4.66	24	111.75	0.06	1.36

Table 3.4. Shear stress prediction performance across bioreactors with different impeller geometries.

Predicted Impeller	Reynold's Number	Coarse RMSE (mPa)	Prediction RMSE (mPa)	ΔRMSE (%)
Paddle	4080	5.10	1.15	-78
	1223	1.98	0.81	-59
	3611	12.47	2.89	-77
	2374	5.95	1.67	-72
	5383	10.27	2.23	-78
Simple rod	4080	4.22	4.20	0
	1223	1.53	1.51	-2
	3611	10.30	10.24	-1
	2374	4.86	4.81	-1
	5383	8.46	8.45	0
Rushton	4080	5.23	4.91	-6
	1223	2.16	2.03	-6
	3611	12.78	12.11	-5
	2374	6.15	5.81	-5
	5383	10.59	10.01	-5

Table 3.5. Kolmogorov length prediction performance across bioreactors with different impeller geometries.

Predicted Impeller	Reynold's Number	Coarse RMSE (mm)	Prediction RMSE (mm)	ΔRMSE (%)
Paddle	4080	0.0157	0.0075	-52
	1223	0.0167	0.0145	-13
	3611	0.0164	0.0080	-51
	2374	0.0178	0.0102	-43
	5383	0.0138	0.0063	-55
Simple rod	4080	0.0422	0.0303	-28
	1223	0.0442	0.0424	-4
	3611	0.0431	0.0317	-26
	2374	0.0445	0.0359	-19
	5383	0.0393	0.0266	-32
Rushton	4080	0.0131	0.0068	-48
	1223	0.0128	0.0140	10
	3611	0.0133	0.0074	-45
	2374	0.0134	0.0099	-27
	5383	0.0126	0.0058	-54

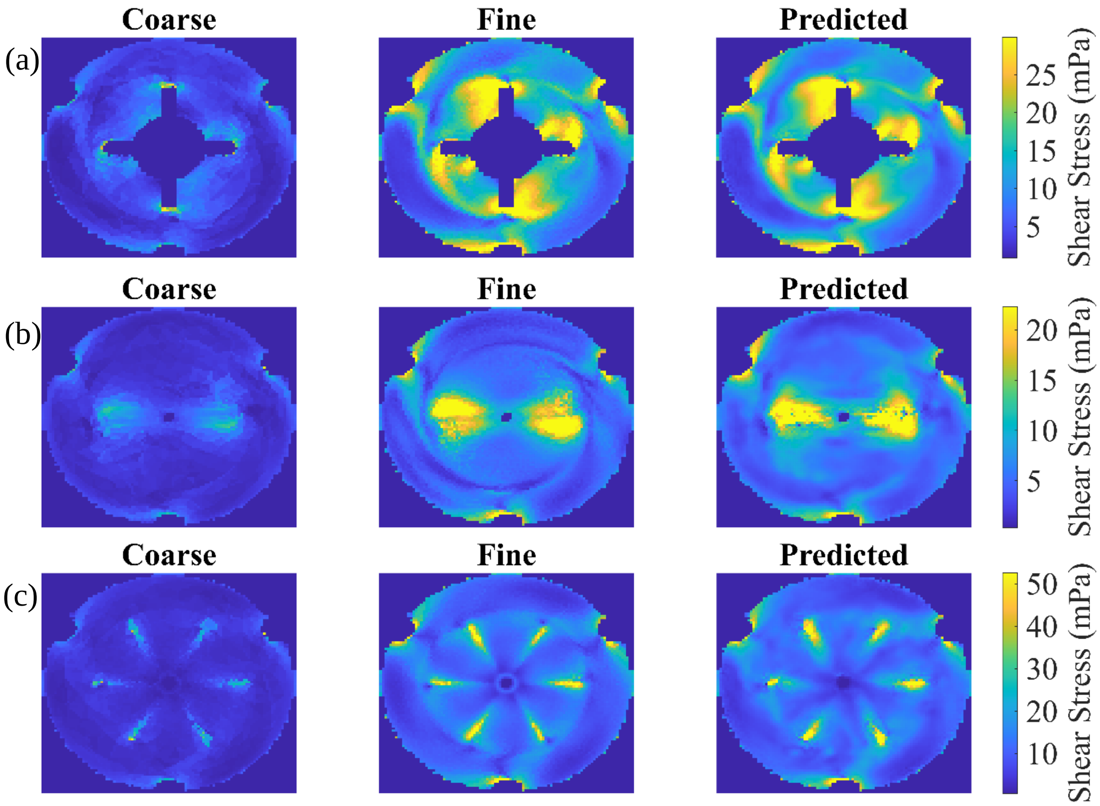

Figure 3.8. Shear stress fluid profile in the xy-plane at 2 cm from the bottom of the bioreactor with (a) paddle, (b) simple rod, and (c) Rushton impeller for Re = 4080.

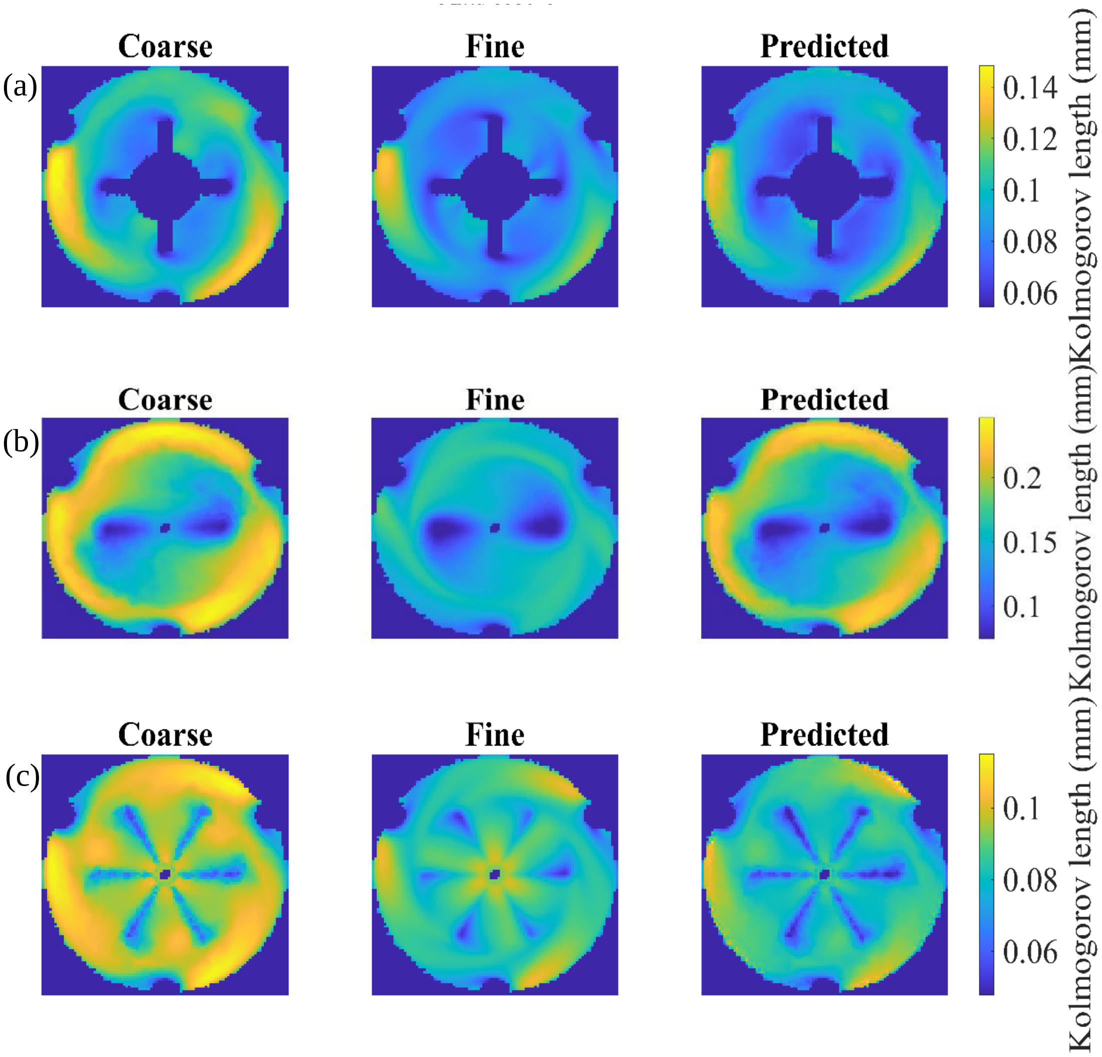

Figure 3.9. Kolmogorov length fluid profile in the xy-plane at 2 cm from the bottom of the bioreactor with (a) paddle, (b) simple rod, and (c) Rushton impeller for Re = 4080.

Table 3.6. Shear stress prediction performance across bioreactors with different impeller geometries when 3D CNN U-Net was trained with datasets from all impeller geometries.

Predicted Impeller	Reynold's Number	Coarse RMSE (mPa)	Prediction RMSE (mPa)	ΔRMSE (%)
Paddle	3143	4.79	1.84	-62
Simple Rod	1768	3.40	1.79	-47
Simple Rod	1751	2.64	1.40	-47
Paddle	2179	4.53	1.97	-57
Simple Rod	2487	5.32	2.43	-54
Paddle	6961	10.29	3.69	-64
Paddle	4064	5.09	1.85	-64
Paddle	1223	1.97	1.08	-45
Simple Rod	7820	11.56	5.08	-56
Paddle	3611	12.44	4.61	-63
Simple Rod	5094	8.57	3.53	-59
Rushton	3747	6.51	2.55	-61
Paddle	2374	5.93	2.50	-58
Paddle	5383	10.25	3.62	-65
Rushton	3143	4.94	1.99	-60

Supplementary Figures

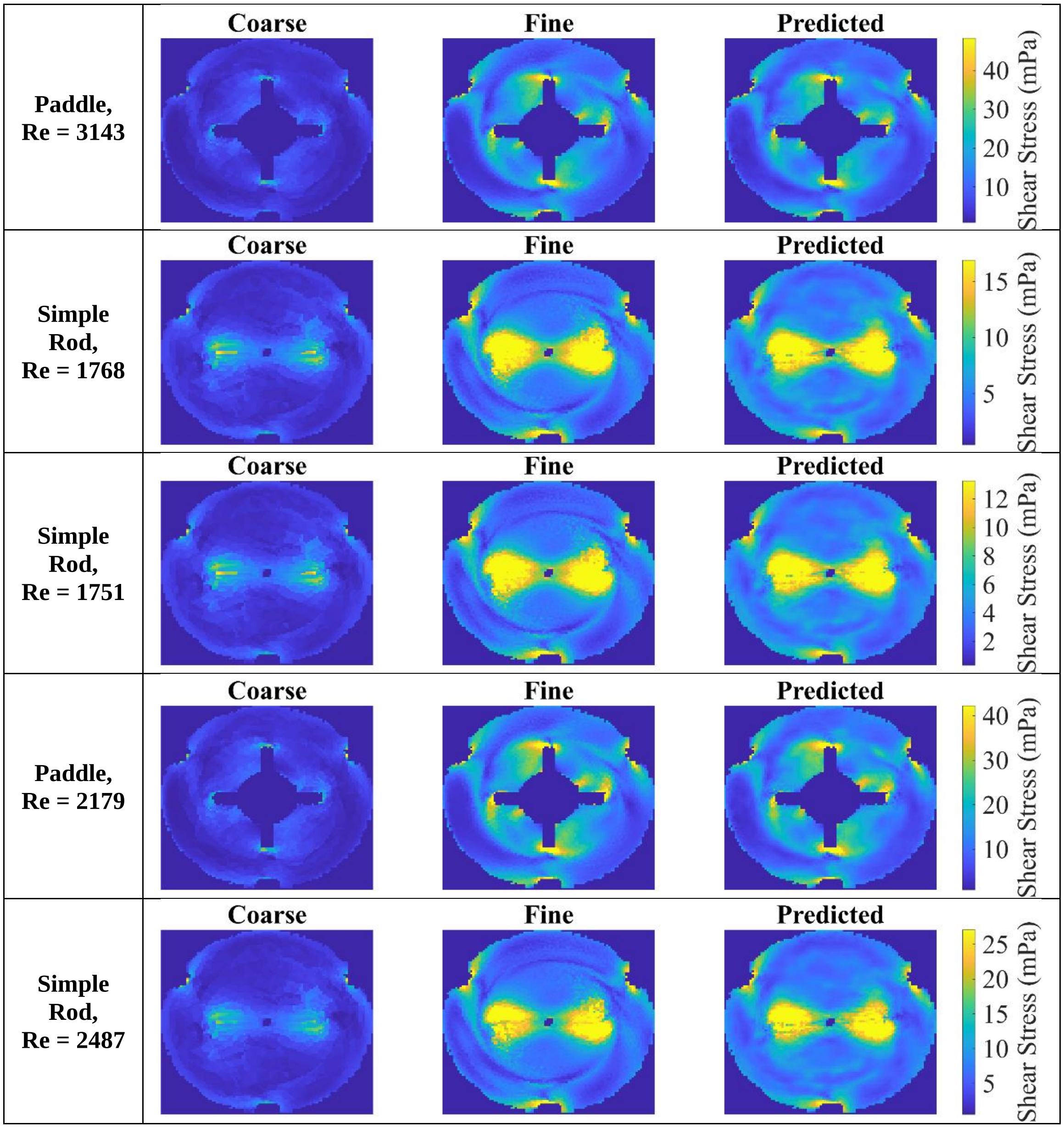

Supplementary figure 3.1. Shear stress fluid profile in the xy-plane at 2 cm from the bottom of the bioreactor. All geometries combined into a single training dataset.

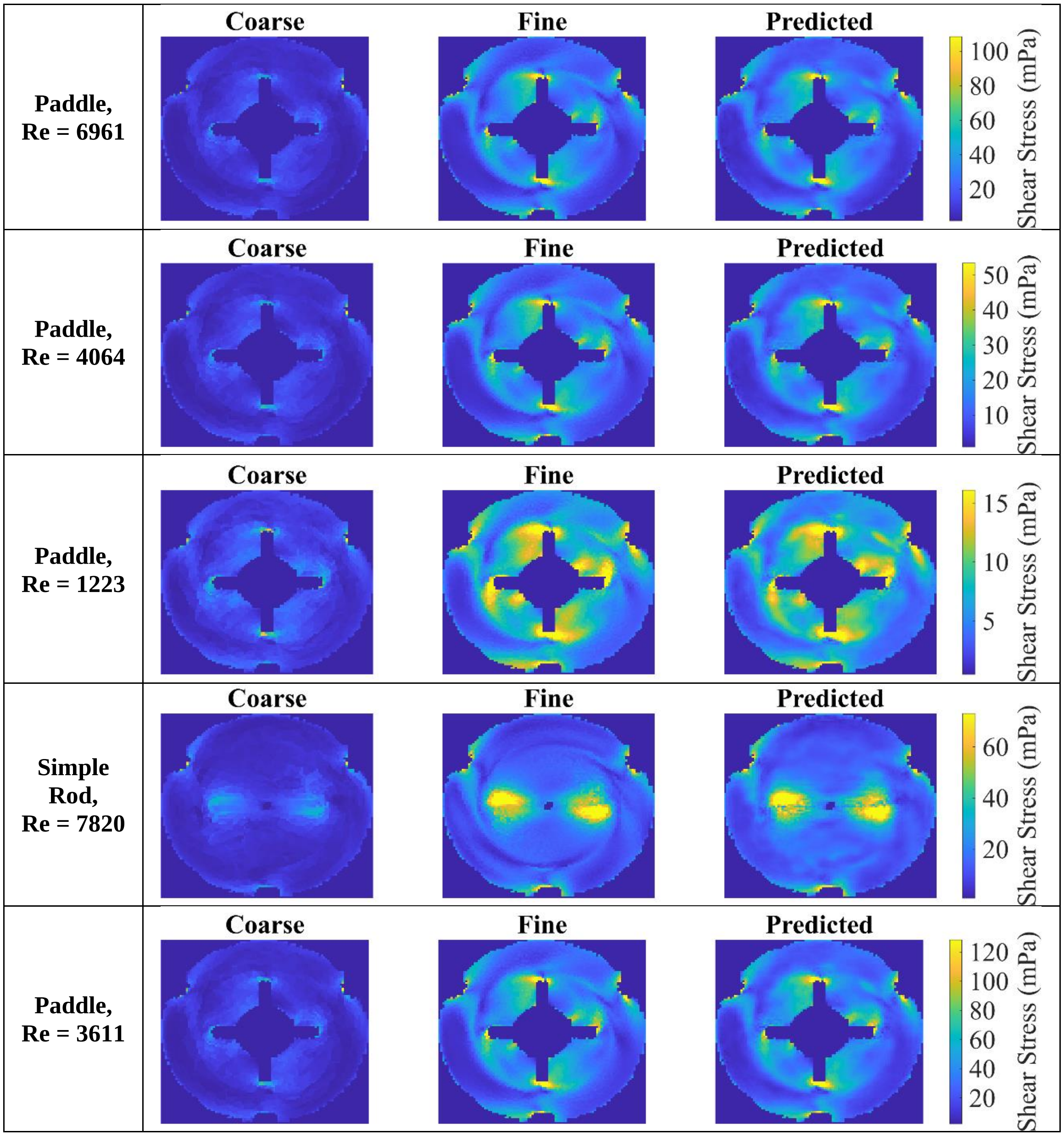

Supplementary figure 3.1. Continued.

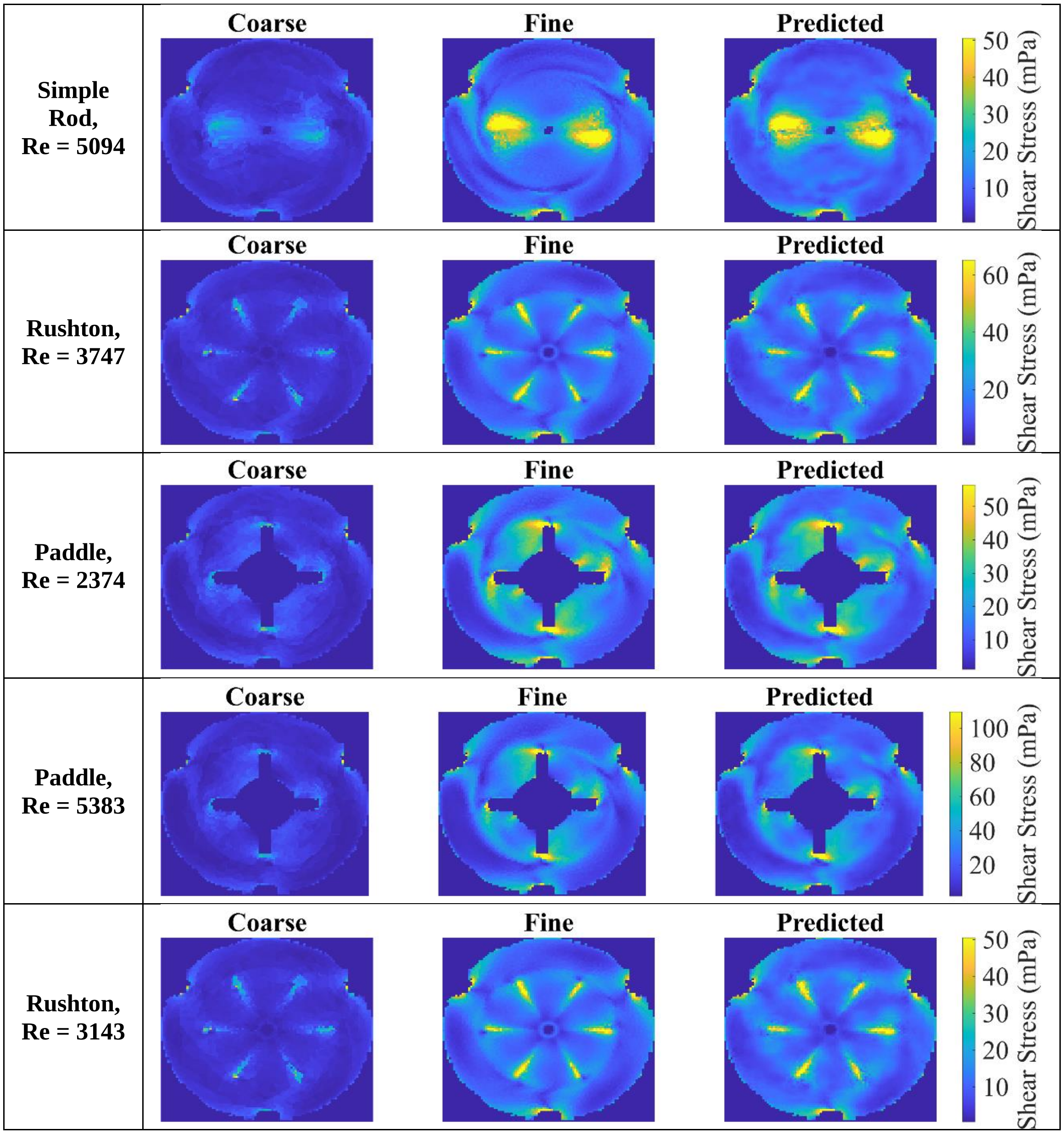

Supplementary figure 3.1. Continued

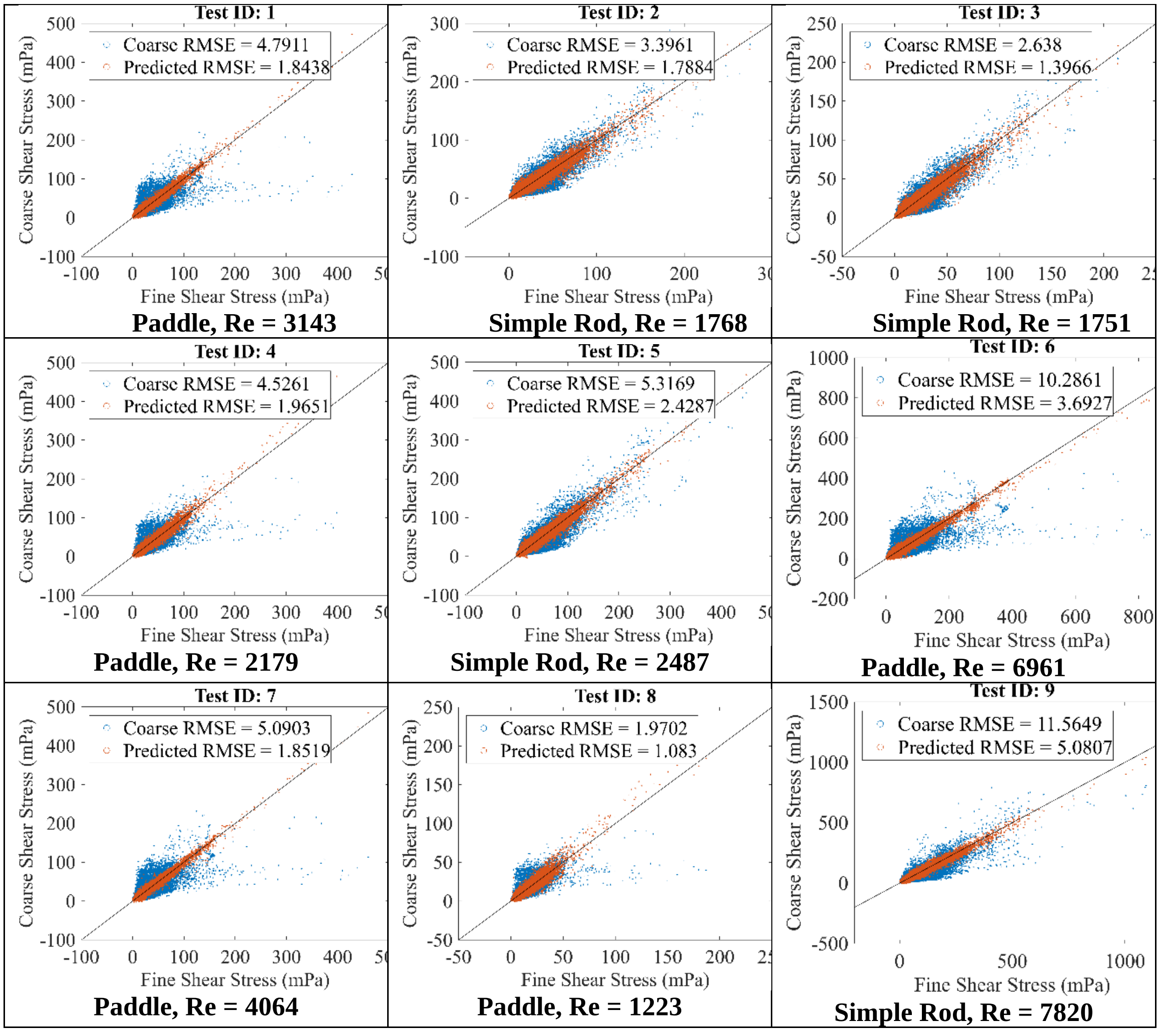

Paddle, Re = 3143 **Simple Rod, Re = 1768** **Simple Rod, Re = 1751**

Paddle, Re = 2179 **Simple Rod, Re = 2487** **Paddle, Re = 6961**

Paddle, Re = 4064 **Paddle, Re = 1223** **Simple Rod, Re = 7820**

Supplementary figure 3.2. Shear stress correlation plots between coarse and predicted against fine, high-resolution data. All geometries combined into a single training dataset.

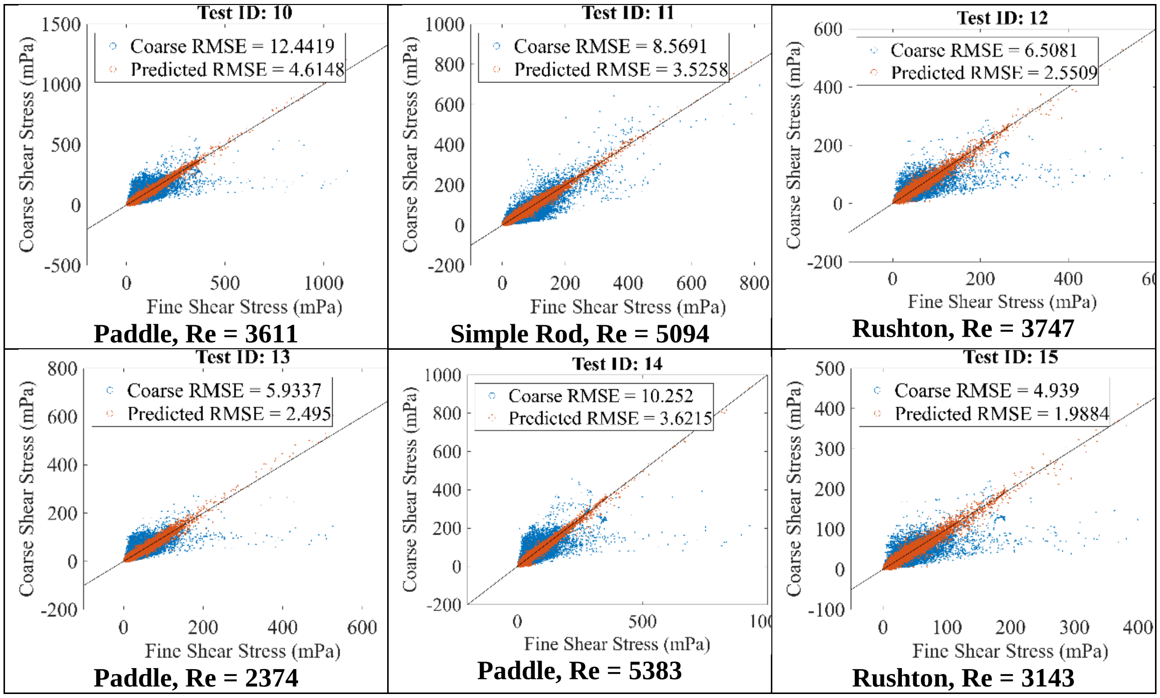

Paddle, Re = 3611

Simple Rod, Re = 5094

Rushton, Re = 3747

Paddle, Re = 2374

Paddle, Re = 5383

Rushton, Re = 3143

Supplementary figure 3.2. Continued.

4. CHAPTER IV.

CHARACTERIZATION OF THE DYNAMIC VISCOSITY OF CELL CULTURES AND ITS EFFECT ON MIXING PERFORMANCE IN A SPINNER FLASK BIOREACTOR

A version of this chapter has been submitted for publication by Fernando José Cantarero Rivera, Doris D'Souza, Madhu Dhar, and Jiajia Chen to the Biochemical Engineering Journal and is currently under review.

As the first author of this research article, I was the main contributor to Conceptualization, Methodology, Data curation, Investigation, Software, Visualization, and Writing of the manuscript. Dr. Jiajia Chen, as the major professor and corresponding author, contributed to Conceptualization, Investigation, Supervision, Project administration, Funding acquisition, Writing - Reviewing and Editing of the manuscript. The co-authors, also committee members of the Ph.D. program, contributed with lab Materials and space, Supervision, and Reviewing and Editing of the manuscript.

Abstract

Computational fluid dynamics (CFD) models have been developed to simulate cell culturing bioreactors but assume water-like viscosity properties due to significant data gaps. This study characterized the dynamic viscosity of HEK-293 cell cultures and evaluated its effect on mixing performance in a spinner flask bioreactor. Viscosity measurements indicated that the cell culture media, media with microcarriers, and cell cultures presented shear thinning behaviors within the measured shear rate range of 1 to 100 s^{-1}. The viscosity also increased with the microcarrier concentrations and growth of cell culture. The CFD model, incorporating dynamic viscosity data, showed that shear stress and Kolmogorov length profiles are significantly influenced by microcarrier concentrations and cell culture growth. Higher microcarrier concentrations led to higher average shear stress and Kolmogorov values. The cultured HEK-293 cells after seven days of growth also had higher average shear stress and Kolmogorov values than at the day of seeding, indicating an impact caused by the cells' metabolism and biomass. Overall, the results indicated that assuming water-like properties underestimates shear stress and Kolmogorov length scales, especially at zones of lower shear rates due to the observed shear thinning behavior. Thus, careful monitoring of dynamic viscosity of cell cultures and proper control of mixing parameters are critical to deliver the desired mixing conditions for optimized cell growth especially during scale-up production operations.

Keywords: Viscosity, animal cell culture, microcarriers, shear stress, Kolmogorov length, bioreactors.

1 Introduction

Cultivated meat has gained wide interest in academia and food industry due to the potentially significant environmental benefits including reducing agriculture-related pollution and supporting animal welfare (Mattick et al., 2015; Sinke & Odegard, 2021). In addition, cultivated meat is a promising technology to meet increased protein demands; however, for cultivated meat approaches to be feasible, it must be scaled up to industrial proportions where cells are grown in bioreactors at high densities and volumes (e.g., ~20 m^3) (Post & Hocquette, 2017). Although bioreactors of this volume exist, they have mostly been used for bacteria, yeast, or animal cell culture in suspension for biopharmaceutical products and only recently adapted for food products (D. Eibl & Eibl, 2009). The bioreactor design and processing parameters depend greatly on the cell type being cultivated. This has led to the design of various bioreactor types, all with their own advantages and disadvantages (Catapano et al., 2009). Stirred-tank bioreactors are the most widely used bioreactors for suspension cell culture, and microcarriers are typically added to provide a surface for adherent cell types, like myoblasts (Verbruggen et al., 2018). However, the scale up process for adherent cells used for cultivated meat is not straightforward. These cells are sensitive to hydrodynamic shear stress, and exposure to turbulence can damage or even cause cell death (Chisti, 2001; Croughan et al., 1987). Larger volume bioreactors that require more or larger impellers with faster mixing speeds to maintain proper nutrient mixing will lead to a higher chance of exposing these cells to high shear rate zones. Hence, adequate monitoring and implementation of (hydrodynamic environmental and/or mixing) parameters for optimal cell-culture growth conditions is warranted.

Computational fluid dynamics (CFD) simulations are useful tools to characterize the hydrodynamic environment within any bioreactor type with much less experimental time and cost. Many studies have used CFD simulations to understand the mixing characteristics of airlift (McClure et al., 2016; Wadaugsorn et al., 2016), rocking (Öncül et al., 2010; Svay et al., 2020; Zhan et al., 2019), hollow fiber (Menshutina et al., 2020; Mohebbi-Kalhori et al., 2012) and stirred tank bioreactors (Jossen et al., 2018; Verma et al., 2019). However, all these CFD models assume that cell cultures have water-like properties, and this is a common assumption to make due to the significant knowledge gaps on the rheological properties of cell cultures. Several CFD studies for cultivated meat applications also assumed water-like density and viscosity. One such study developed CFD models for a spinner flask and a 20 m^3 stirred tank with varying working volumes and microcarrier solid loads (g/L) in phosphate-buffered saline (PBS) solutions (J. Zhang et al., 2021). Another study used CFD to optimize airlift bioreactor designs as they were scaled up to 300 m^3 to meet mass transfer, mixing, and energy dissipation rates typical for animal cells used for cultivated meat (Li et al., 2020). Furthermore, neither of the studies evaluated the changes in shear stress within the bioreactors; yet both agree this is an important parameter for proper process scale-up. This model simplification of using water-like properties significantly influences the model accuracy, especially at high cell densities and larger scales (Hutmacher and Singh, 2008; Ebrahimi et al., 2019; Ghasemian et al., 2020). Thus, the knowledge gap of dynamic shear-dependent viscosity of cell cultures needs to be filled to improve the CFD modeling accuracy.

Recently, a few studies characterized the rheological properties of cell cultures. Poon (2022) measured the viscosity of RPMI-1640, a cell culture medium commonly used to grow mammalian cells and determined that it had a higher dynamic viscosity than water and had a shear thinning behavior at lower shear rates (0 – 20 s^{-1}). Wyma et al., (2018) evaluated the viscosity of static and stirred L929 (mouse fibroblast) cell cultures after 5 days of growth. They also evaluated how viscosity changed between cell-free media without serum and media with typical 10% serum supplementation without cells. They found that L929 cells in suspension in serum-free culture medium at Day 0 showed non-Newtonian behavior and so did the medium (free of cells) with 10% serum while other samples without cells or serum had a more linear, Newtonian behavior. This means that both cells in suspension and serum supplementation are the main drivers of this non-Newtonian behavior. This study also conducted a quick estimation of the shear stress using the data-fitted Sisko model and the Newtonian model and found that assuming Newtonian behavior underestimates the shear stress significantly, indicating that characterization of dynamic viscosities of cell cultures is necessary. For cultivated meat applications, these reported rheological properties' studies need to be further improved to incorporate the impact of microcarrier concentration which plays a significant role for growth and propagation of animal cell culture (Bodiou et al., 2020; Y. Liu et al., 2022). The presence of these spheres would disrupt the fluid flow inside the bioreactor leading to changes in the viscosity of the bulk fluid. It is known that high concentrations of particles in suspension will impact the bulk fluid viscosity significantly due to increased incidence of particle collisions (Mueller et al., 2010). These changes in viscosity due to the presence of microcarriers would then have an impact on the shear stress and overall bioreactor mixing performance.

Therefore, the objectives of this study were to:

(1) Characterize the shear-dependent dynamic viscosities of cell culture media with varying microcarrier concentrations and dynamic cell cultures (using human embryo kidney (HEK)-293 T cells as a model system) before and after 7 days of growth.

(2) Evaluate the effect of shear-dependent viscosities on CFD modeling of a spinner flask bioreactor.

2 Materials and method

2.1 Cell Culture

Human embryo kidney (HEK)-293T cells were obtained from American Type Culture Collection (ATCC, Manassas, VA). Cells were cultured in Dulbecco's Modified Eagle Medium (DMEM) F-12 supplemented with 10% Fetal Bovine Serum (FBS) (HyClone™, Cytiva, Marlborough, MA). The HEK-293T cells were chosen because they are immortalized cells with rapid proliferation and can be stably cultured at high densities (Schwarz et al., 2020), enabling the characterization of dynamic viscosities. They have been widely used for gene expression and protein production (Fliedl & Kaisermayer, 2011). HEK-293T cells were cultured in T-175 flasks with an initial cell seeding density of roughly, 5×10^3 cells/cm^2 (1×10^6 total cells) and grown in an incubator with 5% CO_2 at 37 °C. Once cells reached 70-80% confluence (5-7 days), they were harvested with standardized cell detachment procedures using10 mL 0.25% Trypsin/EDTA (1×) for 5 min at 37 °C. These cells were then transferred to the sterilized and siliconized spinner flasks. The spinner flasks were siliconized with Sigmacote® to prevent cells and microcarriers from adhering to the walls. The Corning® 125 mL spinner flasks (Corning, Cleveland, TN) were seeded with 1 g of Corning® collagen-coated micro-carriers (360 cm^2 total surface area), prepared following manufacturer's instructions, at an initial working volume of 50 mL growth medium and were allowed to acclimate for one hour before seeding with cells. These collagen-coated microcarriers were used based on having the best results from an attachment screening test against Solohill® collagen-coated, Hillex® II, and FACT III microcarriers. After microcarrier acclimation, HEK-293T cells were added at a seeding concentration of 2×10^4 cells/cm^2 (7.2×10^6 total cells) equivalent to about 15 cells per microcarrier. During the first 24 h, the cells were left unstirred to assist with attachment. After the settling period, the total working volume was brought up to 72 mL to have a similar media volume to surface area ratio as compared to the static flasks and a continuous stirring at 30 rpm was programmed on the MagStir Genie® magnetic stirrer. The final microcarrier concentration was 13.89 g/L.

Sampling and quantification of viable cell concentration in the spinner flask were done following the Solohill ® protocol. A 5 mL sample from the spinner flask was transferred to a 15 mL falcon tube. After the microcarriers settled, the supernatant was removed, and 1 mL of 0.25% Trypsin/EDTA was added to detach the cells from the microcarriers. After trypsinization, the solution was passed through a Fisherbrand ™ 0.70 μm sterile, nylon cell strainer. Complete medium was added slowly through the strainer to rinse off any remaining cells and stop trypsinization. Live cell counts with the trypan blue exclusion method was done on the final strained solution.

2.2 Viscosity measurements

To assess variations in culture media viscosity, the influence of microcarrier concentration, and alterations resulting from cell culture growth, viscosity measurements were carried out. All samples evaluated included DMEM F-12 supplemented with 10% FBS without any microcarriers (referred as 0 g/L from here on), DMEM F-12 supplemented with 10% FBS with different concentrations of microcarriers (5, 10, and 20 g/L), and spinner flask cell cultures (13.89 g/L microcarriers) at day of seeding and after seven days of growth. Samples with media and varying microcarrier concentrations were prepared following the microcarrier manufacturer's instructions in total volumes of 25 mL each. The same volume (25 mL) was extracted directly from the spinner flasks and transferred to separate tubes under aseptic conditions on the specified days. All samples were tested in triplicate at 37 °C using the Discovery Hybrid Rheometer (DHR) 2 (TA Instruments, New Castle, DE, USA) with the DIN concentric cylinders and a Peltier stainless steel cup sample holder. Measurements of the N1 viscosity standard (Cannon Instrument Co., State College, PA, USA) were used to validate measurements. Then, 23 mL of each sample was loaded onto the rheometer. After loading, the bob was lowered to a gap of 5.794 mm. Testing began with a 1-minute pre-shear conditioning step (100 s^{-1}) to properly mix samples before taking viscosity measurements. After conditioning, the sample was exposed to a backward shear rate sweep from 1000 to 1 s^{-1} in a logarithmic ramp with 5 steps per log. The backward shear rate sweep was used to minimize the microcarrier settling during the measurement.

2.3 Numerical simulations

To evaluate the effect of dynamic viscosity of various cell culture (or media) conditions, a three-dimensional (3D) model of a Corning® 125 mL spinner flask with a working volume of 100 mL was developed using COMSOL Multiphysics® 6.1 (COMSOL Inc., Burlington, MA) (**Figure 4.1**). The simulation assumed steady state and used the Reynolds averaged Navier-Stokes (RANS) κ-ε turbulence model to describe the incompressible fluid profile. The RANS equations are expressed as:

$$\rho \boldsymbol{u} \cdot \nabla \boldsymbol{u} = -P\nabla + (\mu + \mu_t)\nabla^2 \boldsymbol{u} \quad \textbf{(4.1)}$$

$$\rho \nabla \cdot \boldsymbol{u} = 0 \quad \textbf{(4.2)}$$

where ρ is the density, $\boldsymbol{u}$ is the velocity magnitude, P is the pressure, and μ is the dynamic viscosity. The κ-ε turbulence model uses two additional transport equations to solve for *k*, turbulent kinetic energy and to solve for *ε*, turbulent dissipation rate, expressed as:

$$\rho \boldsymbol{u} \cdot \nabla k = \nabla \cdot \left(\left(\mu + \frac{\mu_T}{\sigma_k} \right) \nabla k \right) + P_k - \rho\varepsilon \quad \textbf{(4.3)}$$

$$\rho \boldsymbol{u} \cdot \nabla \varepsilon = \nabla \cdot \left(\left(\mu + \frac{\mu_T}{\sigma_\varepsilon} \right) \nabla \varepsilon \right) + C_{\varepsilon 1} \frac{\varepsilon}{k} P_k - C_{\varepsilon 2} \rho \frac{\varepsilon^2}{k} \quad \textbf{(4.4)}$$

where σ_k and σ_ε are the turbulent Prandtl numbers for *k* and *ε*, respectively, and μ_t is the turbulent viscosity modeled as:

$$\mu_t = \rho C_\mu \frac{k^2}{\varepsilon} \quad \textbf{(4.5)}$$

This model uses five turbulence constants $C_\mu = 0.09$, $C_{\varepsilon 1} = 1.44$, $C_{\varepsilon 2} = 1.92$, $\sigma_k = 1$, and $\sigma_\varepsilon = 1.3$. These were determined from experimental data in simple flows (Launder & Spalding, 1974; Wilcox, 2006). The COMSOL κ-ε turbulence model has been widely used for suspension bioreactors (Borys et al., 2019; Freiberger et al., 2022) and has been validated for spinner flasks with light attenuation (Delafosse et al., 2018) and particle image velocimetry (Berry et al., 2016). A rotating domain was defined in the model (highlighted in **Figure 4.1**b) to account for the impeller's movement. Three mixing speeds were evaluated; 30 rpm to match our experimental conditions and recommended manufacturer setting for the microcarriers used, 60 rpm to match the PIV validation experiments (Berry et al., 2016) and experimental conditions from Yang et al. (2019), although the microcarriers used in that study are different from those used here; and 90 rpm as a more severe scenario to showcase the impact at higher mixing speeds which would generate more severe conditions overall.

A baseline model with commonly used water-like constant values for density (995 kg/m^3) and viscosity (0.659 mPa·s) at 37°C, as described before (Poon, 2022), was developed and compared with other models using the measured dynamic shear-dependent viscosities at various cell culture conditions. The density for all media samples was defined as 1009 kg/m^3 as determined by Poon (2022). The measured viscosity values for all samples were directly incorporated into the simulations as a function of shear rate. The model of the spinner flask was solved with the steady-state study called “frozen rotor”. The frozen rotor step computes the velocity, pressure, and turbulence within the system by keeping the rotating domains frozen in position and accounting for the rotation by including centrifugal and Coriolis forces (COMSOL). The best mesh to use (**Figure 4.1**c) was determined with a mesh independence study for shear stress and Kolmogorov length at 30, 60, and 90 rpm (**Figure 4.2**). The percentage change for shear stress was <1% between all mesh levels for all speeds while for Kolmogorov length, it reached <1% between the 3rd (1.23 million elements) and the 4th mesh (3.39 million elements). Thus, the 3rd mesh level was used for all simulations, where the element size ranged from a minimum of 0.0069 mm to a maximum of 0.2450 mm. Quality analysis based on skewness, which has a range from 0–1, where 1 represents ideal, undeformed mesh elements, showed that the average element quality was 0.6957.

2.4 Statistical analysis/evaluation of results

All viscosity measurements were taken at 37 °C and three replicates were performed for all samples. The shear stress and Kolmogorov profiles predicted by the CFD simulations with measured viscosities were compared against the models using constant water-like properties. The Root Mean Square Error (RMSE) metric was employed for this purpose was calculated as:

$$RMSE = \sqrt{\frac{1}{n}\sum_{i=1}^{n}|Sample_i - Water_i|^2} \tag{4.6}$$

where n is the number of nodal points used to discretize the simulation space, $Sample_i$ and $Water_i$ are the nodal shear stress and Kolmogorov length values for the simulations using the viscosity of the current sample being evaluated and assuming constant water viscosity, respectively. These statistical measures provided a quantitative evaluation of the accuracy and precision of the CFD predictions in capturing the dynamic, measured properties in contrast to the baseline constant water conditions.

3 Results & discussion

3.1 Cell Culture

3.1.1 Static cell culture growth characteristic

The HEK-293T cells that were seeded in T-175 flasks at an initial concentration of 1×10^6 total cells (5.71×10^3 cells/cm^2) were successfully passaged 20 times. The flasks reached confluency after 5-7 days of growth/incubation. Their average cell growth characteristics are shown in **Table 4.1**.

3.1.2 Spinner flask culture

The HEK-293T cells were cultured in spinner flasks with Corning® collagen-coated microcarriers. Initial seeding concentration was 2×10^4 cells/cm^2 for all experiments, similar to the concentration used in an earlier study, with 1.5 to 2.5×10^4 cells/cm^2, which reported up to 95% attachment with continuous mixing (Yang et al., 2019). Spinner flasks reached $8.59 \pm 0.39 \times 10^4$ cells/cm^2 or an equivalent of $4.30 \pm 0.19 \times 10^5$ cells/mL after seven days of growth. This final cell yield is lower than that obtained from the static cultures and therefore not as high as expected. Yang et al. (2019) cultured HEK-293T cells from an initial cell concentration of 1.5×10^4 cells/cm^2 to a maximum cell concentration of 1.92×10^5 cells/cm^2. The slightly higher yield obtained by Yang et al. 2019 may be due to their use of 3 g/L of Cytodex-1 microcarriers which have a surface area of 4400 cm^2/g, translating to a surface area of 13.2 cm^2/mL, which is 2.64 times higher than that used in our spinner flask cultures (5 cm^2/mL). Their faster mixing regime of 60 rpm, positive charged microcarriers, and slight differences in cell line growth behaviors may have also contributed to the difference in cell yields.

3.2 Viscosity measurements

Viscosity measurements of N1 standard are shown in **Figure 4.3**, serving to validate the accuracy and reliability of the viscosity measurements of all samples. As can be observed, the measured viscosity of the N1 standard was about 0.737 ± 0.028 mPa·s between the shear rate range of 1 and 100 s^{-1}, which closely aligns to the expected viscosity of 0.729 mPa·s, as specified by the manufacturer, indicating accurate measurement in this shear rate range. Out of this shear rate range, considerable difference was observed between the measured and manufacturer values for the N1 standard. The inaccuracies above this range may be due to the formation of secondary flows within the sample and the large variation of measurements below this range are due to lack of sensitivity of the instrument, especially considering all samples have relatively low viscosities (Hughes et al., 1998). Thus, the viscosity measurements for the cell culture and media samples in this study were measured between 1 and 100 s^{-1}.

The impact of microcarrier concentration on fresh media viscosity is shown in **Figure 4.4**a, viscosity measurements for the 5 g/L sample follow that of 10 g/L sample closely and are therefore not shown. The microcarrier concentrations used here represent those commonly used for lab-scale cell culture experiments which range from 3 – 15 g/L (Cytiva, 2021). The results show that the 0 g/L sample (DMEM F-12 only) had a shear thinning behavior in the range studied with higher overall apparent viscosity values compared to water. The shear thinning behavior indicates that the viscosity values will be large at low shear rates and will decrease to a stable, more linear region after reaching higher shear rates (Cross, 1979). Higher microcarrier concentrations led to higher overall viscosity values and an even more pronounced shear thinning behavior. The sample with 20 g/L had the highest shear rate dependent viscosity values within the 1 - 100 s^{-1} range. It is known that high concentrations of particles in suspension will impact the bulk fluid viscosity significantly due to increased incidence of particle collisions (Mueller et al., 2010). Stickel and Powell (2005) found that shear thinning behavior is observable at solid fractions as low as 0.10. Another study found similar shear thinning behavior using suspension of spheres at varying concentrations (Mueller et al., 2010). They described that the dependence of viscosity on particle concentration becomes more noticeable at higher concentrations and the increase in overall viscosity is due to the collisions between particles. These collisions generate friction and increase the resistance to flow of the whole fluid.

The viscosity values of cell cultures growing in a spinner flask at day 0 and day 7 with a microcarrier concentration of 13.89 g/L are compared to water and DMEM F-12 without cells or microcarriers and shown in **Figure 4.4**b. The samples from the spinner flask have higher viscosity values and a more pronounced shear thinning behavior in the studied range than DMEM by itself, which is expected since the spinner flask has a 13.89 g/L microcarrier concentration and varied cell concentrations. The spinner flask sample after seven days of growth had the most pronounced shear thinning behavior and highest viscosity values comparable to other cell culture conditions. The depletion of nutrients in the media and production of metabolites in the spinner flask as the cell culture grows could explain the difference in viscosity profiles between the spinner flask samples. The cell culture sample after cell seeding had fresh DMEM, which typically contains high concentrations of glucose, amino acids, vitamins and is supplemented with fetal bovine serum (FBS) at 10% to use for animal cell culture growth. This serum provides a combination of proteins and growth factors essential for cell attachment and growth (Freshney, 2010). A recent study found that higher concentrations of FBS in DMEM and RPMI cell culture media increased the dynamic viscosity of the fluid by up to ~60% when compared to water dynamic viscosity (Poon, 2022). However, it is well known that FBS is highly variable between batches and therefore the impact of serum supplementation on the cell culture viscosity might need to be re-examined before starting every new culture (Masters & Stacey, 2007). Additionally, as the cells grow, they will consume glucose and produce lactic acid as a metabolite. Lactic acid solutions are known to have lower viscosity than glucose solutions with similar concentration (w/w%) at similar temperatures (Simion et al., 2017; Telis et al., 2007), that can affect the overall viscosity during growth.

3.3 CFD modeling

The dynamic viscosity values measured with the DHR-2 rheometer were imported into the COMSOL model which then used the κ-ε turbulence model to simulate the hydrodynamic profile within the spinner flask for all samples. The model used two commonly used mixing speeds in spinner flasks (30 and 60 rpm) and a higher mixing speed (90 rpm) for better understanding of the underlying phenomena. The effect of the measured dynamic viscosity of various samples on shear stress and Kolmogorov length profiles are comprehensively evaluated and compared against the classical assumption of using water-like viscosity.

3.3.1 Fluid shear stress and Kolmogorov length profiles at 60 rpm

The shear stress profiles generated inside the spinner flask with different viscosities at 60 rpm are shown in **Figure 4.5**. Using constant water-like viscosity led to lower shear stress values in all locations inside the spinner flask compared to all other samples. As discussed in the previous section, the slight shear thinning behavior observed in the culture media is exacerbated by increasing the microcarrier concentration and as the cell culture progresses. In the CFD profiles, the effect of the shear thinning behavior can be observed as the shear stress values increased in the bulk fluid, or lower shear rate zones, with increasing microcarrier concentration and after seven days of cell culture while the maximum values did not change much. The zones with the highest shear stress values, as expected, where found to be around the impeller, which were considerably lower in the model using water viscosity compared to all others.

3.3.2 Effect of culture media and microcarrier concentration on shear stress and Kolmogorov length

Figure 4.6a shows the effect of culture media and microcarrier concentrations on the volumetric average shear stress within the bioreactor at three mixing speeds of 30, 60, and 90 rpm. The error bars indicate one standard deviation of the shear stress. Shear stress is calculated as:

$$\tau = \mu \cdot \dot{\gamma} \qquad \textbf{(4.7)}$$

where τ is shear stress, μ is the fluid's dynamic viscosity, and $\dot{\gamma}$ is the shear strain rate. Higher viscosity values and shear rates will lead to a higher shear stress. In all models, the average shear stress also increased with the rotation speed, as expected. However, at all mixing speeds, the average shear stress over the whole bioreactor increased with higher microcarrier concentrations. The lowest average shear stress was observed in the model with water and the highest average shear stress was found in the model with culture media with 20 g/L microcarrier.

Figure 4.6b, c, and d show the effect of culture media and microcarrier concentrations on the volumetric distributions of shear stress within the bioreactor at 30, 60, and 90 rpm, respectively. Note that the upper limits of the shear stress values were not shown in the figures for better comparison of the most frequent shear stress values. For all three mixing speeds, as the microcarrier concentration in the cell culture media increased, a higher percentage of the bioreactor volume experienced higher shear stress values. Furthermore, higher mixing speeds (higher shear rates) resulted in higher shear stress values with wider ranges as well, indicating more heterogeneous shear stress distribution. At all mixing speeds, the widest, most heterogeneous profile range was obtained by the 0 g/L sample (0.54 to 521.54 mPa at 30 rpm, 0.60 to 1907.80 mPa at 60 rpm, and 0.90 to 4183.00 mPa at 90 rpm) while the lowest range was obtained by water at all mixing speeds (0.05 to 176.63 mPa at 30 rpm, 0.12 to 383.36 mPa at 60 rpm, and 0.15 to 598.96 mPa at 90 rpm). The 20 g/L sample, which had the largest average values as discussed previously, had ranges that fell between the 0 g/L sample and water (0.93 to 455.54 mPa at 30 rpm, 1.65 to 1516.90 at 60 rpm and 3.21 to 3006.20 mPa at 90 rpm). The difference observed between culture media with different microcarrier concentrations and water was attributed to the higher dynamic viscosity values and the shear thinning behavior caused by the increase in microcarrier concentration.

These results show that the overall shear stress within the bioreactor increased with the microcarrier concentration. These results are similar to those presented by Liu et al. (2022b) who found that the viscosity of solid-liquid mixtures increased with increasing particle concentration. Although using a higher concentration of microcarrier could provide more surface area for cells to grow, the increased shear stress may have a negative effect on the cell growth performance (Gareau et al., 2014; Hu et al., 2011). Furthermore, the shear thinning behavior found indicates that in areas of lower shear rates inside the bioreactor, the shear stress would be considerably underestimated if constant water-like properties are assumed. Thus, it is critical to choose proper microcarrier concentrations to balance the influence of surface area and shear stress conditions.

Figure 4.7a shows the effect of culture media and microcarrier concentrations on the Kolmogorov eddy length within the bioreactor at three mixing speeds (30, 60, and 90 rpm). The Kolmogorov eddy length is calculated as:

$$\eta = \left(\frac{v^3}{\varepsilon}\right)^{\frac{1}{4}} = \left(\frac{\mu/\rho}{\varepsilon}\right)^{\frac{1}{4}} \tag{4.8}$$

where v and ρ are the kinematic viscosity and density of the fluid, respectively; ε is the turbulent energy dissipation rate. Higher dynamic viscosity values and lower energy dissipation rate (mixing speed) lead to larger Kolmogorov length scale. The simulation results showed that the average Kolmogorov values increased with increasing microcarrier concentration and decreased with the mixing speed.

Figure 4.7b, c, and d show the effect of microcarrier concentrations in culture media on the volumetric distributions of Kolmogorov eddy length within the bioreactor at 30, 60, and 90 rpm, respectively. At all mixing speeds, the additional particles led to a larger range of Kolmogorov length values but also a more homogeneously distributed profile, seen by the reduced percentage of the bioreactor that presents a single value. At all mixing speeds, the smallest Kolmogorov eddy length range was obtained by water (0.08 to 0.37 mm at 30 rpm, 0.04 to 0.26 mm at 60 rpm, and 0.03 to 0.21 mm at 90 rpm), while the largest range was obtained by the 20 g/L sample (0.10 to 2.83 mm at 30 rpm, 0.07 to 2.33 mm at 60 rpm, and 0.05 to 1.82 mm at 90 rpm). Nevertheless, the most important value in this case is the minimum Kolmogorov eddy length because eddies that are about the same size or smaller than the cells being cultivated can cause significant damage or even cause cell death (Chisti, 2001; Croughan et al., 1987). This study showed that increasing mixing speeds and lower microcarrier concentrations allowed for lower minimum Kolmogorov length values. This further emphasizes the importance of optimizing the processing parameters (e.g., mixing and microcarrier) in cell culturing, especially considering that the opposite trend was seen for shear stress where lower microcarrier concentrations generated lower average shear stresses, and therefore less possible damage to the cells.

These results highlight the considerable difference between using constant water viscosity against properly measuring the dynamic viscosity depending on microcarrier concentration. The shear thinning behavior found for all samples would suggest that the Kolmogorov eddy lengths would be overestimated in areas of lower shear rates inside the bioreactor if constant water-like properties are assumed instead. This should be taken into consideration when determining what microcarriers to use and their concentration. For example, larger microcarriers like the Cytodex-1 are typically used at concentrations of 3 g/L (Yang et al., 2019) while smaller microcarriers such as the collagen-coated used in this study require much higher concentrations to provide the same total surface area. For example, a spinner flask with 100 mL working volume and 3 g/L of Cytodex-1 would provide a total of 900 cm^2. A concentration of 25 g/L is needed to reach this same total surface area with the collagen-coated microcarriers. This higher concentration of suspended particles was shown to lead to higher average shear stress levels while the minimum Kolmogorov length is unaffected. Thus, from the Kolmogorov length point of view, the increase of microcarrier concentrations may not affect the cell growth as much as shear stress in this case.

The shear stress and Kolmogorov length simulation results using culture media with different microcarrier concentrations were compared with that assuming water-like properties by calculating the RMSE values to characterize the potential errors in assuming water-like properties in cell culture media (**Table 4.2**). At all mixing speeds, the RMSE values increased with the microcarrier concentrations, indicating increased errors in assuming water-like viscosity in CFD modeling instead of using the properly measured viscosity values. The introduced error in predicting shear stress and Kolmogorov length using water-like viscosity may influence the bioreactor design and/or control for optimized cell growth.

3.3.3 Effect of growing cell culture on shear stress and Kolmogorov length

The effect of growing cell culture (cell concentrations and media conditions) on shear stress and Kolmogorov length are shown in **Figure 4.8** and **Figure 4.9**, respectively. The results indicated that the average volumetric shear stress (**Figure 4.8**a) and Kolmogorov length (**Figure 4.9**a) values within the spinner flask increased as the cell culture progressed from the day of seeding to seven days of growth, which was due to the increased dynamic viscosity values with cell growth. The smaller values in simulation using water indicated a considerable underestimation of shear stress when using constant water viscosity. **Figure 4.8**b, c, and d show the effect of cell culture growth on the volumetric distributions of shear stress within the bioreactor at 30, 60, and 90 rpm, respectively. The most frequent shear stress values in the bioreactor are higher as the growth of cell culture progresses. The overall distribution of values is unaffected although the range is slightly larger when using the cell culture viscosity values for the simulations. At all mixing speeds, the largest shear stress range was generated using the viscosity of cell culture at day of seeding (0.41 to 484.27 mPa at 30 rpm, 0.57 to 2316.40 mPa at 60 rpm, and 0.59 to 3185.60 mPa at 90 rpm). Constant water viscosity generated the smallest range of shear stresses (0.05 to 176.63 mPa at 30 rpm, 0.12 to 383.36 mPa at 60 rpm, and 0.15 to 598.96 mPa at 90 rpm).

Figure 4.9b, c, and d show the effect of cell culture state on the volumetric distributions of Kolmogorov length values within the bioreactor at 30, 60, and 90 rpm, respectively. As the cell culture progresses, the Kolmogorov values are more homogeneously spread out compared to water. As the mixing speed increases, a larger percentage of the bioreactor presents lower Kolmogorov values. The lowest minimum values at all mixing speeds follow the same trend as with the microcarrier concentrations. Water generated the lowest minimum values at all mixing speeds (0.08 mm at 30 rpm, 0.04 mm at 60 rpm, and 0.03 mm at 90 rpm) while for cell culture at seeding and after 7 days of growth/culture the minimum was the same (0.10 mm at 30 rpm, 0.07 mm at 60 rpm, and 0.05 mm at 90 rpm). As mentioned previously, if the minimum Kolmogorov length values approach the cell size (0.01 – 0.02 mm), then it could lead to cell damage and death. Higher mixing speeds could generate such values; therefore, care must be taken when scaling up growth of cell cultures and increasing mixing speed to maintain similar nutrient and gases mixing conditions.

These simulation results were again further evaluated by using the RMSE to describe how different they were from the results obtained by using constant water viscosity values (**Table 4.3**). The values show that the shear stress and Kolmogorov length profiles generated by the measured spinner flask viscosity at day of seeding and after seven days of growth/culture are considerably different from those generated by using constant water values and this error increases as mixing speed increases as well.

These results suggest that, during cell culturing process, a constant mixing speed would generate an increasing shear stress within the bioreactor that may influence the cell growth performance. Thus, the shear stress generated within dynamic cell cultures should be closely monitored and the bioreactor may need dynamic control of mixing conditions to ensure proper/adequate cell growth/differentiation environments. For example, preadipocytes exposed to one hour of 1 Pa shear stress reduced lipid accumulation, leading to a delayed maturation for these cells (Choi et al., 2017). Another study showed that differentiation of C2C12 (mouse muscle cells) from myoblasts into myotubes was greatly dependent on shear stress (Naskar et al., 2017). When the cells were exposed to only 16 mPa of shear stress, the myogenic markers were upregulated up to 50x their regular expression in static conditions. Furthermore, mouse embryo stem cells exposed to shear stress levels of 150 mPa for 24 hours had better proliferation rates than their static counterparts while those exposed to 500 mPa for 24 hours began differentiating into endothelial cell lineage (Yamamoto et al., 2005).

3.4 Discussion

This study demonstrated that the viscosity of cell cultures is highly dependent on the microcarrier concentrations, and on cell proliferation. Significantly higher viscosity values and shear-thinning behavior were observed for the various cell culture conditions compared to the water sample. Therefore, the use of Newtonian water-like viscosity could significantly under-estimate the shear stress and Kolmogorov length scales, as shown in the modeling results. The underestimation of shear stress and Kolmogorov length in CFD models using water-like properties will mislead the designs and control of bioreactors for desired cell culturing performance.

We expect this difference in simulation results to exacerbate at the industrial scale since larger stirred bioreactors are known to generate a more heterogeneous flow profile during scale-up. Shear stress and Kolmogorov length are two important parameters to consider when scaling up since they directly correlate to cell damage, death, or metabolic reactions (R. Eibl et al., 2009). Other parameters used for scale-up include impeller tip speed, impeller Reynolds number, and mean power input per volume, as they help maintain a similar hydrodynamic environment in terms of shear stress and mixing performance (Catapano et al., 2009). The challenge lies in the fact that only one of these scale-up parameters can be kept constant at a time (Kreitmayer et al., 2023). This can lead to a very iterative process of optimization for bioreactor scale-up which can be significantly expensive and easily avoidable if proper models are developed. These scale-up parameters must be controlled even more for cultivated meat applications since the animal cells required for cultivated meat tend to be more unstable than those used for tissue engineering applications (Post, 2012). The muscle stem cells are highly sensitive to mechanical stimulation such as shear stress and matrix stiffness and this can ultimately affect their differentiation (G. Zhang et al., 2020). Thus, it is necessary to perform online bioreactor performance characterization and incorporate dynamic bioreactor control strategies to provide proper cell culturing conditions for best cell growth behavior.

The results obtained for this study can be expanded in multiple directions for better applications into the cultivated meat process. For example, as the process is scaled up, paddle impellers are less common and replaced by other designs such as Rushton or by multiple impellers which will all generate different flow profiles (Joshi et al., 2011a, 2011b). Using properly measured dynamic cell culture viscosity values instead of constant water-like properties will lead to a more accurate model for bioreactor design and control. Furthermore, the muscle cells required for cultivated meat are anchorage-dependent and is the reason for the common use of microcarriers. As mentioned previously, there are many types of microcarriers with different types of bead material, surface coating, surface charge, porosity, and size. All of these parameters influence the number of particle-particle interactions and could potentially change the cell culture's viscous behavior (Konijn et al., 2014). In this study, HEK-293 cells were used since they are a well-established cell line, however, cell lines for cultivated meat applications are not as well-established and tend to present some phenotypical and genetic drift after continuous culture (R. Eibl et al., 2009). This will affect their specific metabolism which could play a significant role in viscosity values due to nutrient consumption and metabolite production rates being different for each cell type. Finally, many efforts are focused on developing serum-free media mainly for cost and sustainability reasons (Kolkmann et al., 2020; Messmer et al., 2022; Stout et al., 2022). In these studies, serum is replaced with a combination of proteins and growth factors from various sources. The lack of serum could change the fluid's viscous behavior significantly as it has been shown to have a shear thinning behavior (Wyma et al., 2018). Therefore, the process and models must be adapted correspondingly if this type of media is used.

4 Conclusions

This study characterized the dynamic viscosity of cell culture media with varying microcarrier concentrations and of dynamic cell cultures after 7 days of the culturing process and evaluated the effect of dynamic viscosity on shear stress and Kolmogorov length profiles in a spinner flask bioreactor. Different from water, the cell culture media (DMEM with 10% FBS supplementation) had higher viscosity values with a shear thinning behavior, which was intensified with increasing microcarrier concentration. The higher viscosity values and shear thinning behavior were further intensified with the cell culturing process along with nutrient consumption, metabolite production, and cell growth. The dynamic change of viscosity values significantly influenced the simulated shear stress and Kolmogorov eddy length values within the bioreactors. Our findings indicate that the assumption of water-like properties in cell culture bioreactors under-estimates the shear stress and Kolmogorov eddy length values predictions. The dynamic monitoring of bioreactors and control of mixing parameters are critical to provide proper processing conditions for optimal cell growth.

Acknowledgements

This work was supported by the AI Tennessee Initiative and in part by the Student/Faculty Research Award from the University of Tennessee, Knoxville.

REFERENCES

Berry, J. D., Liovic, P., Šutalo, I. D., Stewart, R. L., Glattauer, V., & Meagher, L. (2016). Characterisation of stresses on microcarriers in a stirred bioreactor. *Applied Mathematical Modelling*, *40*(15), 6787–6804. https://doi.org/10.1016/j.apm.2016.02.025

Bodiou, V., Moutsatsou, P., & Post, M. J. (2020). Microcarriers for Upscaling Cultured Meat Production. *Frontiers in Nutrition*, *7*. https://doi.org/10.3389/fnut.2020.00010

Borys, B. S., Le, A., Roberts, E. L., Dang, T., Rohani, L., Hsu, C. Y.-M., Wyma, A. A., Rancourt, D. E., Gates, I. D., & Kallos, M. S. (2019). Using computational fluid dynamics (CFD) modeling to understand murine embryonic stem cell aggregate size and pluripotency distributions in stirred suspension bioreactors. *Journal of Biotechnology*, *304*, 16–27. https://doi.org/10.1016/j.jbiotec.2019.08.002

Catapano, G., Czermak, P., Eibl, R., Eibl, D., & Pörtner, R. (2009). Bioreactor Design and Scale-Up. In R. Eibl, D. Eibl, R. Pörtner, G. Catapano, & P. Czermak (Eds.), *Cell and Tissue Reaction Engineering: With a Contribution by Martin Fussenegger and Wilfried Weber* (pp. 173–259). Springer. https://doi.org/10.1007/978-3-540-68182-3_5

Chisti, Y. (2001). Hydrodynamic Damage to Animal Cells. *Critical Reviews in Biotechnology*, *21*(2), 67–110. https://doi.org/10.1080/20013891081692

Choi, J., Lee, S. Y., Yoo, Y.-M., & Kim, C. H. (2017). Maturation of Adipocytes is Suppressed by Fluid Shear Stress. *Cell Biochemistry and Biophysics*, *75*(1), 87–94. https://doi.org/10.1007/s12013-016-0771-4

Cross, M. M. (1979). Relation between viscoelasticity and shear-thinning behaviour in liquids. *Rheologica Acta*, *18*(5), 609–614. https://doi.org/10.1007/BF01520357

Croughan, M. S., Hamel, J.-F., & Wang, D. I. C. (1987). Hydrodynamic effects on animal cells grown in microcarrier cultures. *Biotechnology and Bioengineering*, *29*(1), 130–141. https://doi.org/10.1002/bit.260290117

Cytiva. (2021). *Microcarrier Cell Culture Principles and Methods*. Cytiva Handbooks. https://www.cytivalifesciences.com/en/us/support/handbooks

Delafosse, A., Loubière, C., Calvo, S., Toye, D., & Olmos, E. (2018). Solid-liquid suspension of microcarriers in stirred tank bioreactor – Experimental and numerical analysis. *Chemical Engineering Science*, *180*, 52–63. https://doi.org/10.1016/j.ces.2018.01.001

Ebrahimi, M., Tamer, M., Villegas, R. M., Chiappetta, A., & Ein-Mozaffari, F. (2019). Application of CFD to Analyze the Hydrodynamic Behaviour of a Bioreactor with a Double Impeller. *Processes*, *7*(10), 694. https://doi.org/10.3390/pr7100694

Eibl, D., & Eibl, R. (2009). Bioreactors for Mammalian Cells: General Overview. In R. Eibl, D. Eibl, R. Pörtner, G. Catapano, & P. Czermak, *Cell and Tissue Reaction Engineering* (pp. 55–82). Springer Berlin Heidelberg. https://doi.org/10.1007/978-3-540-68182-3_3

Eibl, R., Eibl, D., Pörtner, R., Catapano, G., & Czermak, P. (2009). *Cell and Tissue Reaction Engineering*. Springer Berlin Heidelberg. https://doi.org/10.1007/978-3-540-68182-3

Fliedl, L., & Kaisermayer, C. (2011). Transient gene expression in HEK293 and vero cells immobilised on microcarriers. *Journal of Biotechnology*, *153*(1), 15–21. https://doi.org/10.1016/j.jbiotec.2011.02.007

Freiberger, F., Budde, J., Ateş, E., Schlüter, M., Pörtner, R., & Möller, J. (2022). New Insights from Locally Resolved Hydrodynamics in Stirred Cell Culture Reactors. *Processes*, *10*(1), Article 1. https://doi.org/10.3390/pr10010107

Freshney, R. I. (2010). *Culture of animal cells: A manual of basic technique and specialized applications*. Wiley-Blackwell.

Gareau, T., Lara, G. G., Shepherd, R. D., Krawetz, R., Rancourt, D. E., Rinker, K. D., & Kallos, M. S. (2014). Shear stress influences the pluripotency of murine embryonic stem cells in stirred suspension bioreactors. *Journal of Tissue Engineering and Regenerative Medicine*, *8*(4), 268–278. https://doi.org/10.1002/term.1518

Ghasemian, M., Layton, C., Nampe, D., zur Nieden, N. I., Tsutsui, H., & Princevac, M. (2020). Hydrodynamic characterization within a spinner flask and a rotary wall vessel for stem cell culture. *Biochemical Engineering Journal*, *157*, 107533. https://doi.org/10.1016/j.bej.2020.107533

Hu, W., Berdugo, C., & Chalmers, J. J. (2011). The potential of hydrodynamic damage to animal cells of industrial relevance: Current understanding. *Cytotechnology*, *63*(5), 445–460. https://doi.org/10.1007/s10616-011-9368-3

Hughes, J. P., Davies, J. M., & Jones, T. E. R. (1998). Concentric cylinder end effects and fluid inertia effects in controlled stress rheometry: Part I: numerical simulation. *Journal of Non-Newtonian Fluid Mechanics*, *77*(1), 79–101. https://doi.org/10.1016/S0377-0257(97)00102-X

Hutmacher, D. W., & Singh, H. (2008). Computational fluid dynamics for improved bioreactor design and 3D culture. *Trends in Biotechnology*, *26*(4), 166–172. https://doi.org/10.1016/j.tibtech.2007.11.012

Joshi, J. B., Nere, N. K., Rane, C. V., Murthy, B. N., Mathpati, C. S., Patwardhan, A. W., & Ranade, V. V. (2011a). CFD simulation of stirred tanks: Comparison of turbulence models. Part I: Radial flow impellers. *The Canadian Journal of Chemical Engineering, 89*(1), 23–82. https://doi.org/10.1002/cjce.20446

Joshi, J. B., Nere, N. K., Rane, C. V., Murthy, B. N., Mathpati, C. S., Patwardhan, A. W., & Ranade, V. V. (2011b). CFD simulation of stirred tanks: Comparison of turbulence models (Part II: Axial flow impellers, multiple impellers and multiphase dispersions). *The Canadian Journal of Chemical Engineering*, *89*(4), 754–816. https://doi.org/10.1002/cjce.20465

Jossen, V., Eibl, R., Kraume, M., & Eibl, D. (2018). Growth Behavior of Human Adipose Tissue-Derived Stromal/Stem Cells at Small Scale: Numerical and Experimental Investigations. *Bioengineering*, *5*(4). https://doi.org/10.3390/bioengineering5040106

Julaey, M., Hosseini, M., & Amani, H. (2016). Stem Cells Culture Bioreactor Fluid Flow, Shear Stress and Microcarriers Dispersion Analysis Using Computational Fluid Dynamics. *Journal of Applied Biotechnology Reports*, *3*(2), 425–431. http://www.biotechrep.ir/article_69217.html

Kolkmann, A. M., Post, M. J., Rutjens, M. A. M., van Essen, A. L. M., & Moutsatsou, P. (2020). Serum-free media for the growth of primary bovine myoblasts. *Cytotechnology*, *72*(1), 111–120. https://doi.org/10.1007/s10616-019-00361-y

Konijn, B. J., Sanderink, O. B. J., & Kruyt, N. P. (2014). Experimental study of the viscosity of suspensions: Effect of solid fraction, particle size and suspending liquid. *Powder Technology*, *266*, 61–69. https://doi.org/10.1016/j.powtec.2014.05.044

Kreitmayer, D., Gopireddy, S. R., Aki, Y., Nonaka, K., Urbanetz, N. A., & Gutheil, E. (2023). Scale-up analysis of geometrically dissimilar single-use bioreactors. *Biotechnol Bioeng*. https://doi.org/10.1002/bit.28529

Launder, B. E., & Spalding, D. B. (1974). The numerical computation of turbulent flows. *Computer Methods in Applied Mechanics and Engineering*, *3*(2), 269–289. https://doi.org/10.1016/0045-7825(74)90029-2

Li, X., Zhang, G., Zhao, X., Zhou, J., Du, G., & Chen, J. (2020). A conceptual air-lift reactor design for large scale animal cell cultivation in the context of in vitro meat production. *Chemical Engineering Science*, *211*, 115269. https://doi.org/10.1016/j.ces.2019.115269

Liu, Y., Wang, R., Ding, S., Deng, L., Zhang, Y., Li, J., Shi, Z., Wu, Z., Liang, K., Yan, X., Liu, W., & Du, Y. (2022). Engineered meatballs via scalable skeletal muscle cell expansion and modular micro-tissue assembly using porous gelatin micro-carriers. *Biomaterials*, *287*, 121615. https://doi.org/10.1016/j.biomaterials.2022.121615

Liu, Z., Zhang, R., Li, L., Wang, Y., Jiang, X., Zhang, C., Yin, H., Huang, S., & Qu, X. (2022). Prediction of the viscosity of solid–liquid mixtures using a virtual viscometer based on computational fluid dynamics. *Archive of Applied Mechanics*, *92*(12), 3769–3779. https://doi.org/10.1007/s00419-022-02261-8

Masters, J. R., & Stacey, G. N. (2007). Changing medium and passaging cell lines. *Nature Protocols*, *2*(9), 2276–2284. https://doi.org/10.1038/nprot.2007.319

Mattick, C. S., Landis, A. E., Allenby, B. R., & Genovese, N. J. (2015). Anticipatory Life Cycle Analysis of In Vitro Biomass Cultivation for Cultured Meat Production in the United States. *Environmental Science & Technology*, *49*(19), 11941–11949. https://doi.org/10.1021/acs.est.5b01614

McClure, D. D., Kavanagh, J. M., Fletcher, D. F., & Barton, G. W. (2016). Characterizing bubble column bioreactor performance using computational fluid dynamics. *Chemical Engineering Science*, *144*, 58–74. https://doi.org/10.1016/j.ces.2016.01.016

Menshutina, N. V., Guseva, E. V., Safarov, R. R., & Boudrant, J. (2020). Modelling of hollow fiber membrane bioreactor for mammalian cell cultivation using computational hydrodynamics. *Bioprocess and Biosystems Engineering*, *43*(3), 549–567. https://doi.org/10.1007/s00449-019-02249-9

Messmer, T., Klevernic, I., Furquim, C., Ovchinnikova, E., Dogan, A., Cruz, H., Post, M. J., & Flack, J. E. (2022). A serum-free media formulation for cultured meat production supports bovine satellite cell differentiation in the absence of serum starvation. *Nature Food*, *3*(1), Article 1. https://doi.org/10.1038/s43016-021-00419-1

Mohebbi-Kalhori, D., Behzadmehr, A., Doillon, C. J., & Hadjizadeh, A. (2012). Computational modeling of adherent cell growth in a hollow-fiber membrane bioreactor for large-scale 3-D bone tissue engineering. *Journal of Artificial Organs*, *15*(3), 250–265. https://doi.org/10.1007/s10047-012-0649-1

Mueller, S., Llewellin, E. W., & Mader, H. M. (2010). The rheology of suspensions of solid particles. *Proceedings of the Royal Society A: Mathematical, Physical and Engineering Sciences*, *466*(2116), 1201–1228. https://doi.org/10.1098/rspa.2009.0445

Naskar, S., Kumaran, V., & Basu, B. (2017). On The Origin of Shear Stress Induced Myogenesis Using PMMA Based Lab-on-Chip. *ACS Biomaterials Science & Engineering*, *3*(6), 1154–1171. https://doi.org/10.1021/acsbiomaterials.7b00206

Öncül, A. A., Kalmbach, A., Genzel, Y., Reichl, U., & Thévenin, D. (2010). Characterization of flow conditions in 2 L and 20 L wave bioreactors® using computational fluid dynamics. *Biotechnology Progress*, *26*(1), 101–110. https://doi.org/10.1002/btpr.312

Poon, C. (2022). Measuring the density and viscosity of culture media for optimized computational fluid dynamics analysis of in vitro devices. *Journal of the Mechanical Behavior of Biomedical Materials*, *126*, 105024. https://doi.org/10.1016/j.jmbbm.2021.105024

Post, M. J. (2012). Cultured meat from stem cells: Challenges and prospects. *Meat Science*, *92*(3), 297–301. https://doi.org/10.1016/j.meatsci.2012.04.008

Post, M. J., & Hocquette, J.-F. (2017). Chapter 16—New Sources of Animal Proteins: Cultured Meat. In P. P. Purslow (Ed.), *New Aspects of Meat Quality* (pp. 425–441). Woodhead Publishing. https://doi.org/10.1016/B978-0-08-100593-4.00017-5

Schwarz, H., Zhang, Y., Zhan, C., Malm, M., Field, R., Turner, R., Sellick, C., Varley, P., Rockberg, J., & Chotteau, V. (2020). Small-scale bioreactor supports high density HEK293 cell perfusion culture for the production of recombinant Erythropoietin. *Journal of Biotechnology*, *309*, 44–52. https://doi.org/10.1016/j.jbiotec.2019.12.017

Simion, A. I., Grigoras, C. G., Bardaşu, L. E., & Dabija, A. (2017). Modelling of the thermophysical lactic acid aqueous solutions. Density and viscosity. *Food and Environment Safety Journal; Vol 11, No 4 (2012)*. http://fens.usv.ro/index.php/FENS/article/view/308/306

Sinke, P., & Odegard, I. (2021). *LCA of cultivated meat: Future projections for different scenarios* (p. 50). CE Delft. https://cedelft.eu/wp-content/uploads/sites/2/2021/04/CE_Delft_190107_LCA_of_cultivated_meat_Def.pdf

Stickel, J. J., & Powell, R. L. (2005). Fluid Mechanics and Rheology of Dense Suspensions. *Annual Review of Fluid Mechanics*, *37*(1), 129–149. https://doi.org/10.1146/annurev.fluid.36.050802.122132

Stout, A. J., Mirliani, A. B., Rittenberg, M. L., Shub, M., White, E. C., Yuen, J. S. K., & Kaplan, D. L. (2022). Simple and effective serum-free medium for sustained expansion of bovine satellite cells for cell cultured meat. *Communications Biology*, *5*(1), Article 1. https://doi.org/10.1038/s42003-022-03423-8

Svay, K., Urrea, C., Shamlou, P. A., & Zhang, H. (2020). Computational fluid dynamics analysis of mixing and gas–liquid mass transfer in wave bag bioreactor. *Biotechnology Progress*, *36*(6), e3049. https://doi.org/10.1002/btpr.3049

Telis, V. R. N., Telis-Romero, J., Mazzotti, H. B., & Gabas, A. L. (2007). Viscosity of Aqueous Carbohydrate Solutions at Different Temperatures and Concentrations. *International Journal of Food Properties*, *10*(1), 185–195. https://doi.org/10.1080/10942910600673636

Verbruggen, S., Luining, D., van Essen, A., & Post, M. J. (2018). Bovine myoblast cell production in a microcarriers-based system. *Cytotechnology*, *70*(2), 503–512. https://doi.org/10.1007/s10616-017-0101-8

Verma, R., Mehan, L., Kumar, R., Kumar, A., & Srivastava, A. (2019). Computational fluid dynamic analysis of hydrodynamic shear stress generated by different impeller combinations in stirred bioreactor. *Biochemical Engineering Journal*, *151*, 107312. https://doi.org/10.1016/j.bej.2019.107312

Wadaugsorn, K., Limtrakul, S., Vatanatham, T., & Ramachandran, P. A. (2016). Hydrodynamic behaviors and mixing characteristics in an internal loop airlift reactor based on CFD simulation. *Chemical Engineering Research and Design*, *113*, 125–139. https://doi.org/10.1016/j.cherd.2016.07.017

Wilcox, D. C. (2006). *Turbulence modeling for CFD* (3rd ed). DCW Industries.

Wyma, A., Martin-Alarcon, L., Walsh, T., Schmidt, T. A., Gates, I. D., & Kallos, M. S. (2018). Non-Newtonian rheology in suspension cell cultures significantly impacts bioreactor shear stress quantification. *Biotechnology and Bioengineering*, *115*(8), 2101–2113. https://doi.org/10.1002/bit.26723

Yamamoto, K., Sokabe, T., Watabe, T., Miyazono, K., Yamashita, J. K., Obi, S., Ohura, N., Matsushita, A., Kamiya, A., & Ando, J. (2005). Fluid shear stress induces differentiation of Flk-1-positive embryonic stem cells into vascular endothelial cells in vitro. *American Journal of Physiology-Heart and Circulatory Physiology*, *288*(4), H1915–H1924. https://doi.org/10.1152/ajpheart.00956.2004

Yang, J., Guertin, P., Jia, G., Lv, Z., Yang, H., & Ju, D. (2019). Large-scale microcarrier culture of HEK293T cells and Vero cells in single-use bioreactors. *AMB Express*, *9*(1), 70. https://doi.org/10.1186/s13568-019-0794-5

Zhan, C., Hagrot, E., Brandt, L., & Chotteau, V. (2019). Study of hydrodynamics in wave bioreactors by computational fluid dynamics reveals a resonance phenomenon. *Chemical Engineering Science*, *193*, 53–65. https://doi.org/10.1016/j.ces.2018.08.017

Zhang, G., Zhao, X., Li, X., Du, G., Zhou, J., & Chen, J. (2020). Challenges and possibilities for bio-manufacturing cultured meat. *Trends in Food Science & Technology*, *97*, 443–450. https://doi.org/10.1016/j.tifs.2020.01.026

Zhang, J., Li, X., Liu, H., Zhou, J., Chen, J., & Du, G. (2021). Hydrodynamics and mass transfer in spinner flasks: Implications for large scale cultured meat production. *Biochemical Engineering Journal*, *167*, 107864. https://doi.org/10.1016/j.bej.2020.107864

APPENDIX

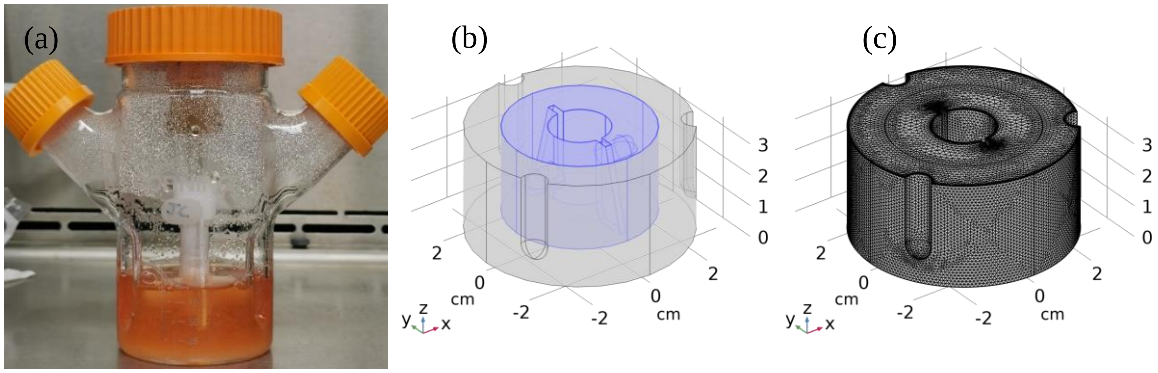

Figure 4.1. (a) Photo of Corning® 125 mL spinner flask, (b) corresponding geometry, and (c) mesh for CFD model.

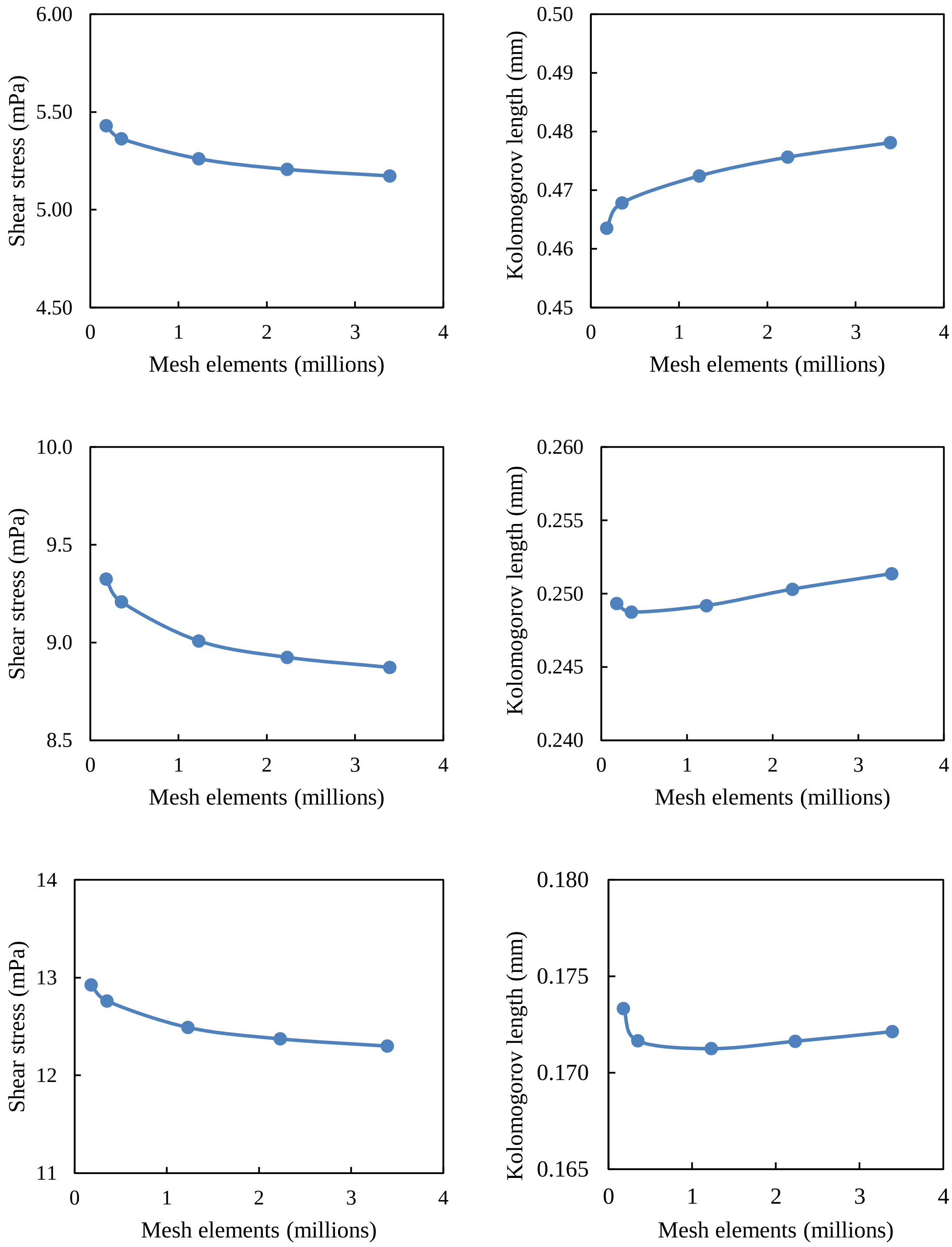

Figure 4.2. Average volumetric shear stress and Kolmogorov length mesh-independent study for spinner flask model using measured media viscosity values at (a) 30, (b) 60, and (c) 90 rpm.

Table 4.1. Cell growth characteristics for HEK cell culture in T-175 flasks

Total cells harvested	Growth rate (/day)	Doubling Time (days)	Fold Increase
$3.06 \pm 0.58 \times 10^7$	0.44 ± 0.05	1.59 ± 0.16	30.62 ± 5.78

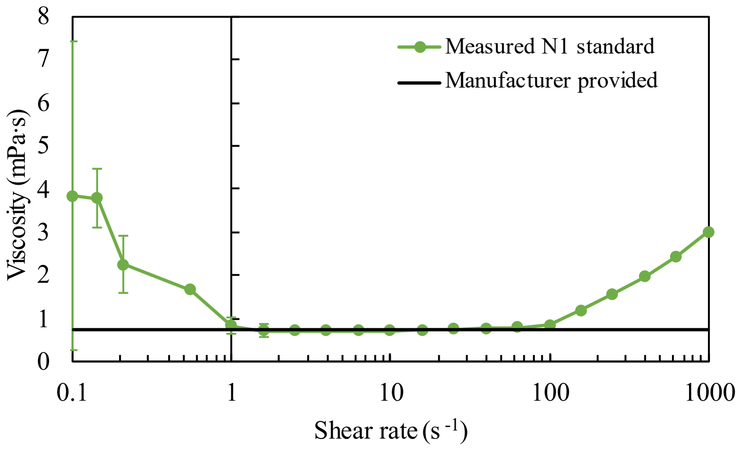

Figure 4.3. Viscosity measurements taken with DHR-2 at 37 °C for N1 standard compared against constant water values measured by Poon (2022).

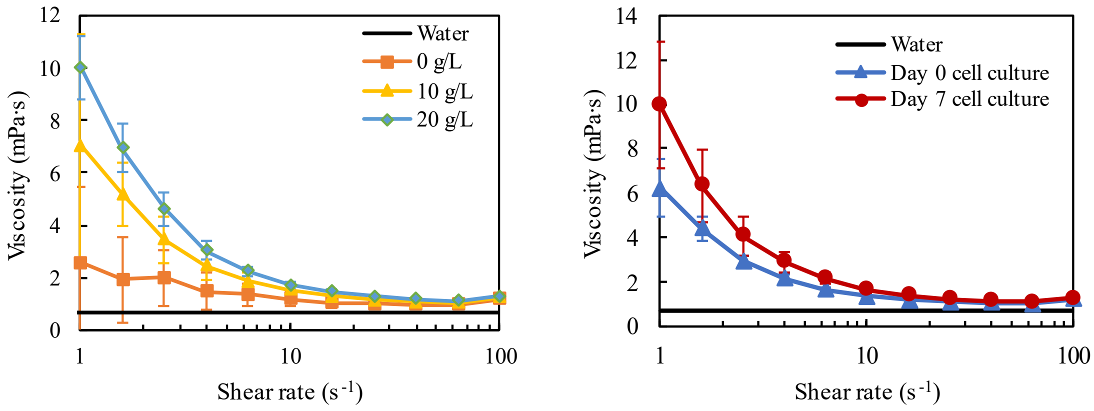

Figure 4.4. Viscosity measurements taken with DHR- 2 at 37 °C for (a) media with different concentrations of microcarriers and (b) spinner flask cell cultures with 13.89 g/L microcarriers compared against constant water values measured by Poon (2022).

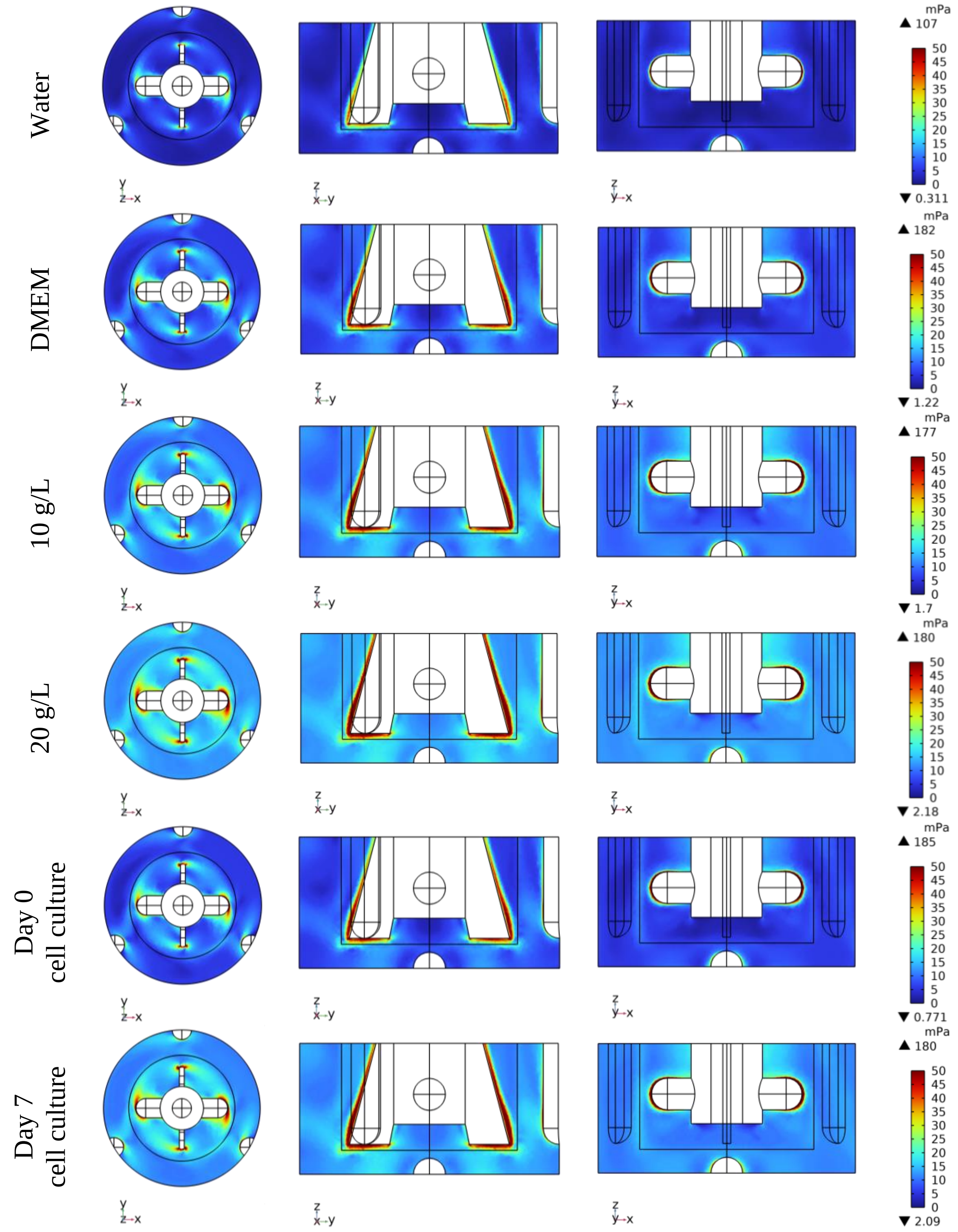

Figure 4.5. CFD-generated shear stress profiles inside spinner flask at 60 rpm.

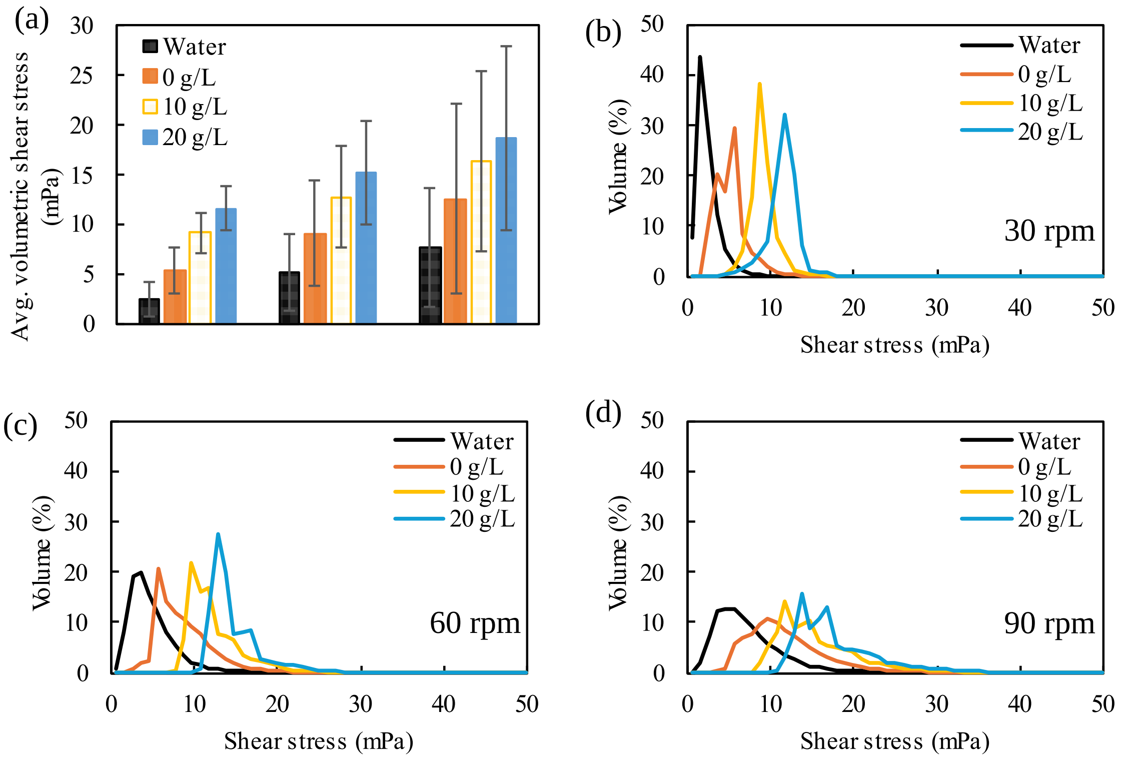

Figure 4.6. (a) Average volumetric shear stress and distribution histograms inside spinner flask at (b) 30, (c) 60, and (d) 90 rpm for DMEM with varying microcarrier concentrations.

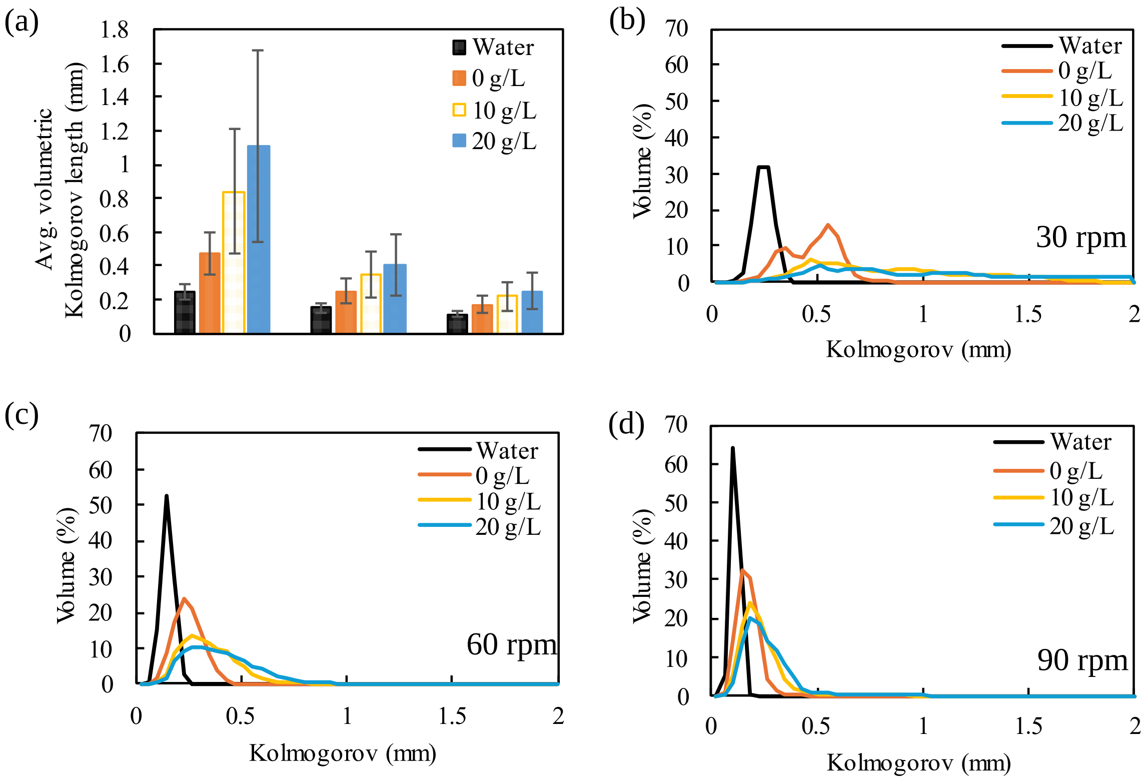

Figure 4.7. (a) Average volumetric Kolmogorov length and distribution histograms inside spinner flask at (b) 30 (c) 60, and (d) 90 rpm for DMEM with varying microcarrier concentrations.

Table 4.2. RMSE values as indicators of similarity of shear stress and Kolmogorov length profiles of constant and measured viscosities using constant water profiles as base for all mixing speeds.

RPM	Microcarrier concentration (g/L)	Shear stress RMSE (mPa)	Kolmogorov length RMSE (mm)
30	0	3.53	0.22
	10	7.27	0.64
	20	9.66	0.95
60	0	8.69	0.10
	10	10.75	0.23
	20	12.95	0.30
90	0	21.07	0.06
	10	18.56	0.13
	20	19.85	0.18

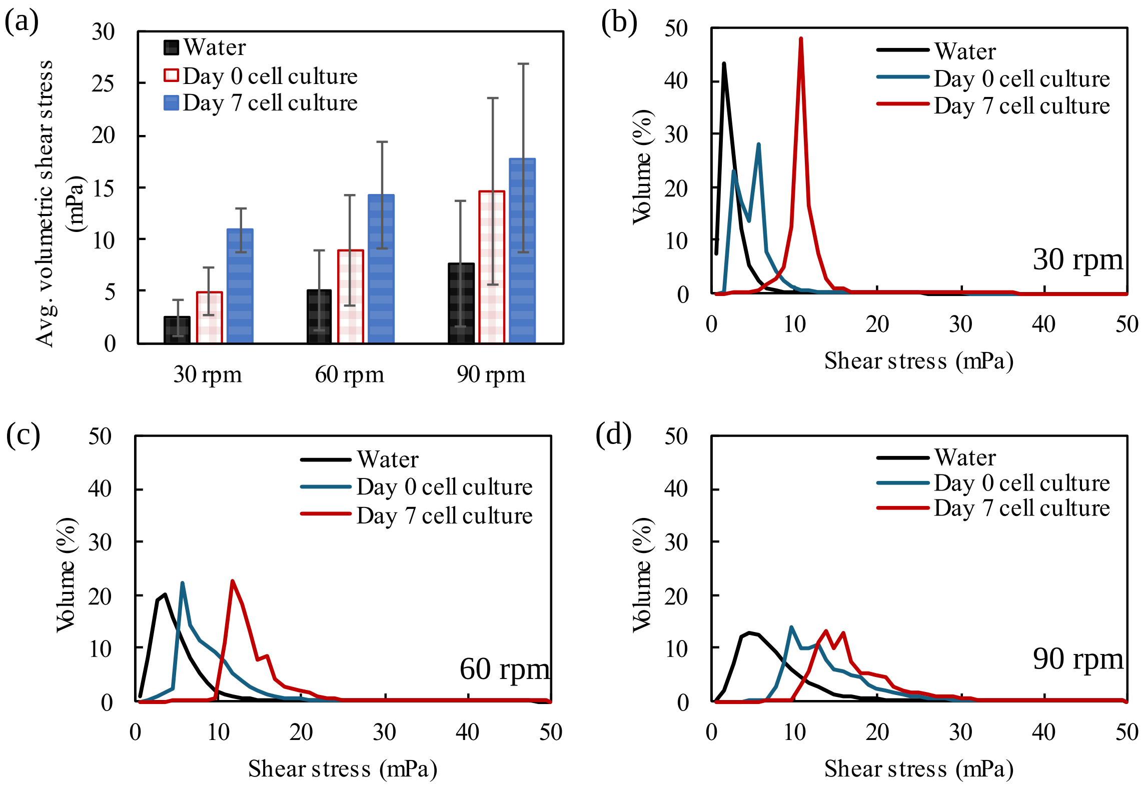

Figure 4.8. (a) Average volumetric shear stress and distribution histograms inside spinner flask at (b) 30, (c) 60, and (d) 90 rpm for constant water, and measured cell culture viscosity at day of seeding and after 7 days of culture.

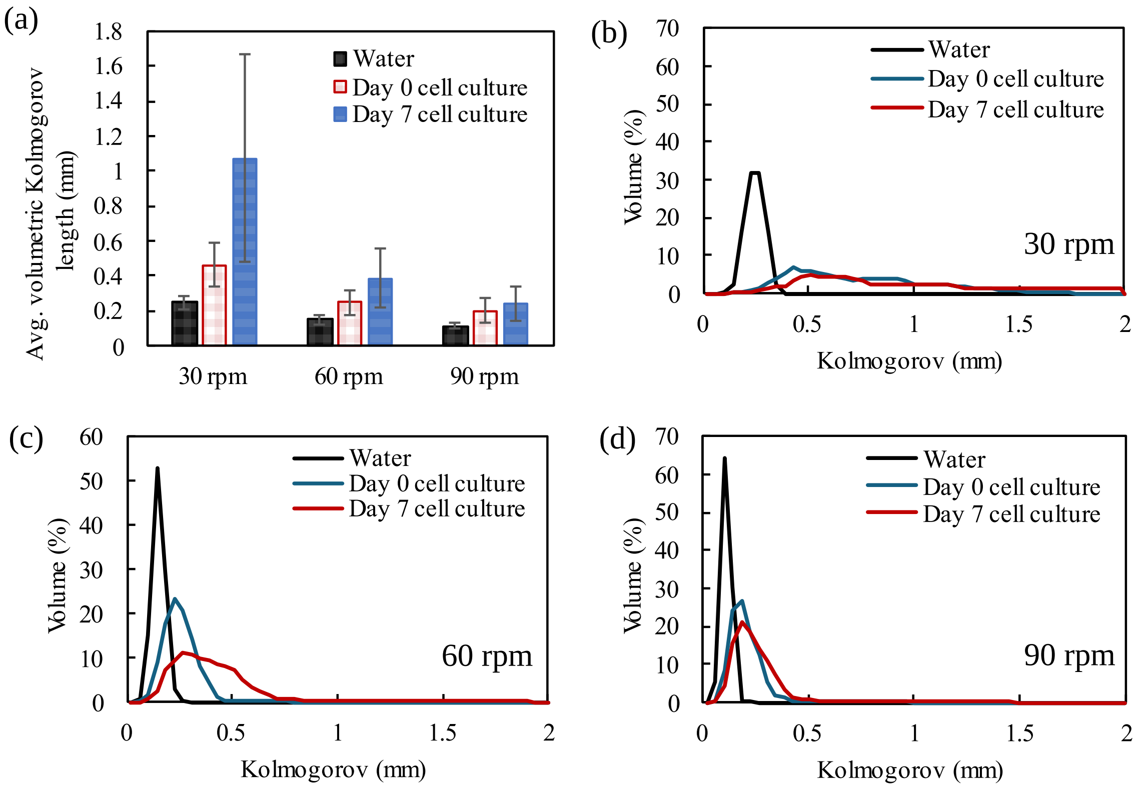

Figure 4.9. (a) Average volumetric Kolmogorov length and distribution histograms inside spinner flask at (b) 30, (c) 60, and (d) 90 rpm for constant water, and measured cell culture viscosity at day of seeding and after 7 days of culture.

Table 4.3. RMSE values as indicators of similarity of shear stress and Kolmogorov length profiles of constant and measured viscosities using constant water profiles as base for all mixing speeds.

RPM	Days of culture	Shear stress RMSE (mPa·s)	Kolmogorov length RMSE (mm)
30	0	6.02	0.53
	7	8.95	0.94
60	0	9.10	0.10
	7	12.18	0.29
90	0	17.46	0.11
	7	19.50	0.17

CONCLUSION AND FUTURE WORK

This dissertation addressed key limitations of CFD models for cell culture bioreactors such as high computational requirements and lack of accuracy due to oversimplification of material properties. The comprehensive review of CFD models for various bioreactors highlighted the need for faster and more accurate models for better process control of bioreactors. The development and application of Artificial Neural Network (ANN) and Convolutional Neural Network (CNN) models significantly enhanced the efficiency of CFD modeling using coarse mesh but with improved accuracy. These ML models corrected coarse-mesh-induced errors and predicted high-resolution fluid profiles from low-resolution counterparts with significantly lower computational time than typical CFD models. The study also emphasized the critical role of dynamic viscosity in CFD models. The characterization of dynamic viscosity of HEK 293T cell cultures revealed its significant impact on mixing performance in bioreactors. The results showed the need for careful monitoring of dynamic viscosity and proper control of mixing parameters for optimized cell growth, especially during scale-up production operations. This foundational work that integrates CFD modeling with ML approach could significantly contribute to the commercialization of cultivated meat and the broader field of tissue engineering.

Upon the foundational work, extensive research activities need to be performed in the following directions to support the long-term goal of developing a digital twin for broader applications in biomanufacturing. A digital twin, comprising both a physical and virtual counterpart of a process, allows for real-time simulation of the physical system's behavior, with information flowing bidirectionally between the two. The models used for the virtual part should be integrated multiscale models that represent the physical counterpart as closely as possible.

First, the CFD models developed in this study that use apparent viscosity of fluids without distinguishing the different phases (e.g., media, microcarrier, cells) can be further refined. For example, the models could be expanded to account for the multiple phases present in cell culture bioreactors, such as the media, cells, and sparged gases.

Additionally, these models should incorporate cell growth and death kinetics by integrating agent-based modeling (ABM), as discussed in Chapter 1, to be applicable to biomanufacturing processes.

Moreover, it is important to further evaluate the impact of cell lines on the rheological properties and bioreactor performance. For cell lines in different applications (e.g., myoblasts or adipocytes in cultivated meat production), the different cell growth kinetics and metabolism behavior will impact the dynamic rheological properties, and the shear stress profiles. Similar work on viscosity characterization and impact on mixing performance needs to be extensively conducted.

Furthermore, the ML models need to be significantly improved and expanded to support the development of digital twins. First, the generalization of the ML models still needs to be further improved to predict CFD results of bioreactors with different configurations. So far, the ML models in this study were mainly trained for bioreactors using radial impellers. Extensive CFD modeling results using various bioreactor designs could expand the database to train a more robust model with better generalization. Moreover, current CFD modeling only simulates stationary conditions without considering the time-dependent flow behavior. Other ML modeling strategies (such as introducing Long-Short Term Memory (LSTM) layers and/or using recurrent CNN approach) can be used in simulating real-time bioreactor performance. New ML models for the integrated multiscale model that couple CFD and ABM also needs to be developed to achieve the real-time flow and cell growth predictions. The ML supported digital twin models could be periodically re-trained by incorporating new data collected from experiments. All these alternatives and more work could be explored as future research based on the foundational work presented in this dissertation.

VITA

Fernando José Cantarero Rivera was born and raised in Tegucigalpa, Honduras. Inspired by his mother's work developing food safety plans for food companies around Honduras, Fernando quickly gained a great interest in Food Science and chose this as his major at Zamorano University. In 2017, an exchange program allowed him to work for a full semester in the Process Modeling and Validation laboratory at Purdue University where he later got accepted and pursued his Master's degree. His work there focused on aseptic process modeling and had the opportunity to be part of a team that validated a new aseptic filler for Heartland Foods Group in Indianapolis, IN. In August 2020, he finished his MS and was accepted to pursue his Ph.D. at the University of Tennessee, Knoxville under the guidance of Dr. Jiajia Chen. During his time at UTK he had the opportunity to work in a multidisciplinary research team called the Cultivated Meat Modeling Consortium (CMMC) to develop a model that could predict cell proliferation and yield based on CFD simulation data. Fernando's Ph.D. work focused on enhancing computational fluid dynamics models of cell culture bioreactors by developing machine learning algorithms to generate high-resolution data with minimal computational requirements.